Final work : Low speed dynamic stall modelling for 2D airfoils

Auteur : Sanchez Martinez, Mariano
Promoteur(s) : Dimitriadis, Grigorios; Terrapon, Vincent
Faculté : Faculté des Sciences appliquées
Diplôme : Master en ingénieur civil en aérospatiale, à finalité spécialisée en "turbomachinery aeromechanics (THRUST)"
Année académique : 2017-2018
URI/URL : http://hdl.handle.net/2268.2/5506

Low speed dynamic stall modelling for 2D airfoils

Université de Liège - Faculté des Sciences Appliquées

Supervisors:
Dimitriadis, Grigorios
Terrapon, Vincent

Travail de fin d'études réalisé en vue de l'obtention du grade de master "Ingénieur civil en aérospatiale, à finalité spécialisée en "turbomachinery aeromechanics (THRUST)"" par

Sánchez Martínez, Mariano
s174299

Année académique 2017-2018

Abstract

Research on low Reynolds unsteady aerodynamics is of great importance on the design of small unmanned aerial vehicles. Dynamic stall is the periodic separation and re-attachment of the boundary layer around oscillating wings. The physics of the phenomenon are very complex and have previously been described for different applications, such as helicopter rotor blades and horizontal axis wind turbines.

Dynamic stall can be modelled by using semi-empirical models. Two examples are the Leishman-Beddoes and ONERA models. An adaptation of the Leishman-Beddoes model was previously developed in the department, accounting for different behaviour in low Reynolds flow conditions.

In this thesis, CFD simulation results of the flow around a NACA0012 profile are compared to the corresponding experimental load coefficients in low Reynolds ($\sim 2 \times 10^4$), static conditions. There are some differences between both, especially for the chordwise force. Static stall onset is compared to the experimental results. It is shown that Kirchhoff's relation between the separation point and the normal force coefficient does not hold for the CFD results. It overestimates the attached portion of the airfoil. The CFD stall onset mechanism is also different from the one observed from the experiments, due to the lack of a laminar separation bubble.

Other important result is the exploration time evolution of dynamic stall in several different cases, using 2D Unsteady RANS simulations. In general, the load coefficients obtained compare well to the experimental results, though their agreement is not perfect. CFD predicts a large dip in the normal force and pitching moment not present in the experiments.

Vortex onset and evolution is described by using several pressure coefficient maps, overlaid by the instant velocity vectors. The simulated mechanism is explained in further detail. It is shown that several vortices form in each cycle, both over the suction surface and at the trailing edge.

From the time evolution of the flow field it is possible to obtain several parameters required for the semi-empirical model, which are then compared to the experimentally determined ones. While stall onset is delayed in the CFD simulations, the model parameters show good agreement with the experimentally determined ones.

Acknowledgements

I would like to thank my supervisors, Prof. Grigorios Dimitriadis and Prof. Vincent Terrapon for giving me the opportunity to work on this topic and their invaluable assistance. I would also like to thank Johan Boutet from the LTAS-AEA (Aeroelasticity and Experimental Aerodynamics Lab) for his interest and help with the interpretation of the data. I wish to also thank Hüseyin Güner and David Thomas from the MTFC (Multiphysics and Turbulent Flow Computation) for their help on setting up the simulations with SU2.

Many thanks also to Prof. Daniella Raveh and Dr. Wrik Mallik from the Faculty of Aerospace Engineering at the Technion for their comments on dynamic stall RANS simulations. I want to also thank the research and teaching teams with whom I have worked during these years.

I would also like to thank my parents and siblings for their support, especially during the course of this thesis. Finally, I would like to acknowledge my sister for her help with the proofreading.

Computational resources have been provided by the Consortium des Équipements de Calcul Intensif (CÉCI), funded by the Fonds de la Recherche Scientifique de Belgique (F.R.S.-FNRS) under Grant No. 2.5020.11.

Contents

List of Figures

List of Tables

Chapter 1

Project description

1.1 Introduction

The purpose of the present document is to study how Computational Fluid Dynamics (CFD) modelling of dynamic stall at a combination of low Reynolds and Mach numbers can be performed and which information, complementary to experimental investigations, can be obtained from such a simulation.

Dynamic stall is a phenomenon occurring in moving, streamlined bodies. It consists in the detachment and re-attachment of the flow around them, influenced by the movement of the body. It is related to static stall, though its mechanisms differ in some points.

Historically, this phenomenon has been studied by the helicopter rotor community, as well as by wind turbine research groups. Both of these applications exhibit moderate to high Reynolds numbers. Dynamic stall was studied in helicopter operation due to the need to assess the aerodynamic loads over the rotor in different conditions, such as forward flight.

Rotors in conventional, horizontal axis wind turbines (HAWT) are also subjected to periodic changes in the local flow conditions and obtaining the loading over the blades is a requirement to calculate the power output and accurately predicting those in various wind conditions is a key aspect of evaluating a HAWT design. Furthermore, the variations in loading over the blades can lead to mechanical failure because of fatigue.

The importance of dynamic stall in wind turbines led to the development of updated techniques for modelling dynamic stall at low Mach numbers. There were some adaptations of compressible, semi-empirical models, such as the Leishman-Beddoes approach, so that their behaviour more closely matched that of incompressible flow [1–3]. However, HAWTs still present high Reynolds number flow conditions.

In the last decade, further exploration of new wind turbine design paradigms, in-

cluding different topologies of vertical axis wind turbines (VAWT), as well as small unmanned aerial vehicles (UAV), have led to a renewed interest in the modelling of dynamic stall at relatively low Reynolds, $10^3 \lesssim Re_c \lesssim 10^5$ [4, 5]. This modelling is complicated by the increased importance of laminar-turbulent transition, which could affect significantly the unsteady flow behaviour.

1.2 Previous work

Before carrying out the present thesis, an experimental measurement campaign was performed. Its setup for measuring the aerodynamic loads was described in more detail by Boutet et al. The authors used a closed-loop wind tunnel, placed in the LadhyX laboratory [6].

They employed three 3D printed wings, representing three profiles: a flat plate with 4% thickness-to-chord ratio, a NACA0012 and a NACA0018. The NACA 4-series airfoils had a chord of $c = 0.04\,\text{m}$ and a span of $b = 0.13\,\text{m}$. All three wings are shown in Figure 1.1. Therefore, the aspect ratio was $AR = b/c = 3.25$. The loads over the wing were measured using a force/torque sensor.

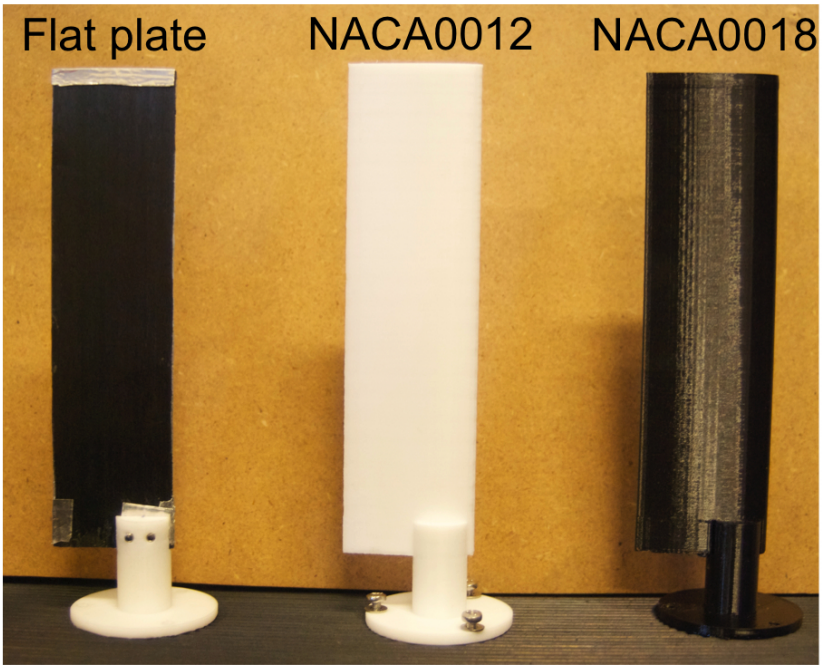

Figure 1.1: Wings used in the experimental setup [6]

In order to ensure that the flow was less affected by 3D features, the experimental setup included an end plate at the free end of the wing. At the other end, there was a small distance in order to prevent interaction between the wall boundary layer and the wing flow [6].

The results of these experiments were used in order to obtain several parameters for a modified Leishman-Beddoes model [7]. The parameters obtained from both methods can then be compared to each other.

1.3 Project objectives

The present project aims to establish a methodology for performing CFD analyses of low speed, low Reynolds dynamic stall simulations, using a free and open source software suite, Stanford University Unstructured (SU2). These simulations are intended to complement experimental research. For achieving this objective, the numerical results are compared to experimental data of the loads at different flow conditions.

The motivation behind the use of CFD is that it allows the study of the flow field characteristics as a function of time, providing further insight in the physics of the problem. The setup is considerably simpler than for experimental flow visualisation methods, such as Particle Image Velocimetry (PIV). However, there are several choices to be made that will impact the simulation accuracy. One of the objectives set for this work is to evaluate one such set.

An important innovation would be a description of the physics of the flow. It would be interesting to see which is their behaviour, to understand the physical mechanisms involved in dynamics stall and how they affect the overall results. One such mechanism is vortex generation and shedding.

Another objective is to estimate the parameters required for semi-empirical models. These can be obtained from numerical and experimental tests and both are to be compared. This comparison can help to validate the model, as well as to specify the correctness of the assumptions and of the phenomenological events on which it relies.

Finally, a validation of the methodologies used in experimental testing for estimating the parameters, as well as for predicting dynamic stall onset, is required. From experimental load measuring, one can obtain several stall onset criteria. The present work aims to compare them to others obtained from the CFD solution.

1.4 Thesis overview

The document is organised in several chapters and sections, each one devoted to a different topic. Chapter 2 details the theoretical framework, divided in several sections. First of all, there is a short introduction to static stall behaviour in low Mach, low Reynolds flow conditions. After this, dynamic stall is introduced, with special attention to flow physics and semi-empirical modelling. Then, the theory behind CFD and its modelling of turbulent flows is discussed, including its importance on the topic, its

main shortcomings and its advantages. Finally, some vortex detection algorithms used in the literature are detailed.

Chapter 3 describes the setup of the CFD simulations, which are carried out using the SU2 suite [8, 9]. It includes a description of the imposed movement of the airfoil, as well as of the geometry of the computational domain. The mesh employed is also described. It was created with GMSH [10]. The numerical parameters important for the problem are presented, as well as the boundary conditions set and the required mesh movement. Finally, the time and time-step convergence of the solution is evaluated.

Chapter 4 presents the main results obtained from the simulations of static cases. Static in the present document refers to test cases without pitching or plunging movements, while dynamic refers to the tests in which the airfoil is forced to undergo harmonic pitching oscillations.

First of all, the simulation results are compared to experimental data at the same flow conditions. Some of the model parameters are obtained, which would be calculated from the equivalent static experiments. Separation is discussed and compared to experimental estimations. The main shortcomings of the CFD setup are established.

Once the model is validated, the dynamic case results are presented, in Chapter 5, with a comparison between experimental and numerical data. Furthermore, a more detailed explanation of the flow physics is presented, based on the CFD flow field.

Simulation results for several test cases and various other parameters are estimated. There is a description of the vortex physics, especially taking into account its dynamics. A comparison of different stall onset criteria shows that there is little difference between them and provides some recommendations for experimental studies. At the end of the thesis, in Chapter 6, the main conclusions drawn from the project are detailed and suggestions for future work are outlined.

Chapter 2

Theoretical framework

The present chapter details the theoretical framework in which the project is set, describing the static and dynamic stall phenomena, as well as establishing the basis used in the semi-empirical models.

2.1 Static stall at the studied flow conditions

In a general way, at low Mach number, static stall can occur due to three main mechanisms, since transonic flow is not present. Each of these has different flow physics, which are detailed in the present section.

2.1.1 Trailing edge stall

This stall mechanism usually occurs in thicker airfoils. Flow separation starts at the trailing edge and the point at which it occurs moves upstream as the angle of attack increases. This behaviour leads to a relatively smooth decrease in the value of the lift curve slope. The maximum lift coefficient is considerably smaller in this kind of stall, compared to the other mechanisms [11, 12].

2.1.2 Leading edge stall

Leading edge stall usually occurs in airfoils of moderate thickness. The laminar boundary layer separates near the leading edge. The separated shear layer undergoes turbulent transition, is stabilised and therefore reattaches to the surface, forming a laminar separation bubble. At some angle of attack, this bubble bursts, leading to abrupt flow separation [11].

This kind of stall leads to a sharp decrease in the lift coefficient of the airfoil when flow detaches, since stall is pretty abrupt. Flow over the surface transitions from mostly attached to mostly detached very quickly [12].

2.1.3 Thin airfoil stall

Thinner airfoils show a different, though related, mechanism. The flow is unable to turn round the very sharp leading edge. This leads to a separation bubble over the leading edge, even at very low angles of attack, which grows in sizewith increasing angle of attack. The reattachment point moves downstream until the bubble engulfs the whole airfoil, thus leading to stall [11, 12].

2.2 Dynamic stall

Dynamic stall is a phenomenon in which the flow around an oscillating, or otherwise moving, airfoil detaches and re-attaches. While it shows similarities to static stall, there are some key differences. The present section first introduces the phenomenon, as well as the coordinate systems used. Then, it includes a small classification of dynamic stall, taking into account both the airfoil kinematics and the flow features. After that, there is a description of the main flow features, followed by several semi-empirical models. Finally, it presents the stall criteria employed in the study, as reported in the literature.

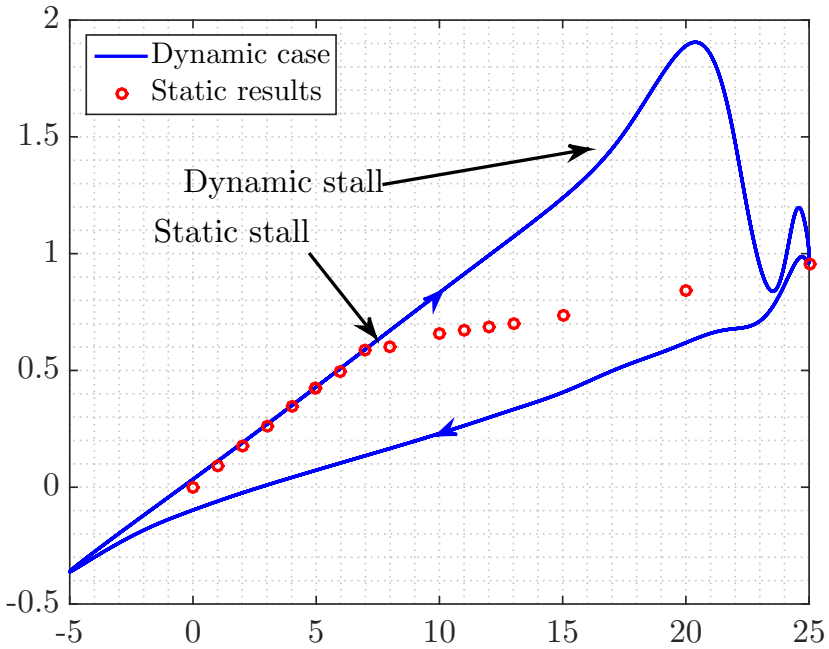

Figure 2.1: Normal force coefficient as a function of the α, static and dynamic CFD ($f = 5\,\mathrm{Hz}$)

One of the main differences with static stall is the presence, in the case of oscillating airfoils, of a hysteresis loop in the plots of aerodynamic load against instantaneous angle of attack. At the same angle of attack, the flow conditions will be considerably different depending on whether the airfoil is moving nose up or down. The loops can be clearly seen in the aerodynamic force and moment coefficients, as shown by McAlister et al. [13]. A comparison between the normal force coefficient values calculated during static CFD cases and a dynamic CFD case is shown in Figure 2.1.

Another important difference is that the flow can stay attached for far longer than in the static case. This can be deduced from Figure 2.1. It can be seen that the relation between angle of attack and c_n is approximately linear for far longer than in the static case. This indicates that flow separation occurs later than in static conditions, a phenomenon known as stall delay.

2.2.1 Coordinate systems

There are two main coordinate systems in use in the literature: the chordwise/normal forces and the drag/lift ones. The former is a moving frame of reference that moves with the airfoil while the latter is inertial, always aligned in directions parallel and perpendicular to the free stream. Each one is employed for different kinds of applications. The present work uses the first one, since it is the one usually evaluated in the study of helicopter rotors and therefore the one obtained in the semi-empirical models designed for that use.

It is easy to transform the loads from one set of coordinates to the other, by means of trigonometric relations. So, if α is the instantaneous angle of attack, then $c_n = c_l \cdot \cos\alpha + c_d \cdot \sin\alpha$ and $c_c = c_d \cdot \cos\alpha - c_l \cdot \sin\alpha$, where c_n, c_c, c_l and c_d are the normal, chordwise, lift and drag coefficients respectively. The pitching moment coefficient, c_m, is unchanged, only dependent on the point around which it is considered. It is usually measured at the quarter chord.

Furthermore, the CFD code provides a third, inertial reference system. For the dynamic cases, the chordwise/normal axes move with the airfoil. This is not the case on the x and y axes, as defined in the code. An overview of the three systems is shown on Figure 2.2. There, the differences between the systems are marked, where the two inertial coordinate systems are drawn in black and the moving frame of reference is drawn in gray.

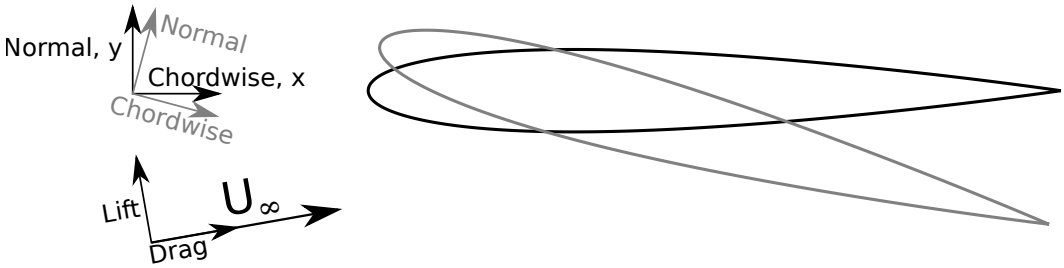

Figure 2.2: Coordinate systems

2.2.2 Classification of dynamic stall

The present section describes two ways of classifying this phenomenon. The first one refers to the intensity of the dynamic stall phenomena, separating it in deep and light stall. The second one includes a description of the movement of the airfoil.

2.2.2.1 Deep and light stall

McCroskey described a difference in behaviour between these two phenomena, relating to various flow features, which can then be used to classify a certain flow behaviour [14].

One of the differences on the flow field is related to the extent of the viscous region. Light stall shows a thin separated area, usually with a thickness similar in magnitude to the one of the airfoil. Deep stall cases show a much larger viscous layer, with a thickness of the order of the airfoil chord. A large vortex appears from the detached flow. This leads to a more important hysteresis loop, even if there is a small difference in the amplitude of the pitching motion [14].

Most of the cases studied in the present report showed a behaviour corresponding to deep stall. Only the simulation at both the lowest frequency and amplitude could be considered light stall.

2.2.2.2 Airfoil movement

Another classification is due to the movement of the airfoil, which can be any combination of pitch and plunge. Pitch refers to an oscillation around a point within the airfoil, perpendicular to the plane in which the airfoil is contained. Plunge, on the other hand, refers to a movement perpendicular to the flight path. The present work deals only with pitch oscillations. There have also been studies about other changes in the flow conditions, such as a modification in the value of the free-stream velocity [15].

2.2.3 Flow description

The flow around an oscillating airfoil is characterised by a departure from the corresponding steady flow, due to the effect of the rotational speed on the flow. This movement, assuming a thin, lightly cambered airfoil, could theoretically be modelled as a linear function of the chordwise coordinate, such that

$$[U, V] = [0, \dot{\alpha} \cdot (x - x_0)] \tag{2.1}$$

where x is the chordwise coordinate of the point, x_0 is the chordwise coordinate of the rotation axis, U and V the chordwise and normal airfoil velocities.

The velocity distribution over the airfoil is therefore equivalent to an effective camber. This effective camber is positive in the upstroke movement and it helps to delay separation. However, it is not the only phenomenon that increases the maximum normal force achievable, though it is probably the simplest one to model.

Two other important phenomena affecting the load over an airfoil are the leading edge jet and vortex. The leading edge jet appears as a consequence of the upwards movement of the leading edge, which increases the energy of the boundary layer. This helps to avoid flow reversal and the consequent detachment of the boundary layer.

The leading edge vortex can appear through several mechanisms; at some point it detaches and moves as a low pressure bubble downstream. This vortex counteracts the negative effect on the normal force of detached flow and is usually accompanied by a sharp decrease in the moment, as well as by a curvature change in the normal force.

This behaviour can be seen in Figure 2.1. In that case, the pre-stall normal force coefficient in the oscillating case is around twice the one in the static case.

2.2.3.1 Mechanisms of dynamic stall

Chandrasekhara et al. showed that in moderate and low Reynolds numbers there were three main mechanisms leading to the onset of dynamic stall, depending on the Mach number [16]. Since the present work deals with low Mach number flows, only the first one will be presented.

Their first finding was that the bursting of a laminar separation bubble (LSB) led to dynamic stall. The LSB appears close to the leading edge. Due to the high adverse pressure gradient the laminar boundary layer detaches. After the BL transitions to a turbulent one, it is able to reattach further downstream.

The bursting leads to a behaviour similar to that of leading edge stall. However, this bubble only appears if the boundary layer is laminar. Therefore, the authors decided to trip the airfoil, so that it presented a fully turbulent one. This tripping delayed stall, but did not avoid it completely. They also found that at higher Mach numbers, there was interaction between supersonic flow and the LSB [16].

2.2.4 Flow modelling

The flow around oscillating airfoils cannot be accurately approximated by only considering the instantaneous angle of attack. The current state of the flow depends on the entire history of the motion. This is true both for potential and viscous flows. As explained in Section 2.2.3, some of the flow structures are intrinsically viscous and others also appear in fully attached flow.

The intrinsic difficulties in modelling turbulent flow led to the creation of semi-empirical tools, such as the Leishman-Beddoes or the ONERA models. These are based on a set of parameters obtained by means of dynamic and static experiments, which represent the behaviour of different flow features.

2.2.4.1 Leishman-Beddoes model

The Leishman-Beddoes model is a semi-empirical description of the flow surrounding a moving airfoil. This model consists of two main blocks, each describing different features of the flow. Both are available in indicial [17] and state-space formulations [18,

19]. The first block is a potential flow model, which does not take into account detached flow effects. The Leishman-Beddoes model predicts the value of the normal and chordwise flow coefficients, as well as the pitching moment around the quarter chord.

The authors described a compressible flow model, inspired by the Wagner function and adapted for these kinds of flows. Their attached, compressible model is shown here, compared to the Wagner function. These functions represent the response to a step change in the flow conditions, which can be used to compute the value of lift, for example, at a specific time instance [19, 20]

$$\Phi^C_{LB}(t) = 1 - A_1 \cdot e^{-b_1\beta^2\frac{Ut}{b}} - A_2 \cdot e^{-b_2\beta^2\frac{Ut}{b}} \tag{2.2}$$

$$\Phi_W(t) = 1 - \Psi_1 \cdot e^{-\varepsilon_1\frac{Ut}{b}} - \Psi_2 \cdot e^{-\varepsilon_2\frac{Ut}{b}} \tag{2.3}$$

where $\Phi^C_{LB}(t)$ is the value of the time step-response function defined by Leishman and Beddoes; $\Phi_W(t)$ is the corresponding Wagner function; A_n, b_n, Ψ_n, ε_n are various flow coefficients; $\beta = \sqrt{1 - Ma^2_\infty}$ is the compressibility factor and b is the half-chord.

While these two models use different names for the parameters, their function is equivalent, except for β. The values of the other coefficients are shown in Table 2.1. The time characteristics are otherwise similar, with the coefficient of time multiplied by flow velocity divided by the half-chord, $\frac{Ut}{b}$.

Leishman-Beddoes		Wagner	
A_1	0.3	Ψ_1	0.165
b_1	0.14	ε_1	0.0455
A_2	0.7	Ψ_2	0.335
b_2	0.53	ε_2	0.3

Table 2.1: Potential flow coefficients

The Leishman-Beddoes potential flow model is only accurate for Mach numbers higher than 0.3. At lower Mach numbers, the Wagner model should be used.

Viscous effects are added to the potential flow model. One such effect concerns separation at the trailing edge, which is included based on Kirchhoff theory. This theory allows to estimate the value of the normal force coefficient, c_n, as a function of the non-dimensional separation point, $f = x_{sep}/c$, where c is the airfoil chord:

$$c_n(f) = c^P_n \cdot \left(\frac{1 + \sqrt{f}}{2}\right)^2 \tag{2.4}$$

where c^P_n refers to the inviscid component of the normal force coefficient [18].

It is possible to derive the value of $f(\alpha)$ from this load coefficient, therefore estimating its value from experimental results:

$$f(\alpha) = \left(2\sqrt{\frac{c_n(\alpha)}{\alpha \cdot \frac{\partial}{\partial\alpha}c_n\big|_{\alpha=0}}} - 1\right)^2 \tag{2.5}$$

where α is the corresponding angle of attack and assuming that $c_n(0°) = 0$, true for a symmetric airfoil.

The Leishman-Beddoes model includes an empirical, piecewise description of the separation point location as a function of the angle of attack [17, 18]:

$$f(\alpha) = \begin{cases} 1 - 0.3 \cdot e^{\frac{\alpha - \alpha_1}{S_1}} & \alpha \leq \alpha_1 \\ 0.04 + .66 \cdot e^{\frac{\alpha_1 - \alpha}{S_2}} & \alpha > \alpha_1 \end{cases} \tag{2.6}$$

where α_1, S_1 and S_2 are parameters to be determined from experimental testing.

The moment coefficient can be calculated from the normal force coefficient and a model of the centre of pressure. This point is the one in which the aerodynamic forces over an airfoil are considered to be applied. Since the force in the chordwise direction is small, CP is a non-dimensional chordwise factor,

$$CP = \frac{c_m}{c_n} \tag{2.7}$$

$$CP \cdot c = \frac{M}{N} \tag{2.8}$$

where c_m is the moment coefficient around the quarter chord, c_n the normal force coefficient, M the magnitude of the moment around the quarter chord and N the normal force.

Leishman and Beddoes devised a fit for this location and $CP \cdot c_n$ would give the corresponding moment coefficient

$$c_m(f) = [K_0 + K_1 \cdot (1 - f) + K_2 \cdot \sin(\pi \cdot f^m)] \cdot c_n(f) \tag{2.9}$$

where K_0, K_1, K_2 and m are parameters to be obtained from experimental testing.

The parameters can be obtained from static tests. It should be noted, however, that Equations (2.9) and (2.4) are only valid for static cases. The authors then applied a delay to both the separation and centre of pressure, in order to reflect the dynamic behaviour. This delay is included as a non-dimensional time, to be determined from experimental testing [20].

Non-dimensional times are meant to be constant for moderately different flow conditions. The usual procedure is

$$T_* = t_* \cdot \frac{U_\infty}{b} \tag{2.10}$$

where t_* is the dimensional time, T_* the corresponding non-dimensional time, U_∞ the free-stream velocity and b the airfoil half-chord.

Another important feature of the model is vortex generation and propagation, which modify the aerodynamic loads by increasing the normal force and applying a downstroke moment. This vortex is characterised by two factors: the location of its centre

of pressure and its strength. The non-dimensional chordwise location of the centre of pressure is modelled, generally, by using a sinusoidal pattern [17, 19]

$$CP_v = \frac{1}{4}\left[1 - \cos\left(\frac{\pi \cdot t_v}{t_{vl}}\right)\right] \tag{2.11}$$

where CP_v is this non-dimensional location, t_v is the time since vortex onset and t_{vl} is a characteristic time of the vortex, the time it takes for the structure to shed since its onset.

Vortex strength is modelled by a parameter C_v and the vortex normal force coefficient is proportional to its rate of change. It is obtained from previously obtained values,

$$C_v(t) = \begin{cases} c_n^C \left[1 - \left(\frac{1+\sqrt{f}}{2}\right)^2\right] & 0 \leq t_v \leq 2 \cdot t_{vl} \\ 0 & t_v > 2 \cdot t_{vl} \end{cases} \tag{2.12}$$

where c_n^C is the normal force coefficient due to circulatory forces and f is a delayed separation point [19].

2.2.4.2 Variations on Leishman-Beddoes

The Leishman-Beddoes model was designed and tuned, for moderate to high Mach number operation, since that was its intended use. It was developed for evaluating the behaviour of helicopter rotors. The increase in research on HAWTs, which work at low Mach numbers, led to the formulation of low-speed variations of the model.

One such development was presented by Sheng et al., for a set of airfoils for which experimental data was available. The main differences included switching from a critical normal force coefficient to a critical angle of attack in order to define dynamic stall onset, as well as adding a non-dimensional time constant, which they defined from the slope of α_{DS} versus $r = \dot{\alpha} \cdot b/U_\infty$, the reduced pitch rate [1, 2].

Sheng et al. added a second parameter for flow reattachment, following approximately the same behaviour as the one presented for the flow separation phase, depending on a normal force coefficient minimum [2, 21].

In the present work, the minima were observed to always occur at the minimum angle of attack, independently of the reduced pitch rate. This occurred for both the experimental and numerical results. Therefore, this reattachment parameter could not be evaluated in the same way.

Sheng et al. also modified the treatment of the vortex, applying another delay to the location of separation and modifying the shape of the centre of pressure of the vortex. They defined a piecewise function

$$CP_v(t_v) = \begin{cases} \sin^{3/2}\left(\frac{\pi t_v}{2t_V}\right) & 0 \leq t_v \leq t_V \\ \cos^2\left(\frac{\pi(t_v - t_V)}{t_{vl}}\right) & t_v > t_V \end{cases} \tag{2.13}$$

where t_V is another vortex characteristic time [2].

2.2.4.3 Non-dimensional parameters

From experimental data, it is possible to obtain several parameters, which are used by Leishman-Beddoes and similar models to simulate the behaviour of a pitching airfoil. The two main parameters obtained from the simulation were the separation delay time (T_a) and the vortex shedding time (T_{vl}).

Separation delay time This parameter represents a delay in the point of separation. It can be measured as the difference in time between the static and dynamic separation curves and then turned non-dimensional as per Equation (2.10), from t_a to $T_a = t_a \cdot \frac{U_\infty}{b}$.

Vortex shedding time This parameter represents the time it would take for the vortex to travel from the leading edge to the trailing edge. It can be calculated as $t_{vl} = \frac{c}{U_{vortex}}$, where U_{vortex} is the vortex propagation velocity. It can also be turned non-dimensional, in which case it becomes $T_{vl} = t_{vl} \cdot \frac{U_\infty}{b} = 2\frac{U_\infty}{U_{vortex}}$.

2.2.4.4 ONERA model

Another dynamic stall model is the one developed by ONERA. It consists of two differential equations, one related to attached flow effects while the other describes separated flow behaviour. These equations behave in a similar manner for the three main load coefficients: normal and chordwise forces and pitching moment [15].

For example, the normal force coefficient can be divided in two separate coefficients, as shown in Equation (2.14). The first one, C_{N_1}, is the attached flow value, taking into account the movement of the airfoil. The differential equation it fulfils is shown in Equation (2.15) The second one, C_{N_2}, includes the detached flow effects over the airfoil. Its constituent, second order differential equation is given in Equation (2.16). It is simple to adapt it to a first order ODE, by adding an extra parameter, in order to apply a Runge-Kutta, or other ODE numerical solution method.

$$C_N = C_{N_1} + C_{N_2} \tag{2.14}$$

$$\dot{C}_{N_1} = \lambda \cdot (C_{N_L} - C_{N_1}) + (\lambda \cdot s + \sigma) \cdot \dot{\alpha} + s \cdot \ddot{\alpha} \tag{2.15}$$

$$\ddot{C}_{N_2} = -a \cdot \dot{C}_{N_2} - r \cdot C_{N_2} - (r \cdot \Delta C_N + E \cdot \dot{\alpha}) \tag{2.16}$$

Some important values in these equations are the set of parameters, λ, s, σ, a, r and E, the values of which can be obtained from experiments. They can vary with the angle of attack, α. Two other, related, values also appear, they are C_{N_L}, which represents the linear, attached flow behaviour (i.e. $\alpha \cdot \frac{\partial}{\partial \alpha} C_N\big|_{\alpha=0}$) and $\Delta C_N = C_{N_L} - C_N$, the difference between attached and separated lift values [15].

While the presented equations only take into account the pitch motion, this model has been extended for other variations in the flow, including plunge and changes in the flow velocity, which are important for helicopter aerodynamics [15, 22, 23].

2.2.5 Dynamic stall onset criteria

In order to appropriately model dynamic stall, a dynamic stall onset criterion must be defined. Some such criteria were summarised by Sheng et al. These are obtained by studying the angular variation of the aerodynamic load coefficients, as well as the pressure coefficient in selected points. A selection of these is shown in Figure 2.3 [1].

2.2.5.1 Δc_m criterion

This criterion is shown in Figure 2.3a. Once the moment coefficient decreases under a certain amount, which is usually arbitrarily taken to be $\Delta c_m = -0.05$, dynamic stall is considered to have occurred. However, this value can induce some problems, especially in low amplitude simulations. In some of those, the moment may jump only slightly below that value.

In general, one should consider which value to use as a threshold for this criterion and it should be compared to other criteria. It is a simple one, though the drop used has to take into account previous experiences and the minimum c_m obtained.

2.2.5.2 $\frac{\partial}{\partial \alpha} c_c$ criterion

This criterion detects the local minima or maxima in the chordwise force coefficient. While in other studies the maxima were obtained, for the present one the minima are studied, as that was the experimental result [1, 6]. These are directly related to the flow phenomena and there are usually several such minima, providing further insight into different flow phenomena. One such example is shown in Figure 2.3b. Its main disadvantage is that, since it requires a derivative, it could lead to spurious detections, or it could be masked by noise. This is specially true when analysing experimental data.

2.2.5.3 $\frac{\partial^2}{\partial \alpha^2} c_n$ criterion

This method finds a point in which the curvature of the normal force coefficient as a function of the angle of attack starts to turn positive, as shown in Figure 2.3c. Usually, due to inviscid phenomena, the attached flow phase shows a slightly negative curvature. Once the vortex is formed, the resulting low pressure bubble increases substantially the c_n. Therefore, detecting the change in curvature can lead to a stall onset criterion.

The main drawback of this criterion is the confusion occurring between dynamic stall onset and vortex shedding. This second phenomenon is not required for dynamic

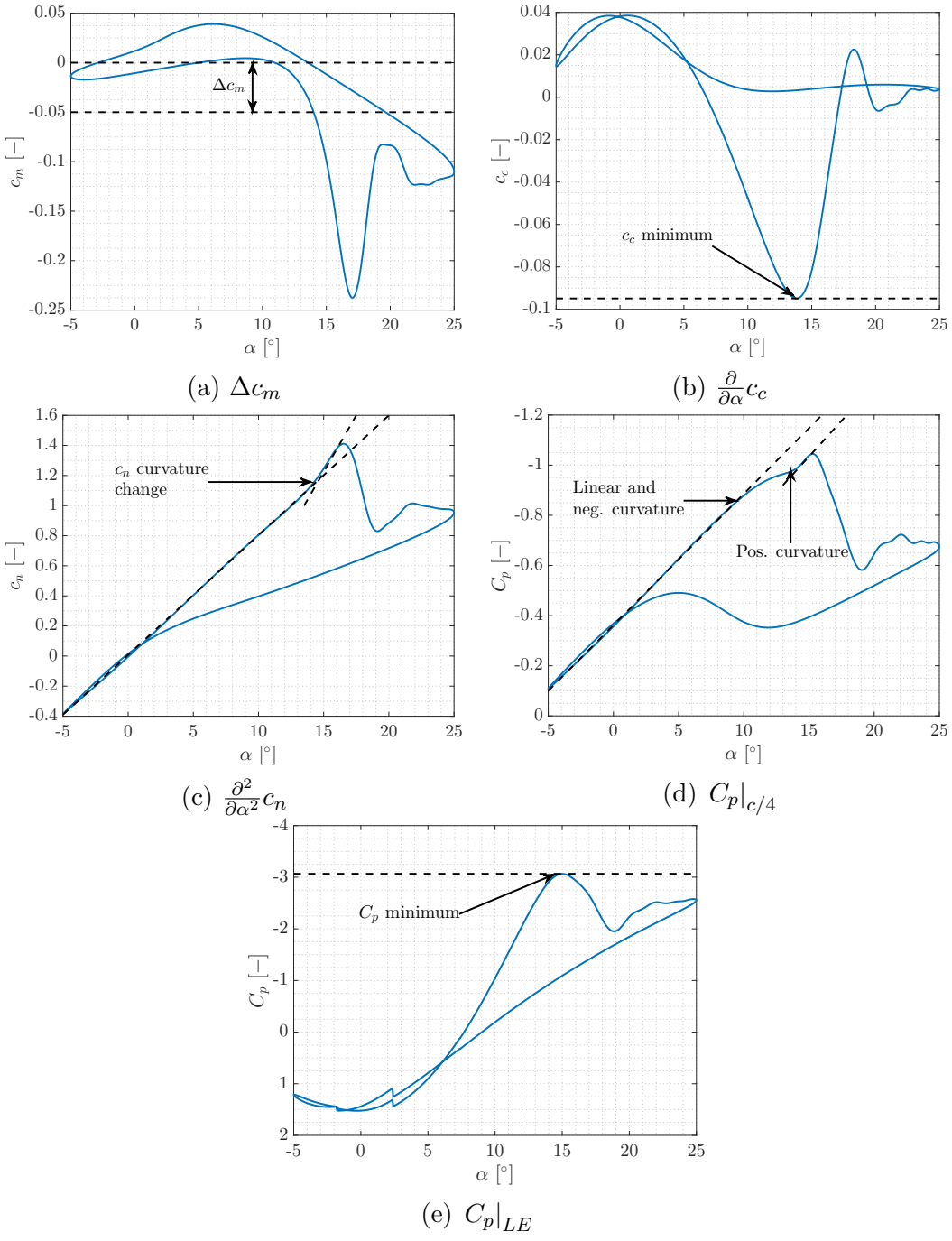

Figure 2.3: Graphical representation of different criteria for one set of results, based on Sheng et al. [1]

stall. In those cases, the c_n versus α plot does not show a positive curvature, it does not curve upwards.

Another drawback is related to the experimental data analysis. The second derivative amplifies even more high frequency components of the signal, especially affecting noise. Therefore, this function is not smooth, leading to possible errors identifying the onset.

2.2.5.4 $C_p|_{LE}$ and $C_p|_{c/4}$ criteria

Sheng et al. describe two criteria using the pressure coefficient distribution: one relating to the vortex downstream movement and a second one with the pressure coefficient at the leading edge. The first one relies on a change in curvature. It is shown in Figure 2.3d, with a sudden increase in the pressure coefficient before it starts to decrease, related to the passage of the vortex [1].

The leading edge peak, per Sheng et al., shows a collapse in the pressure coefficient, though such a sudden event was not observed in the present study. One of the cases is plotted in Figure 2.3e [1].

Again, the change in curvature is difficult to measure in experimental data. Furthermore, the present experimental setup did not have measurement taps at either of the two mentioned points.

2.3 Computational Fluid Dynamics frameworks

The present section details the main assumptions made during the setup of the CFD simulation, explaining the choices taken and which consequences they may have. The Finite Volume Method used is the standard way to perform aerodynamic calculations.

2.3.1 Turbulence modelling

Previously, dynamic stall had been investigated using a variety of turbulence models. The most important consideration considers the scale of turbulent structures to be modelled. At this point, there are differences between the simplest, Unsteady Reynolds-Averaged Navier-Stokes (URANS) models, to the most complex Direct Numerical Simulation (DNS), in which all the scales available are calculated. This last one is still only used for research, not for engineering or hybrid applications, due to its high computational cost.

Between those two models, one can find Large Eddy Simulation (LES), as well as hybrid URANS-LES schemes. In these cases, the smallest turbulence length scales are modelled, while the largest and more energetic ones are calculated explicitly.

Pure LES is currently unfeasible for most cases, so hybrid URANS-LES approaches are usually employed. There are different ways of achieving these, such as Detached Eddy Simulation (DES) [24] or Delayed DES (DDES) [25]. This last approach has been employed by several authors in order to model dynamic stall, such as Martinat et al., Wang et al. or Zanotti et al. [26–28].

The specific turbulence model used in these hybrid and pure URANS cases has also been a point of study in the community, with the general agreement that Shear Stress Transport (SST) models provide a more trustworthy representation of the physics [26–29].

The problem was solved first using a URANS solver, including Menter's k–ω SST turbulence model [30, 31], as well as the Spalart-Allmaras (S-A) one-equation model [32]. Since the SST model provided superior agreement in the present static cases, it was used in the dynamic simulations performed.

An inconvenience of using such a model consists in the difficulty of modelling laminar flow behaviour, as should be the case for part of the boundary layer. A transition model would be needed in order to ensure that the flow is appropriately represented in that area. SU2 implements two such models: the Baş-Çakmakçıoğlu transition model [33] and the Langtry-Menter model [34, 35]. The first one works with the S-A model, while the second uses Menter's SST turbulence model, adding extra equations. Unfortunately, it was not possible to use this last model in the present work, the simulations failed.

2.3.2 Physical dimensions

One of the assumptions to be made when examining a problem is the number of dimensions that are required in order to accurately model the flow behaviour. Dynamic stall has a strongly three dimensional behaviour and several authors have compared the results from 2D and 3D models. Their work has shown that in several different flow conditions, upstroke behaviour is dominated by two-dimensional effects, while downstroke behaviour is more accurately modelled considering the 3D geometry [26–28].

In the present work it was decided to start with a two dimensional setup and to check if the results matched closely the experimental behaviour, or if there was any room for improvement with a 3D model.

2.3.3 Compressibility of the flow

Due to the low value of the freestream Mach number ($Ma_\infty < 0.03$), it could be assumed that the flow is incompressible. However, at usually incompressible conditions ($Ma_\infty = 0.09$), extremely low pressure coefficient values have been reported [13, 36].

Furthermore, the incompressible formulation employed by SU2 does not allow for the simulation of unsteady cases [37]. Therefore, it was decided to use the compressible flow solver. For the examined cases, the maximum local Mach number in the field was in the vicinity of 0.04.

2.4 Vortex detection algorithms

As has been explained in Section 2.2, vortices are a key component of the flow behaviour in dynamic stall. Therefore, semi-empirical models such as the Leishman-Beddoes method require the determination of some of their characteristics.

However, the detection of these phenomena is problematic. This is exacerbated by the characteristics of the simulation setup. Usually, vortex detection algorithms rely on performing tensor operations on a 3D field. However, the calculations were performed using 2D URANS. Therefore, an adaptation of these procedures was required. One such way could be found in the literature on Particle Image Velocimetry (PIV). As for the present simulations, PIV is usually obtained in a plane field. Even though more complex setups allow the capturing of small out-of-plane motion, it is most suited to calculate in-plane velocities. Therefore, it is a comparable field for 2D methods. A review of the literature revealed several vortex detection methods, a selection of which is shown in the present section [38–41].

2.4.1 Q–criterion

This criterion, developed based on work by Hunt, is based on the decomposition of the velocity gradient tensor in two other tensors: a symmetric one ($\mathbf{S}$) and an anti-symmetric one ($\mathbf{\Omega}$). The calculation of the criterion is shown in Equation (2.17). In those regions with a positive Q–criterion, vorticity dominates over strain. If those areas furthermore show a local pressure minimum, it can be considered as a vortex [42].

$$Q = \frac{1}{2}\left(\|\mathbf{\Omega}\|^2 - \|\mathbf{S}\|^2\right) > 0 \tag{2.17}$$

It can be easily simplified [40] and then expanded for the particularities of 2D fields:

$$Q = -\frac{1}{2}\sum_{i,j}\frac{\partial u_i}{\partial x_j}\frac{\partial u_j}{\partial x_i} = -\frac{1}{2}\left[\left(\frac{\partial u}{\partial x}\right)^2 + \left(\frac{\partial v}{\partial y}\right)^2 + 2\frac{\partial u}{\partial y}\frac{\partial v}{\partial x}\right] \tag{2.18}$$

2.4.2 λ_2–criterion

This criterion is strongly related to the previous one, in that it corresponds to an eigenvalue of the matrix $\mathbf{M} = \mathbf{S}^2 + \mathbf{\Omega}^2$. In a 3D field, this symmetric matrix has three real eigenvalues. These values can be ordered as $\lambda_1 \leq \lambda_2 \leq \lambda_3$, since they are always real [40]. When λ_2 is negative, the flow can be considered to be vortical. Jeong and

Hussain derived from the Navier-Stokes equations that for a variety of conditions, two eigenvalues of the $\mathbf{M}$ matrix have to be negative in a vortex core. With respect to the Q-criterion, they also showed that $Q = -\frac{1}{2}(\lambda_1 + \lambda_2 + \lambda_3)$ [43].

However, this criterion presents several drawbacks. First of all, it was developed for a 3D flow and has to be adapted to a 2D one. Furthermore, eigenvalues of matrices are generally expensive to compute. Finally, there is no physical interpretation for positive eigenvalues [40].

2.4.3 Δ–criterion

This criterion is also related to the Q– and λ_2– criteria. It represents a polynomial inequality using two independent invariants of the $\nabla\mathbf{u}$ tensor. These values are Q and $R = \det(\nabla\mathbf{u})$. This criterion for detecting a vortex is given in Equation (2.19). Vortices can be defined as regions in which the eigenvalues of $\nabla\mathbf{u}$ are complex [41, 44].

$$\Delta = \left(\frac{Q}{3}\right)^3 + \left(\frac{R}{2}\right)^2 > 0 \tag{2.19}$$

A relatively large negative value of Q when compared to R is required. When the flow is incompressible, the characteristic equation of $\nabla\mathbf{u}$ is $\lambda^3 + Q\lambda - R = 0$ [41].

2.4.4 Γ_2–criterion

This 2D criterion was developed for PIV measurements. It represents how much the flow turns around the point in question, giving values between -1 for clockwise rotating flow, 0 for non-rotating flow and 1 for counter-clockwise rotating flow [38, 39].

Unlike other criteria, Γ_2 allows for the detection of the sense of the flow rotation. Other than that, it is easy to compute, provided that the grid connections are known. Figure 2.4 shows the values required for the calculations. $\overrightarrow{PM}$ is the vector from the point in which the criterion is being calculated to each of the neighbouring points for which there is velocity information. All of these points lie within an arbitrarily defined, small surface S, over which the integration is performed. $\overrightarrow{\Delta U}$ is the velocity difference vector, that is $\vec{U}_i - \vec{U}_A$, where $\vec{U}_A$ is the mean velocity in S and $\vec{U}_i$ is the velocity at each point. This allows to account for an average flow. θ_M is the angle between the two vectors $\overrightarrow{PM}$ and $\overrightarrow{\Delta U}$.

The calculation performed is shown in Equation (2.20), including both the analytical definition and the numerical implementation. $\vec{z}$ is the surface-normal vector, it just transforms a vector with one component, perpendicular to the surface (as is the case with the vector product) to a scalar.

$$\Gamma_2(P) = \frac{1}{S}\int_S \frac{\overrightarrow{PM} \times \overrightarrow{\Delta U} \cdot \vec{z}}{\left\|\overrightarrow{PM}\right\|\left\|\overrightarrow{\Delta U}\right\|}\, dS \simeq \frac{1}{N}\sum_{i=1}^{N} \sin\theta_M \tag{2.20}$$

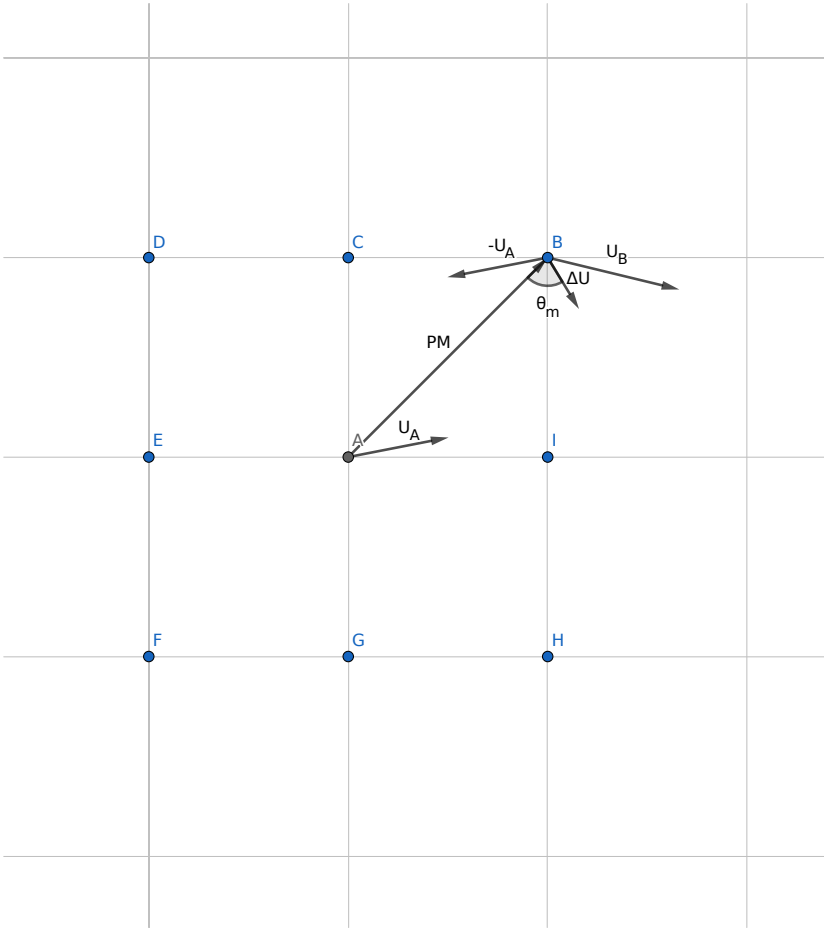

Figure 2.4: Γ_2–criterion representation

The value of the most important parameter, θ_M, is shown in Figure 2.4. Other than that, N is the number of points within the specified surface S.

Chapter 3

Methods

3.1 Setup

The code used to obtain the Computational Fluid Dynamics (CFD) results is part of the SU2 suite [8, 9]. It is an open-source, compressible solver, allowing the modelling of the problem using a moving mesh. The present section describes the parameters used as an input for the solver, as well as a description of the mesh and geometry and a comment on convergence.

3.1.1 Problem description

The cases considered for this project used a pitching motion shown in Eq. (3.1). The angle of attack, $\alpha(t)$, of the body varied between $\alpha_0 - \Delta\alpha$ and $\alpha_0 + \Delta\alpha$, where α_0 is the initial angle of attack and $\Delta\alpha$ is the pitching movement amplitude,

$$\alpha(t) = \alpha_0 + \Delta\alpha \sin(2\pi f t) \tag{3.1}$$

The motion parameters can be stated as two non-dimensional parameters: the reduced pitch rate, r and a reduced half-chord frequency, k,

$$\dot{\alpha}_0 = \Delta\alpha \cdot 2\pi \cdot f \tag{3.2}$$

$$k = \frac{2\pi \cdot f \cdot b}{U_\infty} \tag{3.3}$$

$$r = \frac{\dot{\alpha}_0 \cdot b}{U_\infty} = \Delta\alpha \cdot k \tag{3.4}$$

where f is the pitching frequency, $\dot{\alpha}_0$ the maximum pitching rate, b the airfoil half-chord ($0.02\,\mathrm{m}$) and U_∞ the freestream velocity.

The cases studied in the present work were defined by the motion parameter values shown in Table 3.1. These were used in previous experimental analyses, against which the results can be validated [6].

Case	α_0 [°]	$\Delta\alpha$ [°]	f [Hz]	k [–]	r [–]	c [m]	U_∞ [$\frac{\text{m}}{\text{s}}$]
Low frequency	10	5	1	0.0173	0.0015	0.04	7.25
Reference	10	15	2.5	0.0433	0.0113	0.04	7.25
Medium frequency	10	15	5	0.0867	0.0227	0.04	7.25
High frequency	10	15	7.5	0.1300	0.0340	0.04	7.25
Very high frequency	10	15	10	0.1733	0.0454	0.04	7.25
Low amplitude	10	5	5	0.0867	0.0076	0.04	7.25
High amplitude	10	20	5	0.0867	0.0303	0.04	7.25

Table 3.1: Case parameters

3.1.2 Mesh and geometry description

The mesh was generated with GMSH [10]. It is based on a Matlab script, that can generate both 2D and 3D computational domains around NACA4 series airfoils. The domain consists of an envelope around the airfoil, which has its leading edge at $x = -0.04\,\text{m}$, $y = 0$ and its trailing edge at $x = 0$, $y = 0$. Upstream, the domain is limited by a semi-circumference centred on the coordinate origin, its radius is $r = 2\,\text{m}$, 50 times the chord. Downstream, it forms a rectangle, with $\Delta x = 2\,\text{m}$, $\Delta y = 4\,\text{m}$. The geometry is shown in Figure 3.1.

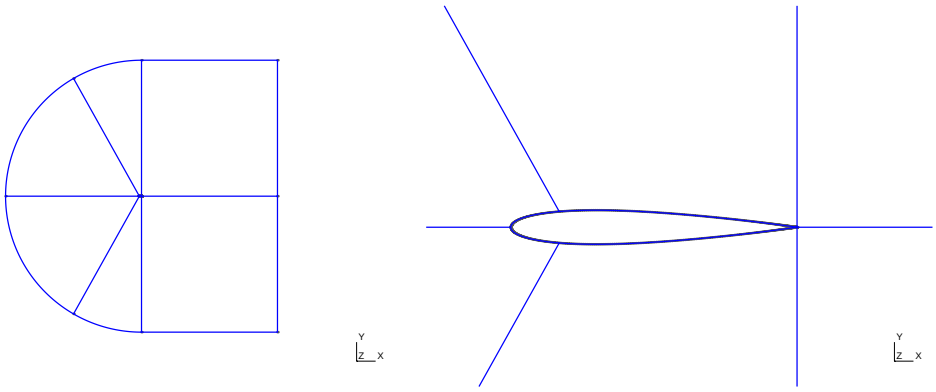

(a) Full domain (b) Zoom-in around the airfoil

Figure 3.1: Geometry of the computational domain

The mesh is generated on the surface normal direction by applying a first spacing of $\Delta s = 3.794 \times 10^{-5}\,\text{m}$. This value would lead to a $y+$ close to 1 for a flat plate. In the simulations, the value of this boundary layer parameter oscillated between 0.5 and 3, which lies within the viscous sublayer. After the first cell, each consecutive one had a height 20% larger than the previous one.

In the direction parallel to the surface, there are a set number of points, in this case $N = 200$, along the suction and pressure surfaces. The total number of elements is 20 367, all of which are quadrilaterals. The mesh is structured, though SU2 treats it as an unstructured grid. A close-up of the mesh is displayed in Figure 3.2.

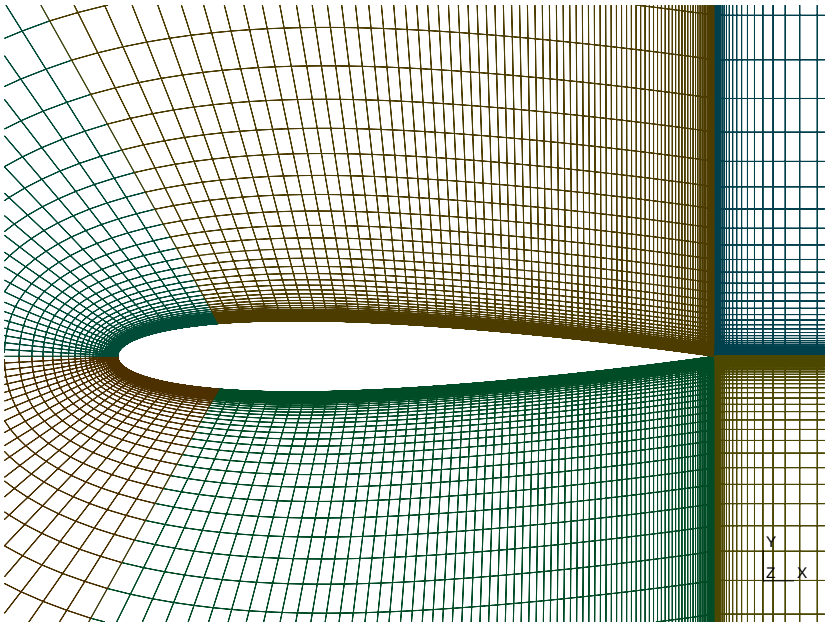

Figure 3.2: Mesh around the airfoil

The mesh is similar to the URANS one described by Güner on his Masters' thesis for the same geometry [45]. Furthermore, the mesh parameters were close to those described by Gómez Gómez for a converged mesh over a flat plate [46]. Therefore, a mesh study was not conducted and it was considered sufficiently converged.

3.1.3 CFD description

The current problem was solved through unsteady RANS, using the Menter Shear Stress Transport (SST) turbulence model, as implemented by the SU2 code. The Spalart-Allmaras model was also tested, but it produced results further away from the experimental data. That was expected, since the S–A model is appropriate at mostly attached flow conditions.

3.1.3.1 Numerical methods

The unsteady simulations used a second order dual time-stepping method, with a constant time step for each simulation. The number of internal iterations within each external time step was set to be 150 and the Courant-Friedrich-Lewis number for these was set to 20. Finally, since the mesh was not too complex, there was only one multi-grid level set. Higher numbers could result in numerical instabilities appearing in the simulations. Other than that, the numerics of the solver were not touched.

3.1.3.2 Boundary conditions and dynamic mesh

Two boundary conditions were applied: one on the surface of the airfoil and another on the far-field. The first one was set as an adiabatic, no-slip wall boundary. The second

one was a Far-field boundary, in which the angle of attack was set to the corresponding α_0. It needed the free-stream temperature or density for initialisation, the first of which was set to 288.15 K. Furthermore, it required the Mach number, calculated from the experimental and numerical values, as $Ma_\infty = \frac{U_\infty}{\sqrt{\gamma R T_\infty}} = 0.0213$. The free-stream velocity value was set to $U_\infty = 7.25\,\frac{\mathrm{m}}{\mathrm{s}}$.

Finally, the code required the corresponding Reynolds number, which is used with the ideal gas law and the Sutherland viscosity correlation to obtain the free-stream pressure. The chord Reynolds was set to $\mathrm{Re}_c = \frac{c \cdot U_\infty}{\nu_\infty} = 20000$, close to the one reported for the experiments.

The turbulence intensity, by default, was of 5%. The experimental report states that the wind tunnel had an expected turbulence value of around 1.2%. One of the cases was run with a different turbulence intensity in order to check the influence of this parameter. It was shown not to affect significantly the solution.

The mesh moves rigidly, without deforming, around the quarter chord. This point is placed at $x = -0.03\,\mathrm{m},\ y = 0$. The pitching angular frequency around the Z axis, ω, was set to the value given in Table 3.1 for each test case, multiplied by 2π, with the corresponding amplitude and a 0° phase offset.

3.1.4 Solution convergence

In periodic simulations, there are several areas in which convergence is needed. Since the motion is repeated with a constant frequency, it is expected that the values at the same time point since the start of each cycle will converge. This is known as the cycle-to-cycle convergence.

Furthermore, when the number of time steps within a cycle is increased, the solution will change. After a certain number of time steps per cycle, it can be considered converged. Cycle-to-cycle convergence is a pre-requisite to evaluate this time step convergence.

Finally, the static, non-moving test cases were also required to reach time convergence. This kind is analogous to the previously stated cycle-to-cycle convergence for the dynamic cases.

3.1.4.1 Cycle-to-cycle convergence

Cycle-to-cycle convergence is verified by looking at the same phase angle, or time, in each cycle. If the difference in the instantaneous values of the load coefficients is small enough, no more cycles are required. There was no way to perform this action automatically, so it was decided to first use as much as 10 cycles and check afterwards $c_*(t+T) - c_*(t)$, where c_* denotes any of the load coefficients and T is the period of the motion.

A graphic way of looking at these differences is shown in Figure 3.3a for a large time step and Figure 3.3b for a smaller time step. The figures show the value of c_n for the first, second to last and last cycles simulated. The shorter time step case was initialised with result files of the longer time step one, instead of using far-field flow conditions.

It was also seen that this convergence took more cycles to be achieved at higher frequencies. This behaviour was expected, since the physical time is lower for these. In general, when initialising from a static or dynamic solution, five cycles are enough for convergence for all those cases. This setting was used, for example, in Figure 3.3b. On the other hand, when initialising from the free-stream conditions, ten cycles were more than enough, as shown in Figure 3.3a.

3.1.4.2 Time step convergence

Time step convergence can be verified by comparing the time response of the force and moment coefficients in several different simulations. Each of these uses a certain number of steps per cycle. For the aforementioned reference case, the setups used are shown in Table 3.2.

Case	Δt [ms]	Timesteps per cycle
1	2	200
2	1	400
3	0.5	800
4	0.2	2000
5	0.1	4000

Table 3.2: Time step convergence parameters for $f = 2.5\,\mathrm{Hz}$

In Figure 3.3c, a comparison between the normal force coefficients obtained in each of the five cases is performed, around stall onset. This region is zoomed in, since even Case 2 in Table 3.2 was mostly converged outside it. It is shown that the differences between Cases 4 and 5 were minimal, therefore settling for the first one, which requires half the number of time steps. This convergence was faster for higher frequency cases, though it was decided to keep constant the number of time steps per cycle.

Finally, each simulation could be initialised with the last output file of a previous calculation for the same test case. This helped with cycle-to-cycle convergence and reduced the number of cycles until it could be reached. In the end, when initialised from other files, as little as five cycles consistently achieved converged results.

3.1.4.3 Static case convergence

Static cases were solved by using two methods: a dual time-stepping URANS one, similar to the dynamic cases, and a steady RANS one. The unsteady simulations proved

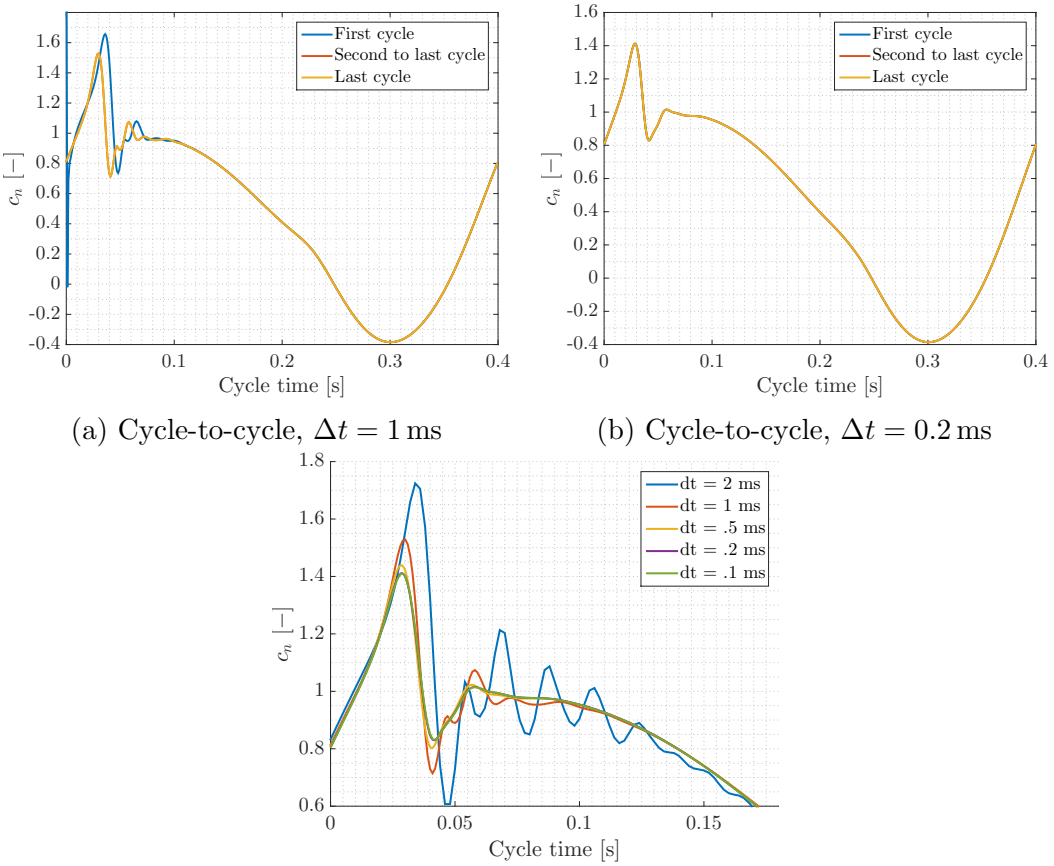

(a) Cycle-to-cycle, $\Delta t = 1\,\text{ms}$

(b) Cycle-to-cycle, $\Delta t = 0.2\,\text{ms}$

(c) Timestep zoom-in

Figure 3.3: Convergence of the normal force coefficient, reference case

more accurate, especially at higher angles of attack, though more computationally intensive. However, in mostly attached flow cases this could be attributed to a solution that was not fully converged.

3.2 Detection of vortices

As discussed earlier, vortex detection is a difficult subject. Therefore, different criteria can be more useful for different flows, each one having its own advantages and disadvantages.

When attempting to obtain the vortex core locations, several methodologies can be used. The simplest one is finding a local minimum in pressure, or pressure coefficient. This one is especially useful when examining the surface distribution of the flow variables. It can also be used in experimental studies, though the chordwise sensor resolution is low. For example, Zanotti et al. include 22 pressure sensors, compared to the 200 surface nodes in the present mesh [47].

Other vortex detection criteria require access to the whole flow field as explained previously, in Section 2.4. The present section presents two complementary approaches for this detection and compares their results in practice.

3.2.1 Surface pressure coefficient

One of the usual methods for determining the vortex positions is by finding the pressure minima over the surface of the airfoil, as a function of time. This only allows for a rough estimation of the chordwise location of the vortex core, without taking into account other parameters, such as its strength and distance from the airfoil's surface. However, it is relatively simple and takes less memory and computing power than full flow field methods.

For the present work, this method was implemented on the basis of the Matlab `findpeaks` function, which provides information about the relative maxima of a series.

3.2.2 Full field methods

Another approach implemented included a two-step method for determining the vortex core location over the full field. First, high vorticity areas were identified in the flow solution, by means of the Q–criterion. While in theory vortices are characterised by $Q > 0$, practically speaking another cutoff value was required. In this case, analysing the CFD results, it was determined that $Q > 100\,000\,\frac{1}{s^2}$ provided reasonable separation between vortices and other flow phenomena.

However, the flow turning around the leading edge has a high value of the presented vorticity criteria and it is difficult to distinguish the vortex cores appearing close to this point and the flow turning phenomenon. The contours of the Q–criterion, as well as the instantaneous flow vectors for one such case are shown in Figure 3.4. While there is clearly a vortex core and it is within the high vorticity region, the whole region is marked as a possible vortex, including the boundary layer at the leading edge.

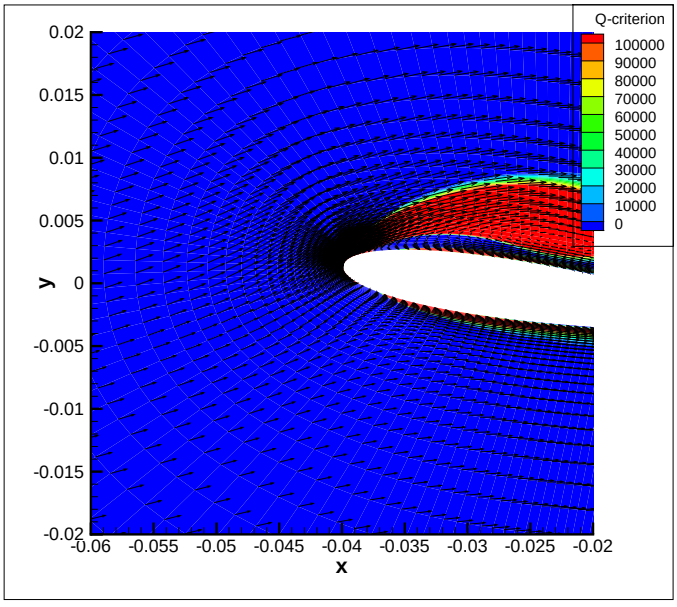

Figure 3.4: Close-up of the leading edge for $f = 5\,\text{Hz}$, $\Delta\alpha = 15°$ and $\alpha = 18°$

This is one of the main points that need to be addressed: a too low Q cutoff value does not allow to differentiate between separate, interacting flow structures, while a higher value can cause structures to be missed. This kind of trade-off has to be considered when processing the data.

Once the high vorticity regions have been identified, the vortex core can be established as either the lowest pressure or the highest Q value. Both of them are close to the suction peak in the aforementioned leading edge region. Therefore, they do not allow for an easy and systematic determination of the vortex core in that region.

3.2.3 Comparison of methods

The vortex core criteria are essentially coincident up to the dissipation of the vortex, for the large vortical structures associated with dynamic stall onset. Therefore, it does not matter which one is used, though the Q-criterion maxima should be a better fit for weak vortices with respect to the background pressure gradients. Therefore, it is the one employed in the processing.

Figure 3.5 shows a comparison of the detected position for two cases and both methods. The x locations given by both of them are strongly correlated, though their differences are patent. First of all, the surface pressure can be tracked more easily than the vortex cores. This is especially clear in the very high frequency case, shown in Figure 3.5b.

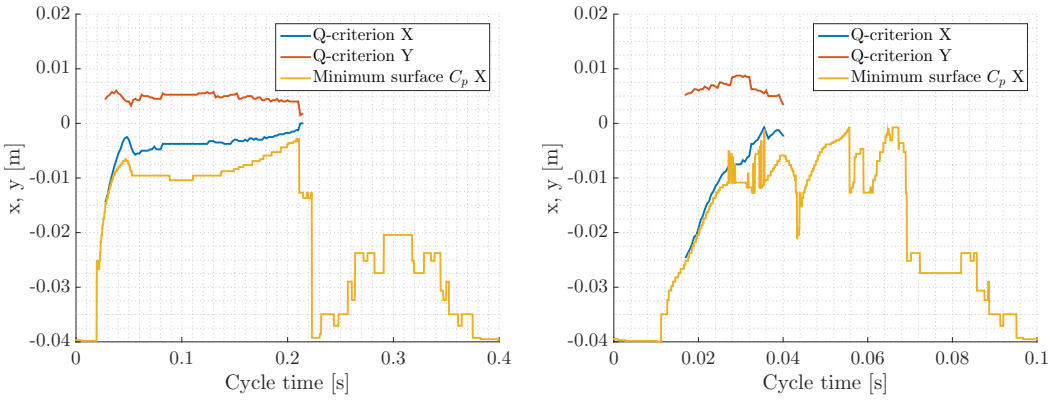

(a) Reference (b) Very high frequency

Figure 3.5: Comparison between vortex core and surface pressure criteria for two cases

The surface pressure criterion is also able to differentiate between the suction peak and the actual location of the vortex before the Q-criterion contours separate. Surface pressure represents the vortex behaviour close to the leading edge more clearly, for every condition studied. However, it has another drawback: it underestimates the core velocity, especially once the vortex starts to decelerate, close to the trailing edge. The "overshoot" obtained by means of the vortex core criteria is larger than the one estimated by the pressure surface.

3.3 Separation point detection

The separation point is an important flow feature in dynamic stall and it is also related to the presence of vortices. It strongly affects the pressure distribution, so the Leishman-Beddoes model uses this point as a parameter.

The method employed to find the separation point relies on this phenomenon leading to a change in the sign of the velocity in the boundary layer. The friction coefficient, C_f, is defined as the ratio between the surface friction and the dynamic pressure. In these cases, a zero in C_f would imply the presence of separation, with a sign change in the relative flow/surface velocity close to the boundary. The CFD software provides the components of this coefficient along the y and x axes. The latter is chosen in order to find the recirculation point. Figure 3.6 includes a sketch showing this solution.

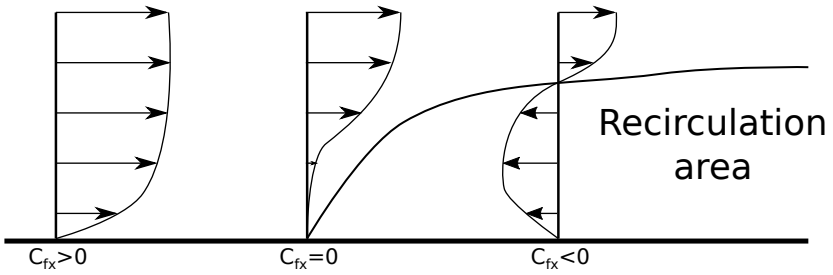

Figure 3.6: Location of the separation point from zero friction coefficient

However, since the airfoil is moving, the CFD x axis does not necessarily coincide with the chord. Therefore, sometimes zeroes of the friction coefficient in the x direction appear at points close to the leading edge without actual separation. In order to avoid those spurious points and to implement the zero finding procedure, a simple algorithm was designed, the flowchart of which is shown in Figure 3.7.

Furthermore, the algorithm just obtains the first flow reversal point. Sometimes, there may be several other $C_f = 0$ points, due to the presence of up to three vortices, which lead to a change in the sense of the flow. It is simple to extend it for finding other points. Finally, in those points for which there is no separation in the suction side, at low angle of attack, the value of f is taken as 1: separation occurs at the trailing edge.

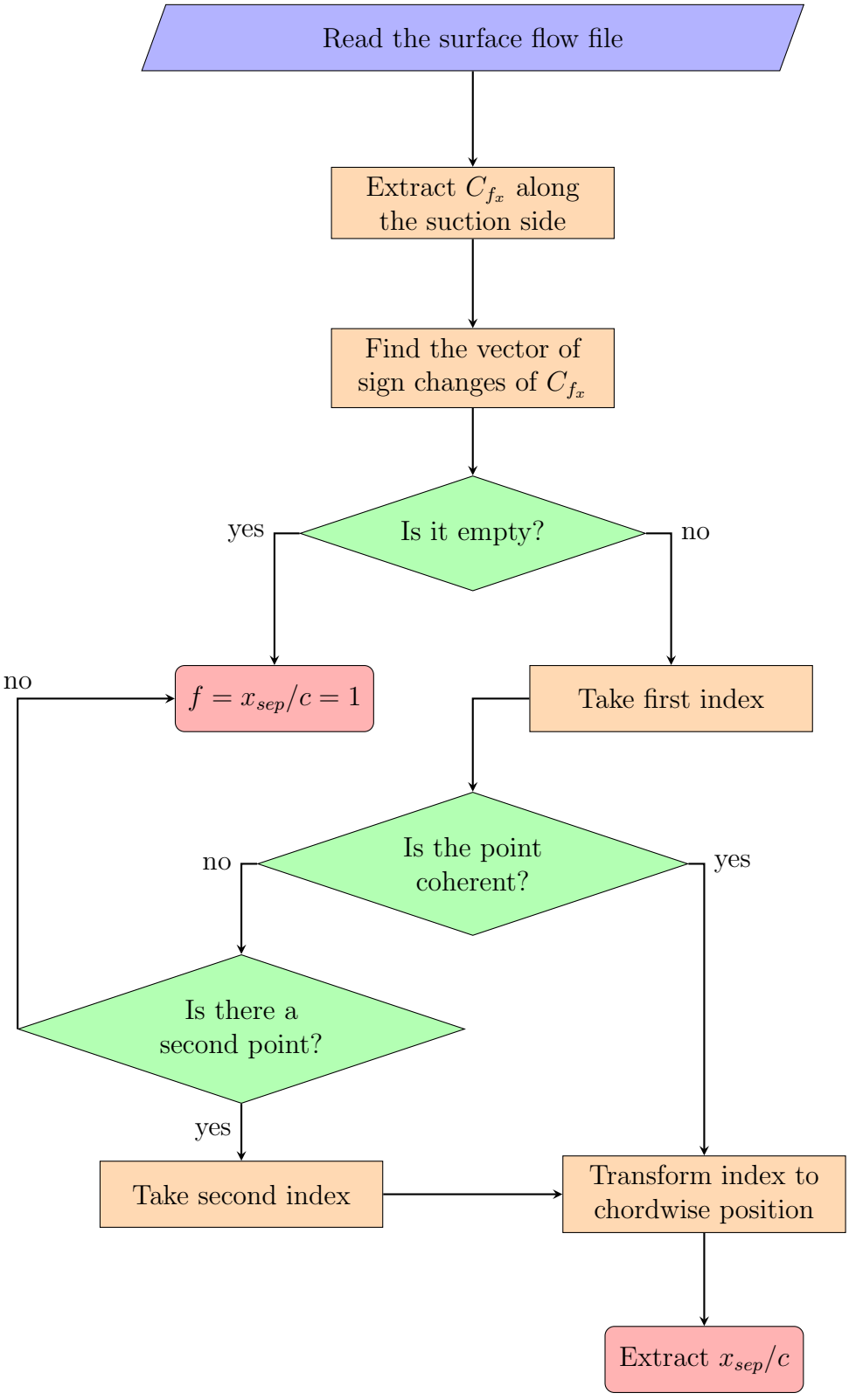

Figure 3.7: Flowchart describing the algorithm for determining the separation point

Chapter 4

Static results

The present chapter presents the load curves obtained for the profile, from several CFD analyses. The mesh is the same as the one for the dynamic cases, though in this case it remains static, with a different angle of attack set in the far field boundary for each case.

4.1 Load curves of the airfoil

The analysis use the same setup implemented for the dynamic, moving cases. It was decided to use the k–ω SST turbulence model, since it provides generally more accurate results at higher angles of attack than the Spalart-Allmaras model.

This was confirmed by the curves obtained, the tendencies and magnitudes estimated from the first model were more closely aligned with those observed from the experiment. This is seen in Figure 4.1, comparing four sets of results against the experimental data, for the three main coefficients. The cases used were both static and dynamic, i.e., with dual time-stepping. As explained before, two different turbulence models were evaluated.

Figure 4.1 shows the polar of the airfoil for the three load coefficients and the studied cases at the corresponding flow conditions. It can be seen that the normal force coefficient for the SST model closely matches that of the experiments. However, at very high angles of attack it seems to slightly overestimate the normal force.

Similar conclusions can be drawn for the moment coefficient, plotted against angle of attack in Figure 4.1a. However, it appears that the chordwise force coefficient (Figure 4.1c) is significantly underestimated, by a somewhat constant offset. However, the tendencies shown are essentially the same as the experiments suggest. This could be due to a constant offset when measuring the chordwise force.

Other than that, the normal force coefficient is overestimated at low angles of attack. This is most likely due to the presence of a laminar separation bubble, which

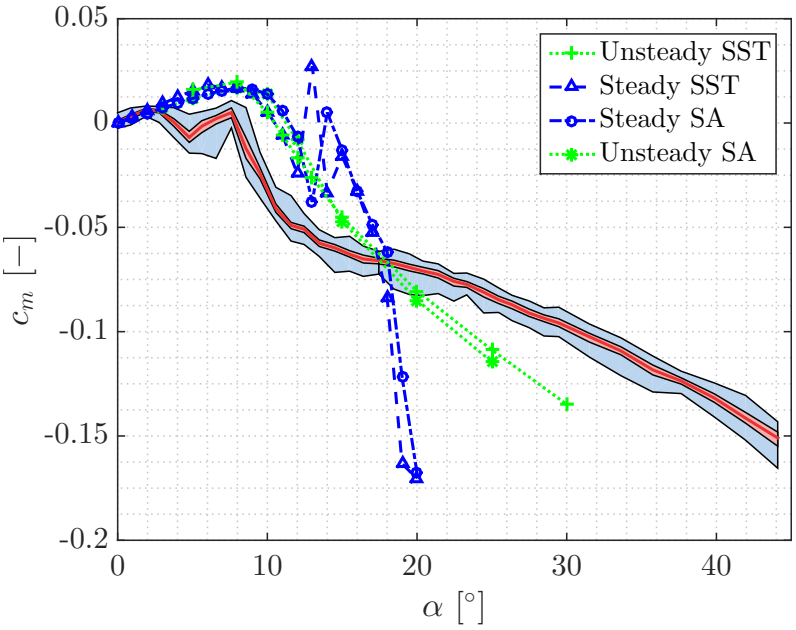

(a) Moment coefficient

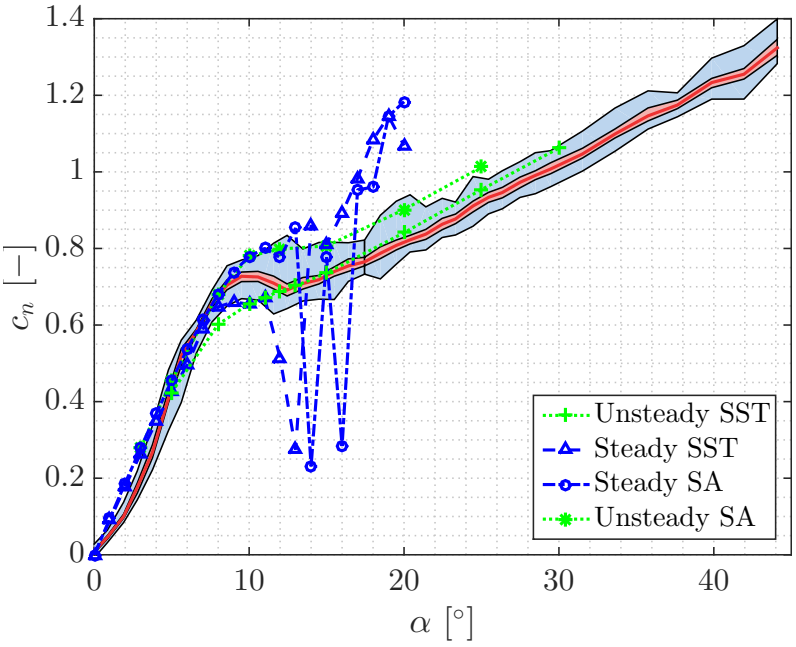

(b) Normal force coefficient

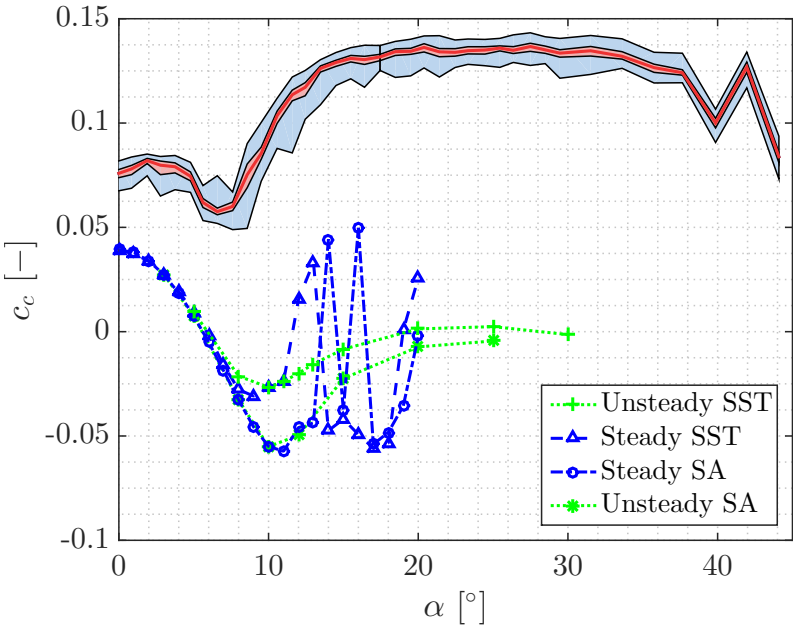

(c) Chordwise force coefficient

Figure 4.1: Comparison between experimental and CFD results of the load coefficients

cannot be modelled by normal turbulence closures, without a transition model.

Another important point is the difference between static and dynamic analyses. It is clear that the results are essentially identical at low angles of attack, before the static stall starts. However, once it has started, the results diverge. The static cases oscillate wildly, while the dynamic cases show a clearer trend, without many oscillations. A comparison of these two is shown in Figure 4.2. Two different angles of attack are compared between the two cases: 5° and 20°. While the criteria for convergence were reached on the first case for the static simulation, the second was still oscillating after 20 000 iterations. Therefore, dynamic CFD is trusted in situations with detached flow, confirming the trend shown in Figure 4.1.

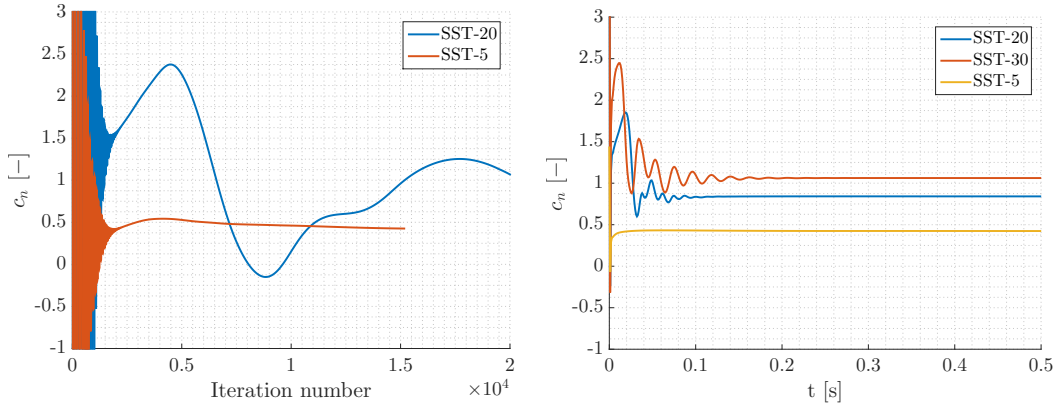

(a) Steady CFD, $\alpha = 5°,\ 20°$ (b) Unsteady CFD, $\alpha = 5°,\ 20°,\ 30°$

Figure 4.2: Comparison between CFD convergence of the normal force coefficient

Therefore, one could say that the static cases are not converged. However, since this problem requires a dynamic calculation, with dual time-stepping, it is not expected to be a barrier.

The main conclusion one can draw from this section is that, in spite of the low Reynolds conditions, which are not optimal for turbulence modelling, the SST dynamic results show a very strong agreement with experimental data, even at relatively high angles of attack, except for the chordwise force. The main differences have to do with laminar boundary layer conditions at low angles of attack, which are explored in further detail in Section 4.3.

4.2 Separation point

An important input for the Leishman-Beddoes model is the chordwise location of the separation point as a function of the angle of attack. This has been obtained as the point closest to the leading edge in which there is flow reversal. The algorithm shown in Figure 3.7 is applied to each surface flow file.

The Leishman model used to predict the separation point from the angle of attack is described in Equation (2.6). This model estimates the separation point, f, as a function of the angle of attack and using three parameters. The best-fit value of these parameters, as obtained using the `fit` Matlab function, is shown in Table 4.1.

Parameter	Value	Unit
α_1	7.106	$^\circ$
S_1	1.644	–
S_2	3.569	–

Table 4.1: Parameters for the Leishman separation model

A comparison of the result of the separation point model, using the coefficients in Table 4.1 and the actual point obtained from the CFD data is shown in Figure 4.3.

While the agreement between model and steady CFD data is pretty good, at high angles of attack there is a relatively large variation. This is expected, since in that region the flow is highly unsteady. Depending on the times examined, the result will change. Even though there is some variation, the model is smooth and able to overcome this problem. This variation is minimised by the Unsteady RANS results, shown as green triangles, which are also given more weight in the curve fit.

The standard way of estimating $f(\alpha)$ from experimentally measured load data is by curve-fitting normal force data using Equation (2.5). The results of this calculation, applied to the CFD lift curves, are plotted in Figure 4.4, along with the model obtained directly from the separation point locations of Figure 4.3. It can be seen that the results

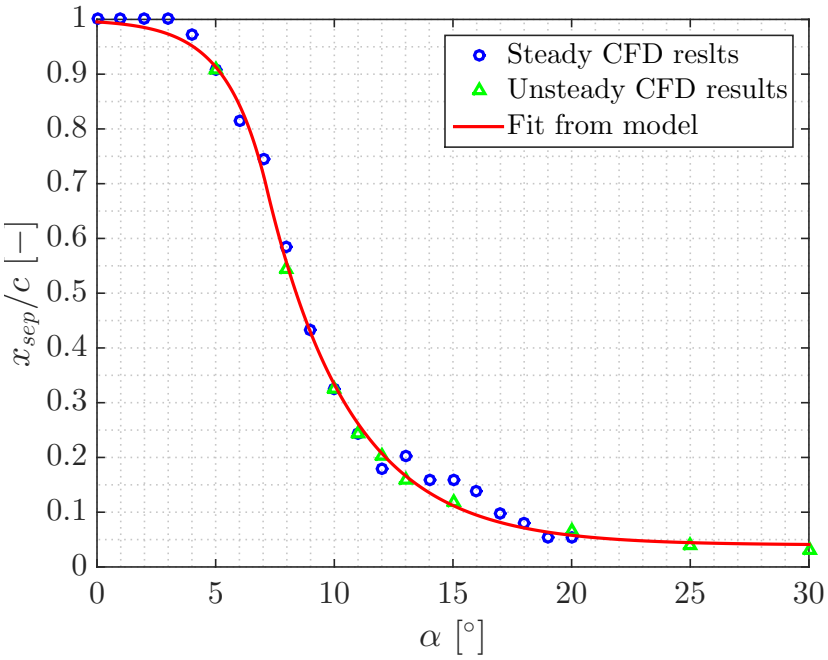

Figure 4.3: Comparison between Leishman model and CFD results for separation

from Equation (2.5) and the model of Equation (2.6) do not match each other at high angles of attack. The tendencies are more or less correct, but while some disagreement with the steady calculations was expected, the magnitude and disagreement with the unsteady results is too high. Therefore, it can be established that either the Kirchhoff model underestimates the normal force coefficient or Equation (2.5) overestimates the position of the separation point.

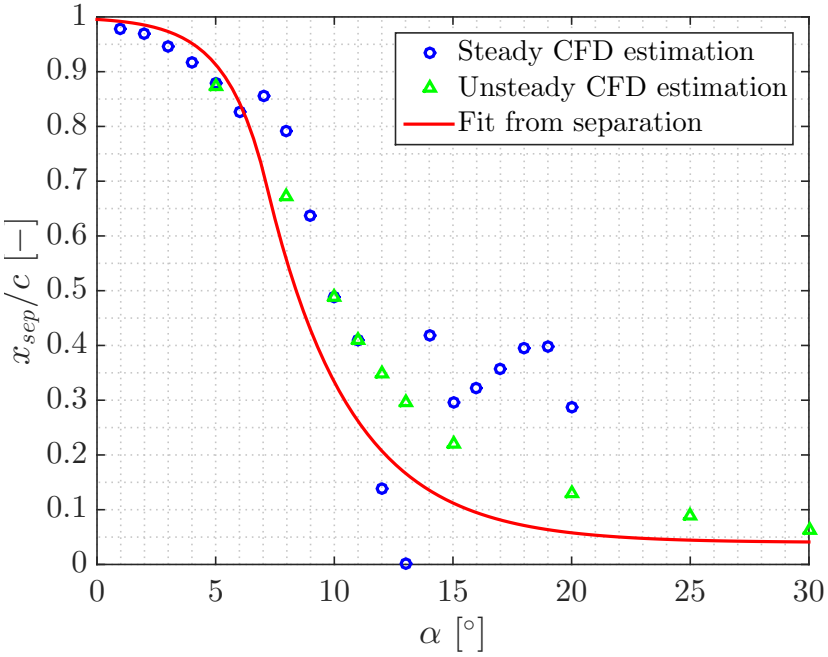

Figure 4.4: Comparison between separation position estimated by Kirchhoff theory and CFD fitting

Another fit that can be performed is the one shown in Equation (2.9), for the moment coefficient. The first term is referred to as g, a non-dimensional variable, defined by Equation (4.1), as the difference between the centre of pressure and the quarter chord. Consequently, it ranges from 0.25 to -0.75, from the leading edge to the trailing edge, respectively.

$$g(f) = \frac{c_m|_{1/4}}{c_n} = \frac{1}{4} - \frac{x_{cp}}{c} \tag{4.1}$$

The curve fit was performed within the Matlab script. Its resulting parameters are shown in Table 4.2.

Parameter	Value	Unit
K_0	0.034 62	–
K_1	-0.2926	–
K_2	0.1852	–
m	0.4671	–

Table 4.2: Parameters for the Leishman-Beddoes fit of the non-dimensional centre of pressure

Interestingly, K_0, the parameter that relates c_n and c_m for attached flow, is greater than 0. Therefore, the centre of pressure is upstream the quarter chord, even at low angles of attack. The fit, shown in Figure 4.5, is generally quite good, even for flow showing near-complete separation. In that range, dynamic simulations are given higher weights in the curve fit, since they capture better the flow behaviour.

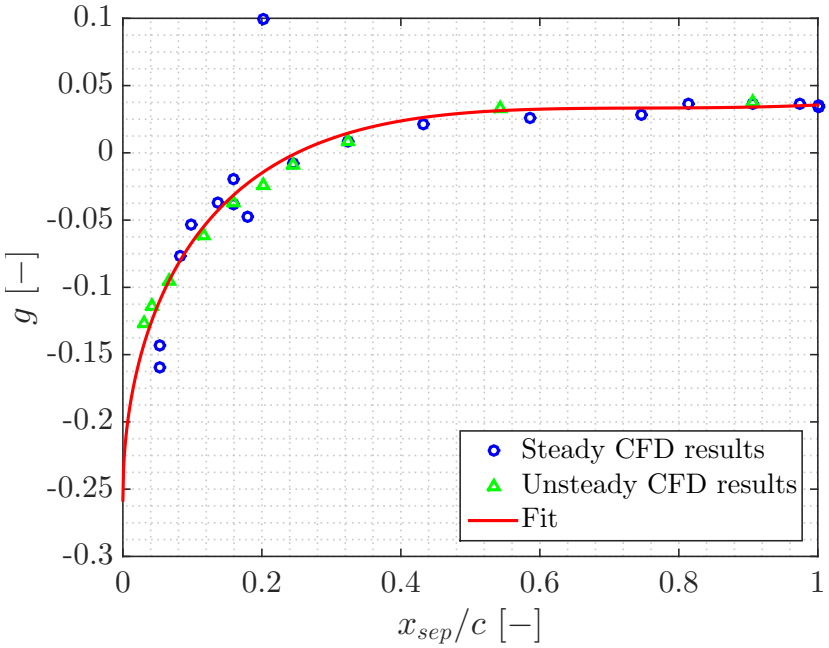

Figure 4.5: Comparison between the CFD non-dimensional position of the centre of pressure and a fit for the data

4.2.1 Experimental separation results

A comparison between the results for the separation point in CFD and the experimentally determined values is performed. It should be noted that the experimental apparatus was not able to obtain directly the position of this point, but it could be estimated from Equation (2.5), as explained previously. Therefore, both the fit from the CFD separation point and the values derived from Equation (2.5) are compared. It is expected that, due to the good agreement between the load coefficients, the estimated separation points should be comparable.

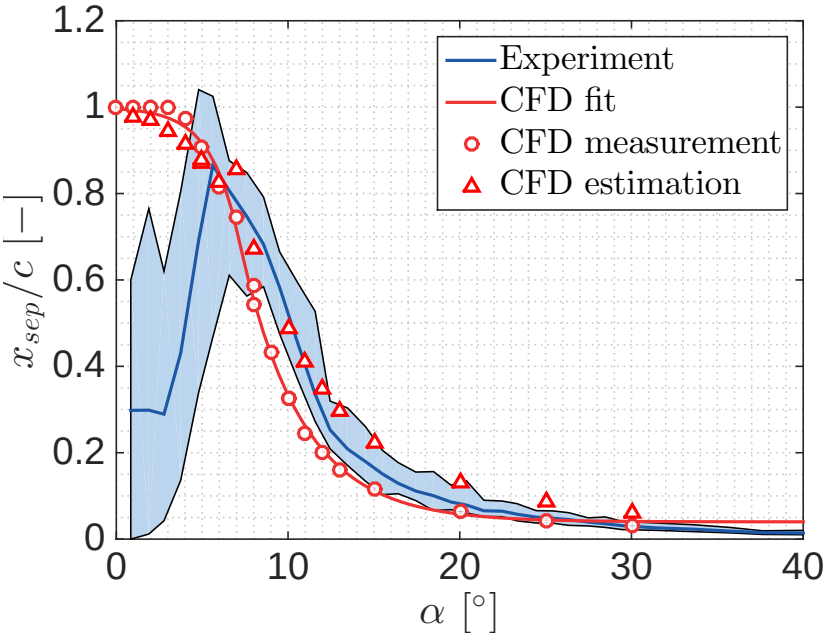

Figure 4.6: Separation point, experiment and CFD comparison

The results of the comparison are shown in Figure 4.6. This plot compares the experimental results derived from Equation (2.5), in blue and their corresponding confidence bounds to the Equation (2.6) and Table 4.1 fit, in red. The actual separation point values for steady and unsteady simulations are red circles, while the estimation from CFD, using Equation (2.5), is plotted as red triangles.

The strong disagreement at low angles of attack has to do with the aforementioned laminar separation bubble, which is unfortunately not modelled in the current CFD scheme. This behaviour is not included in the Leishman-Beddoes model. Other than that, as expected, the Equation (2.5) values match quite well, while the Equation (2.6) fit imply an earlier separation point.

4.3 Stall onset description

The present section compares static stall onset to the theoretical description in Section 2.1, summarising some of the findings from the CFD results and their possible impact on dynamic stall.

First of all, the laminar separation bubble does not appear in CFD at low angles of attack. This is expected, since the fully turbulent model employed cannot represent a laminar boundary layer, nor the transition to turbulence. Figure 4.7 plots the variation of c_n with α for angles of attack up to 10°. It compares the experimental measurements to the predictions obtained from the various CFD schemes. It can be seen that there is a big difference between the experimental results and all the models for $\alpha < 5°$. The experiments show a normal force deficit, not present in the CFD data.

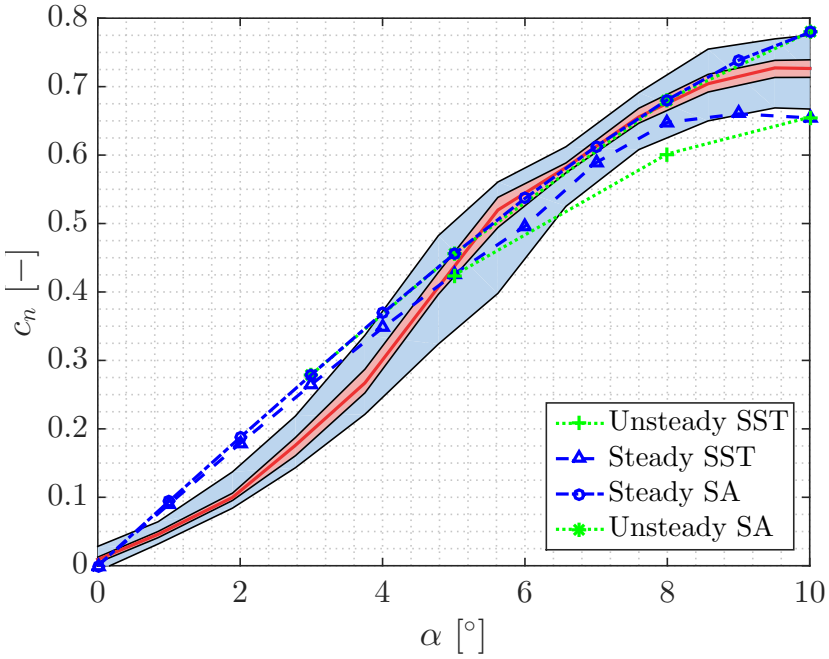

Figure 4.7: Normal force coefficient at low angles of attack

The Baş-Çakmakçıoğlu transition model was tried, as implemented by SU2, in order to model the presence of the aforementioned separation bubble. However, the solver did not predict significant differences between this model and the Spalart-Allmaras, fully turbulent one. Table 4.3 shows a comparison of the normal force coefficient results for all three turbulence models, as well as the experimental results, interpolated to the corresponding angle.

α [°]	Menter SST	Spalart-Allmaras	Baş-Çakmakçıoğlu	Experimental
0	~ 0	~ 0	~ 0	0.009
1	0.090	0.094	0.088	0.054
2	0.179	0.187	0.175	0.109
3	0.265	0.279	0.258	0.197
4	0.348	0.369	0.337	0.301
5	0.426	0.455	0.408	0.436

Table 4.3: Normal force coefficient values for three different turbulence models and the experiment

The results show an approximately linear behaviour for all three models, including the one representing the laminar-to-turbulent transition. Therefore, the LSB is not modelled at the present flow conditions, by any of the closures. This leads to some problematic results regarding vortex onset, which is considered by classical representations of the flow behaviour as occurring due to the interaction of the LSB and the extending separation region.

Therefore, the load coefficient evolution for the experimental results is compatible at low angles of attack with leading edge stall, presenting a sudden collapse in the value of the lift and normal force coefficients. However, the CFD simulations predict fully attached flow at low angles of attack and trailing edge stall at high angles of attack, with a recirculation bubble appearing at the trailing edge and progressively increasing its size in the upstream direction until the full airfoil is stalled, as shown in Figure 4.3. The change in c_n is smooth, without large discontinuities, and is plotted in Figure 4.1b.

Chapter 5

Dynamic cases

The present chapter outlines the main results obtained from the dynamic case simulations. First, it presents the reference case, in Section 5.1. The time response of the flow around the airfoil and its effects on the corresponding changes in the load coefficients are detailed. Then, an overview of several important flow structures is shown.

After that, in Sections 5.2 and 5.3, two other cases are shown, explaining the differences between the conditions at higher and lower frequencies. The behaviour of separation and reattachment and its evolution as the parameters are modified, is included in Section 5.4. The specific aspects of the vortices' evolution, including their onset and shedding, are detailed in Section 5.5.

Finally, the parameters required for the Leishman-Beddoes model are obtained from the simulation data in Section 5.6. A comparison of the criteria reviewed in the literature is included in Section 5.7.

5.1 Reference case

In this case, the parameters are $\alpha_0 = 10°$, $\Delta\alpha = 15°$, $f = 2.5\,\text{Hz}$. The results for the time evolution of the load coefficients over one complete cycle are shown in Figure 5.1. They are compared to the experimental results, in red. The red regions represent the experimental interquartile range. The agreement is quite good, especially for the moment and normal force coefficients (Figures 5.1a and 5.1b, respectively).

The chordwise force coefficient, in Figure 5.1c shows worse agreement between the simulated and experimental data. This could be due to either bad modelling from the part of the simulation or inaccuracies due to the experimental procedure. The experimental loads are obtained from the difference between wind on and wind-off measurements in order to separate the inertial and aerodynamic loads. This subtraction becomes less accurate as the magnitude of the aerodynamic load decreases. The magnitude of the chordwise force is much lower than that of the normal force and

hence the experimental data of Figure 5.1c are expected to be less accurate than those of Figure 5.1b.

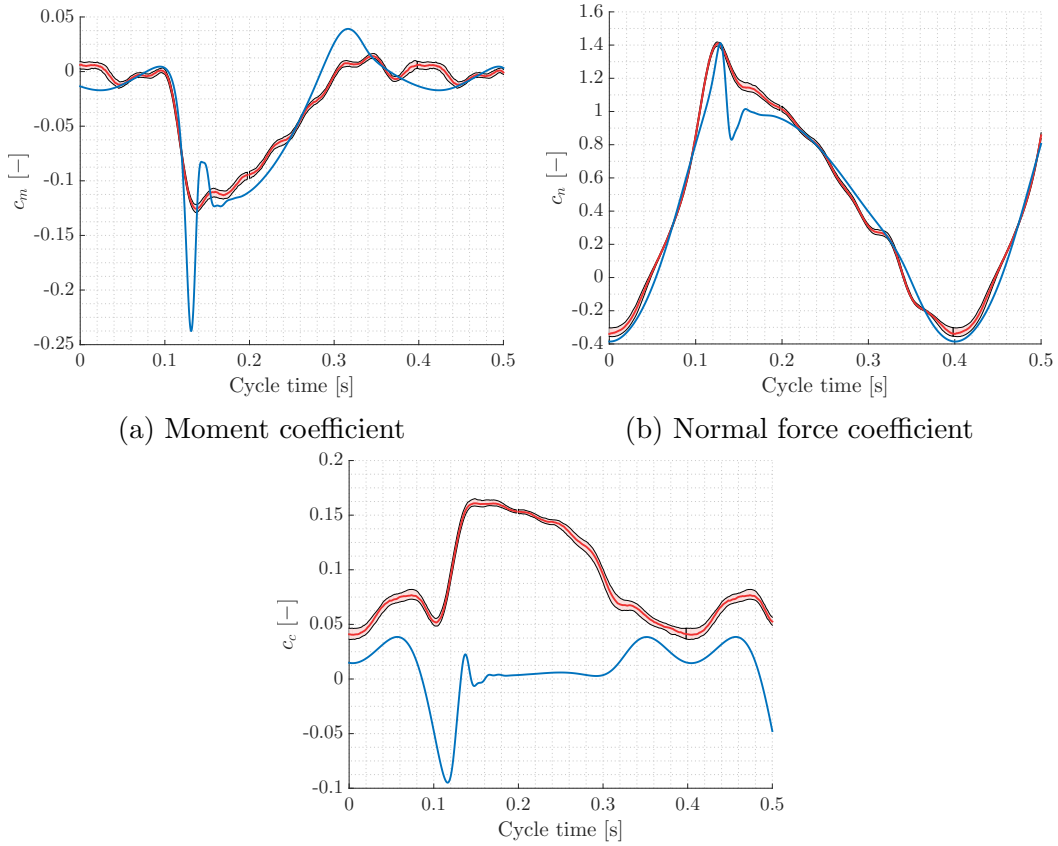

(a) Moment coefficient

(b) Normal force coefficient

(c) Chordwise force coefficient

Figure 5.1: Load coefficient time response for the reference case, compared to the experimental results

5.1.1 Time evolution of each cycle

The present subsection details the time evolution of the flow around the airfoil in each cycle, starting at $t_0 = \frac{N-1/4}{f} = 0.4 \cdot N - 0.25 \cdot T$ [s], where f is the cycle frequency, in Hz; T the cycle period, in s and $N > 1$ the cycle number. A phase shift of $-\pi/2$ rad was added. The simulation used a sine movement, shown in Equation (3.1), without any phase shift. This shift is included because it is considered that it leads to a more intuitive representation of the results. It is shown in Equation (5.1). At $t_{cycle} = 0$, $\alpha = -5°$ and the flow is fully attached, unlike for the unshifted cases.

$$\alpha(t) = \alpha_0 + \Delta\alpha \sin\left(2\pi f t - \frac{\pi}{2}\right) \tag{5.1}$$

Upstroke ($t \in]0, 0.1[$ s) In this part of the cycle, the airfoil is moving nose-up. The flow is attached and the relation between the angle of attack and the normal force

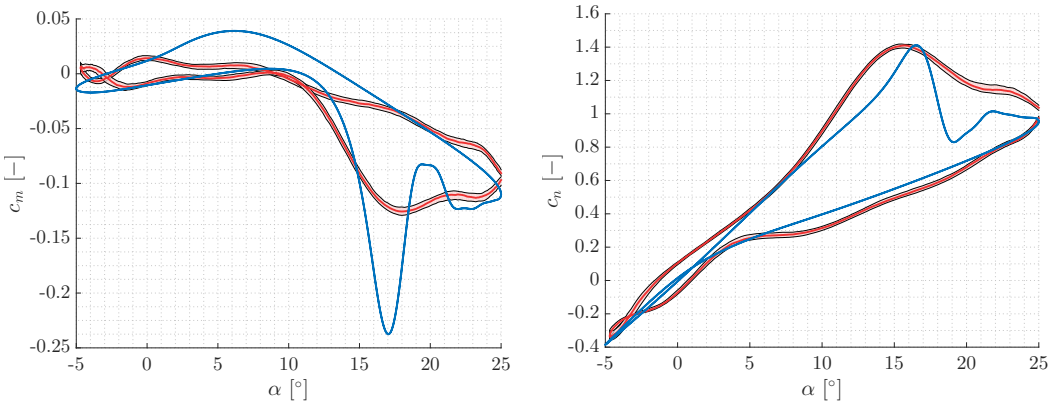

(a) Moment coefficient

(b) Normal force coefficient

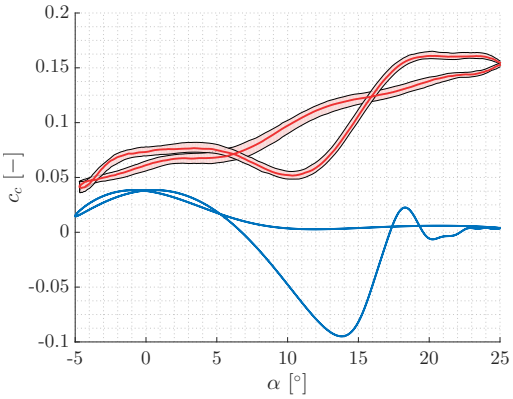

(c) Chordwise force coefficient

Figure 5.2: Load coefficient angle of attack response for the reference case (blue), compared to the experimental results (red)

coefficient is linear. This coefficient is plotted in Figure 5.2b, as a function of the angle of attack. The flow is mostly attached, though close to $t = 0.1$ there is some flow reversal in the trailing edge. At this instance $\alpha = \alpha_0 = 10°$.

Delayed stall ($t \in]0.1, 0.1172[\,\mathrm{s}$) After reaching α_0, the normal force coefficient continues increasing. This increase is still approximately linear with the angle of attack at first. It is due, mainly, to a relatively strong suction peak in the leading edge, which continues increasing, as shown in Figures 5.3a and 5.3b.

Just after $t = 0.1$, the absolute minimum of the chordwise force coefficient is reached. This can be seen in Figure 5.1c. At that point, the moment starts a sudden decrease, crossing the $c_m = -0.05$ threshold at $t = 0.1172\,\mathrm{s}$, $\alpha = 14.0°$.

Moment stall ($t \in]0.1172, 0.1285[\,\mathrm{s}$) At this instance, moment stall occurs. There is a sudden, large drop in the moment coefficient, due to the appearance of a low pressure bubble close to the mid-chord, which subsequently moves downstream. This bubble affects also the normal force coefficient, changing its curvature from close to zero to positive. The bubble can be seen around the mid-chord in Figures 5.3c and 5.4c.

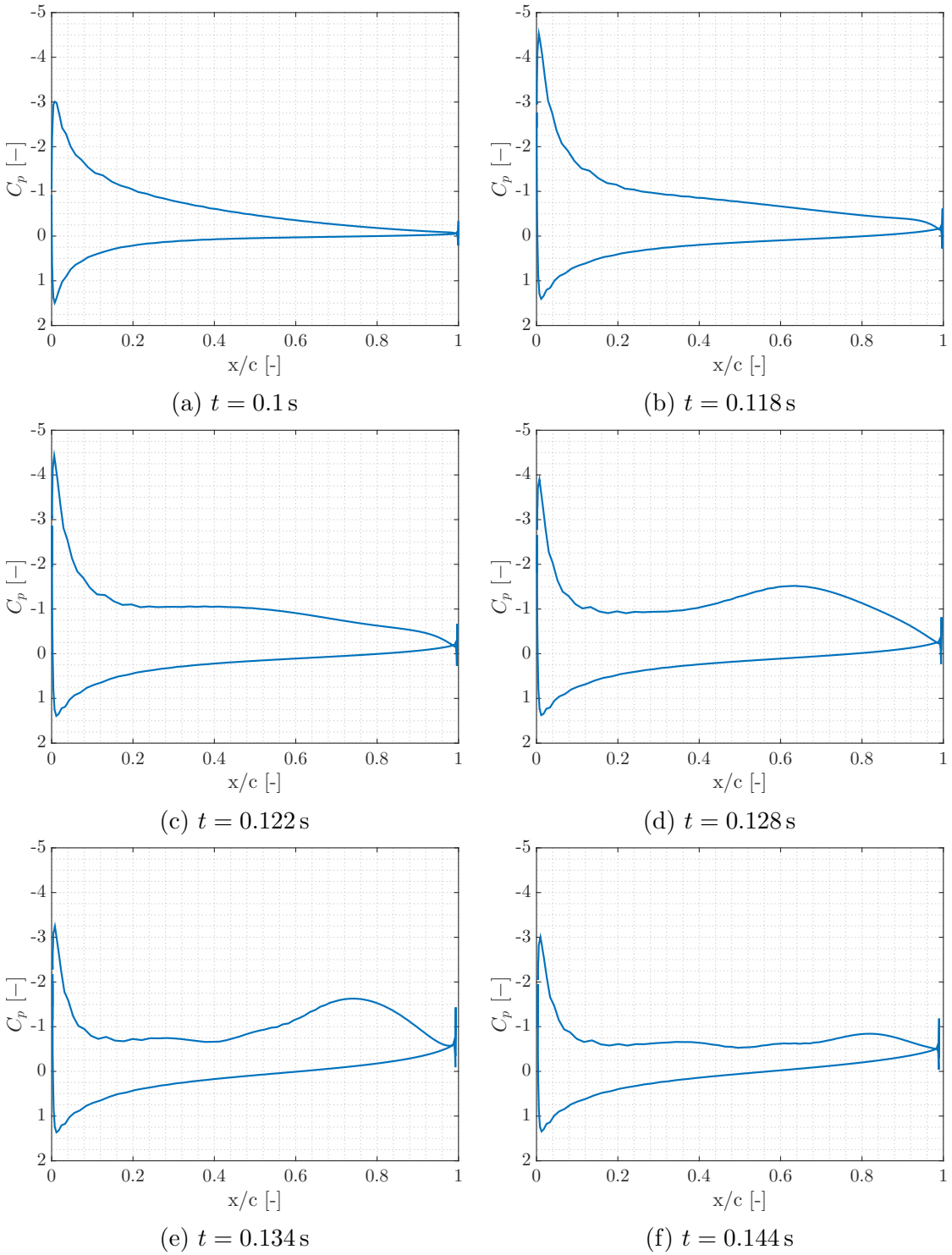

(a) $t = 0.1\,\mathrm{s}$ (b) $t = 0.118\,\mathrm{s}$

(c) $t = 0.122\,\mathrm{s}$ (d) $t = 0.128\,\mathrm{s}$

(e) $t = 0.134\,\mathrm{s}$ (f) $t = 0.144\,\mathrm{s}$

Figure 5.3: Pressure coefficient distribution on the surface of the airfoil for selected time instances

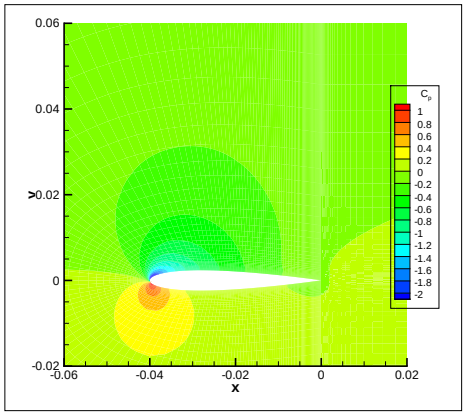

(a) $t = 0\,\mathrm{s}$

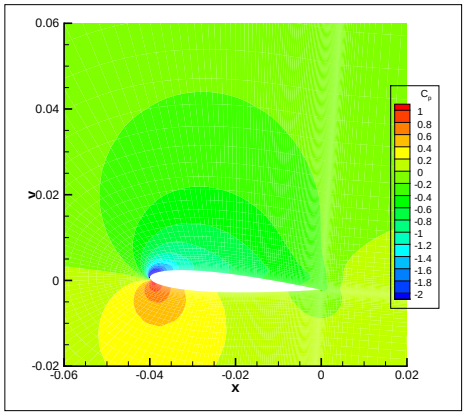

(b) $t = 0.118\,\mathrm{s}$

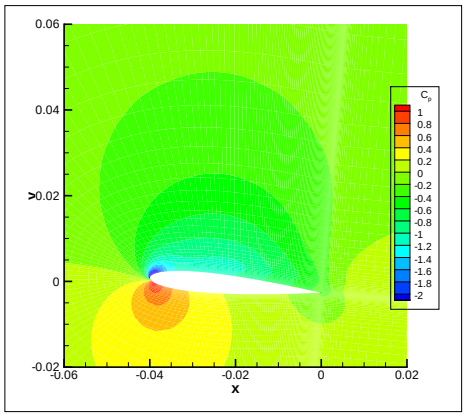

(c) $t = 0.122\,\mathrm{s}$

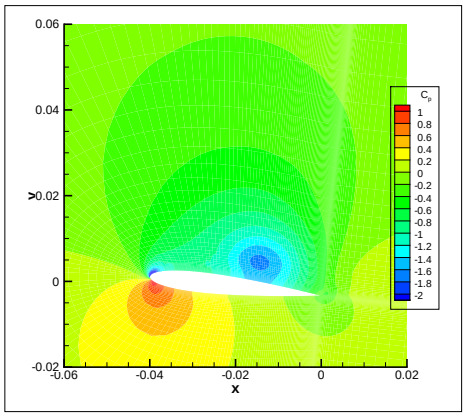

(d) $t = 0.128\,\mathrm{s}$

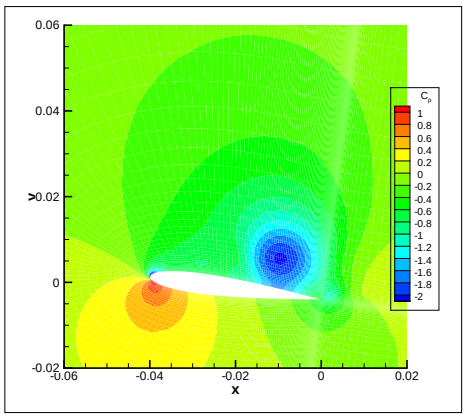

(e) $t = 0.134\,\mathrm{s}$

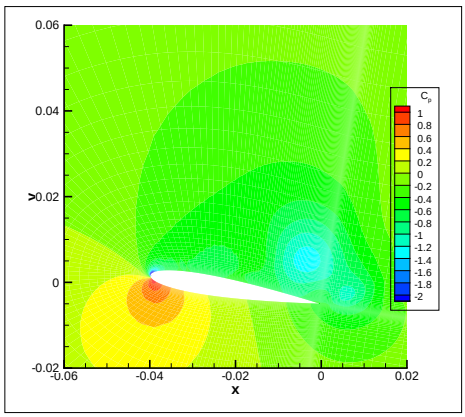

(f) $t = 0.144\,\mathrm{s}$

Figure 5.4: Pressure coefficient field for selected time instances

The normal force coefficient increases faster than the linear relation described above, due to the low pressure region. This region helps counteract the weakening of the leading edge suction peak. Therefore, there is an absolute maximum of the normal force coefficient around $t = 0.1285\,\mathrm{s}$. Figure 5.3 shows that the leading edge suction peak reaches a value of $C_p = -4.5$ at $t = 0.022\,\mathrm{s}$ in Figure 5.3c. Afterwards, it starts to decrease, to $C_p = -4.0$ in Figure 5.3d and to $C_p = -3.0$ in Figure 5.3f.

Lift stall ($t \in]0.1285, 0.2[\,\mathrm{s}$) While the low pressure bubble continues strengthening, it starts to move perpendicularly to the chord, thus leaving the surface of the airfoil, as witnessed by the location of the pressure minimum in Figures 5.4d and 5.4e. The increased strength of the vortex cannot compensate for the decrease in suction around the leading edge. As a consequence, the normal force decreases. Furthermore, when the vortex reaches the trailing edge, it starts to weaken. Figures 5.4e and 5.4f show this weakening. At time $t = 0.144\,\mathrm{s}$, the impact of the bubble over the surface is minimal, as seen in Figure 5.3f.

At this point, the moment has reached its minimum and is recovering. This is due to the bubble weakening, as well as a general increase in pressure along the suction side, which produces a positive moment.

When the normal force coefficient reaches a minimum, the moment has recovered somewhat. At this point there is also a local chordwise force coefficient minimum.

After these two minima, the normal force coefficient starts to recover, while the moment coefficient decreases again. The low pressure bubble, is at this point located close to the trailing edge, as seen in Figure 5.4f. It starts to strengthen somewhat, as a second, weak, vortex sheds from the suction peak and merges with the original one.

Downstroke ($t \in]0.2, 0.4[\,\mathrm{s}$) Finally, the airfoil starts moving nose-down and the flow begins to reattach. The return to attached flow conditions occurs at $\alpha \simeq 1°$.

5.1.2 Flow characteristics

The two main flow structures determining the loads over the section are the leading edge suction peak and the low pressure bubble. Also, the bubble/vortex-related separation point is crucial for the model to be fitted.

5.1.2.1 Suction peak

The suction peak is characteristic of configurations at moderate and high angles of attack. It is shown by Chandrasekhara et al. [16] that for low Mach number flow conditions, the local flow can reach transonic conditions. In those cases, the magnitude of the suction peak has a strong effect on dynamic stall.

However, the Mach number for this study was considerably lower. Therefore, the shock-related stall onset does not occur here. Furthermore, there are two main factors which contribute to the suction peak not being as critical as a static case would suggest and therefore reducing the adverse pressure gradient. These two are the low Reynolds number, which reduces the magnitude of the suction peak and the presence of a leading edge jet which energises the boundary layer, therefore delaying separation.

5.1.2.2 Low pressure bubble

The low pressure bubble is similar in behaviour to the vortices usually described in the dynamic stall literature. It leads to a rotational flow, associated with a relatively low pressure.

It exhibits high values for the vorticity criteria used. It is a highly viscous flow, so the velocity only increases slightly close to the bubble core. The structure is shown in Figure 5.5, which plots the velocity vectors over the C_p map. The main vortex appears on the right hand side, with a relatively low pressure and turning vectors, leading to a strong recirculation. There is a second vortex closer to the leading edge. It is also associated with a local pressure minimum, albeit much weaker.

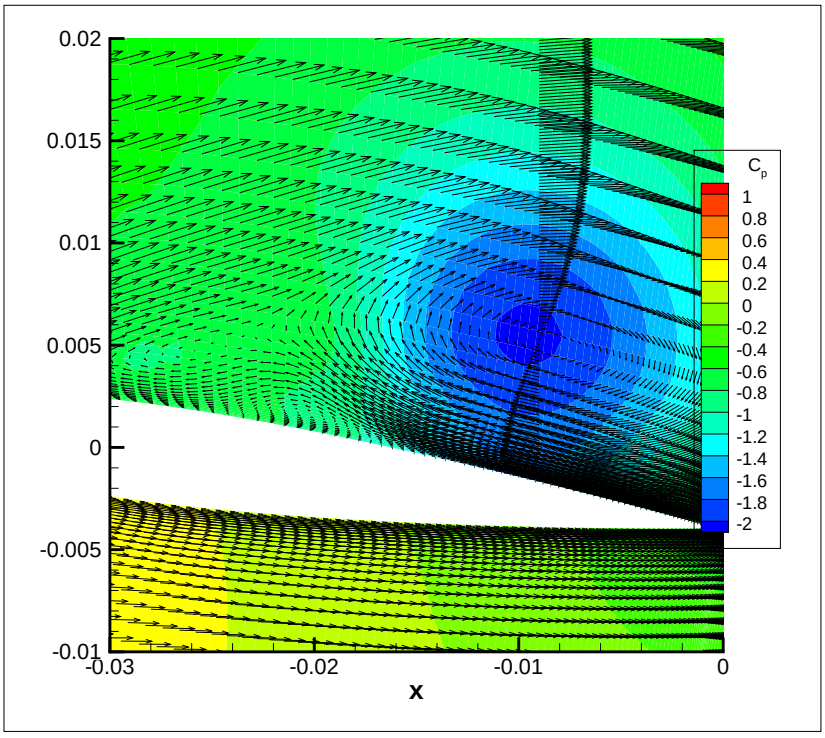

Figure 5.5: Closeup of the vortical structure at $\alpha = 17.6°$, upstroke

In the dynamic stall literature, the vortex is usually stated to be as moving at 30 % to 60 % of the freestream velocity. However, the present simulations suggest that the vortex moves much more slowly. At its peak, the vortex propagation speed barely

reaches 20 % of the freestream velocity. This is consistent with the observations inferred from the experimental data (see Section 2.2).

The generation of this vortex is related to the flow in the boundary layer. As the separation point moves upstream, a rotational flow starts to appear, with the freestream moving in one sense and the separation region in the other. At some point, a low pressure region separate from the suction peak appears, therefore fulfilling the criteria for a vortex.

In conclusion, the low pressure bubble appears as a result of recirculation and moves downstream, acting as a leading edge vortex, even though its root cause is trailing edge separation. Once the vortex becomes strong enough to be visible and starts propagating downstream, its behaviour is similar to that of the leading edge vortex reported in the high Reynolds literature, although its speed of propagation is significantly lower.

5.1.2.3 Separation point

The separation point is obtained according to the algorithm shown in Figure 3.7, which allows for robust and easy separation detection. The results are shown in Figure 5.6. They are compared to the static model defined in Equation (2.6) and plotted in Figure 4.3.

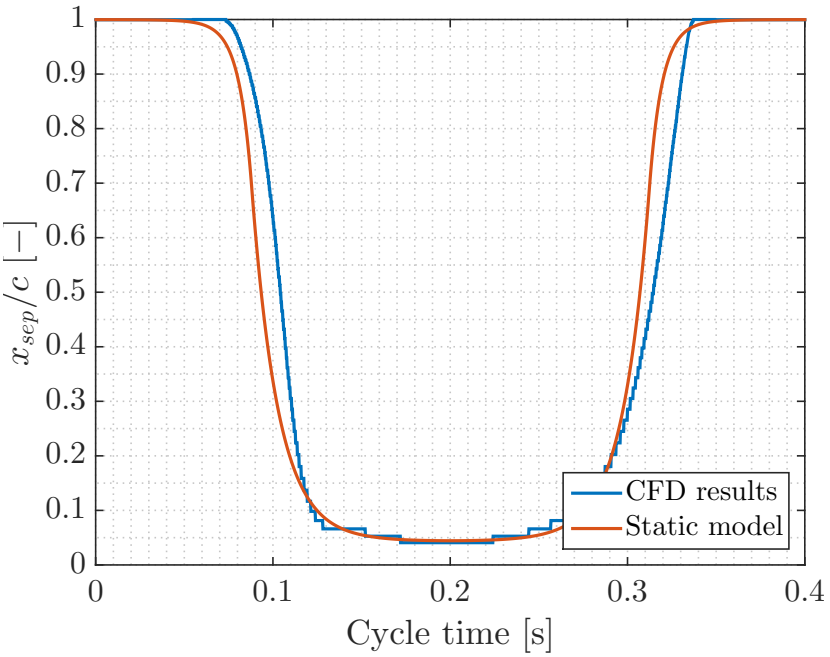

Figure 5.6: Comparison between Leishman static model and CFD results for separation

There is a very clear delay between the static model and the unsteady separation point locations.. This delay is approximately constant and corresponds to the sum of two of the parameters of the Leishman-Beddoes model. Therefore, the Leishman model can be considered a valid simplification of the flow behaviour, as represented by the simulation. From the data, one can estimate the value of $t_p + t_f = t_a = 0.0123\,\text{s}$.

5.2 Low frequency case

For this case, as shown in Table 3.1, the parameters are $\alpha_0 = 10°$, $\Delta\alpha = 5°$, $f = 1\,\text{Hz}$. Therefore, it has the lowest reduced pitch amplitude of the cases studied in this work.

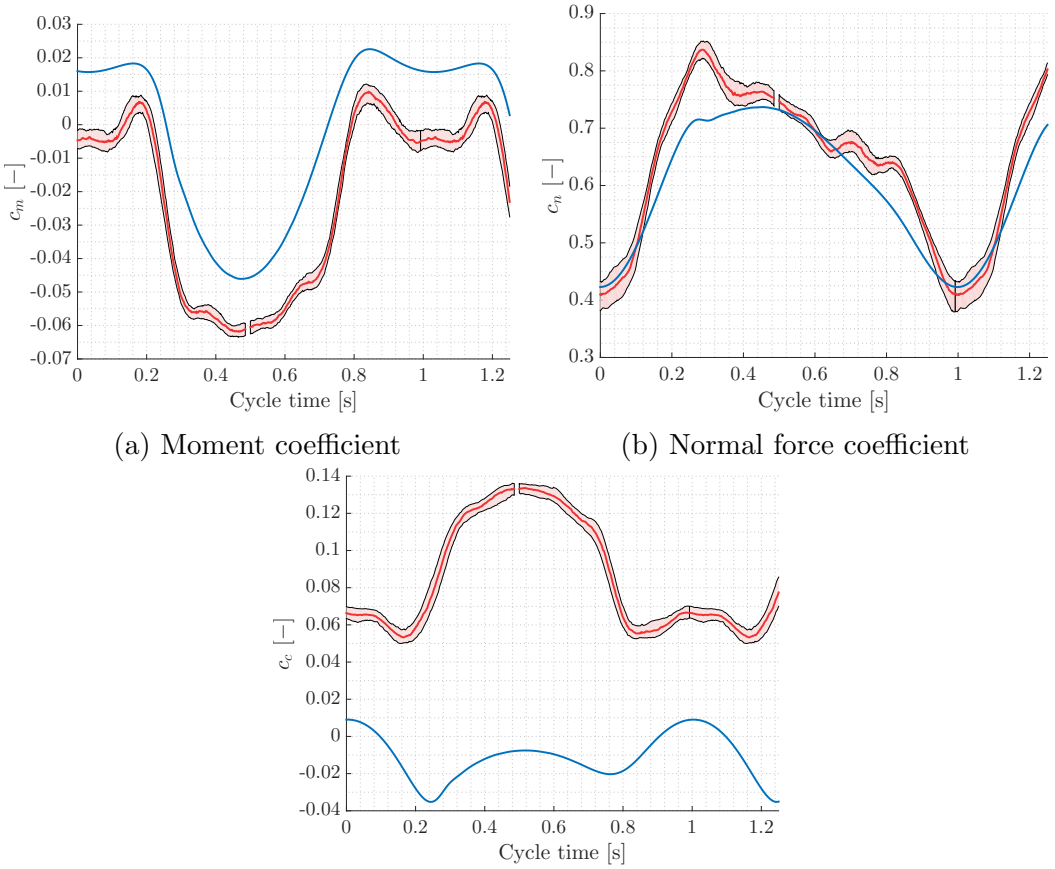

(a) Moment coefficient

(b) Normal force coefficient

(c) Chordwise force coefficient

Figure 5.7: Coefficient time evolution for the low frequency case, compared with the experimental results

In Figure 5.7, the CFD load coefficients are plotted against cycle time, as was done for the reference case. It can be seen that the c_m behaviour predicted by the simulation is quite similar to the experimental measurements, except for a constant offset. This is confirmed by plotting against the angle of attack, in Figure 5.8a.

As in the previous case, the chordwise force does not quite match the experimental results, though the minimum occurs at the same time. The normal force coefficient, both in Figures 5.7b and 5.8b, indicates that the vortex strength is not quite matched by the simulation: the normal force is considerably underestimated. This could be due to a weak suction peak, since after stall the behaviour is matched again more closely.

The same classification performed for the reference case can be applied here.

1. Upstroke: it takes place at $t \in]0, 0.25[$ s

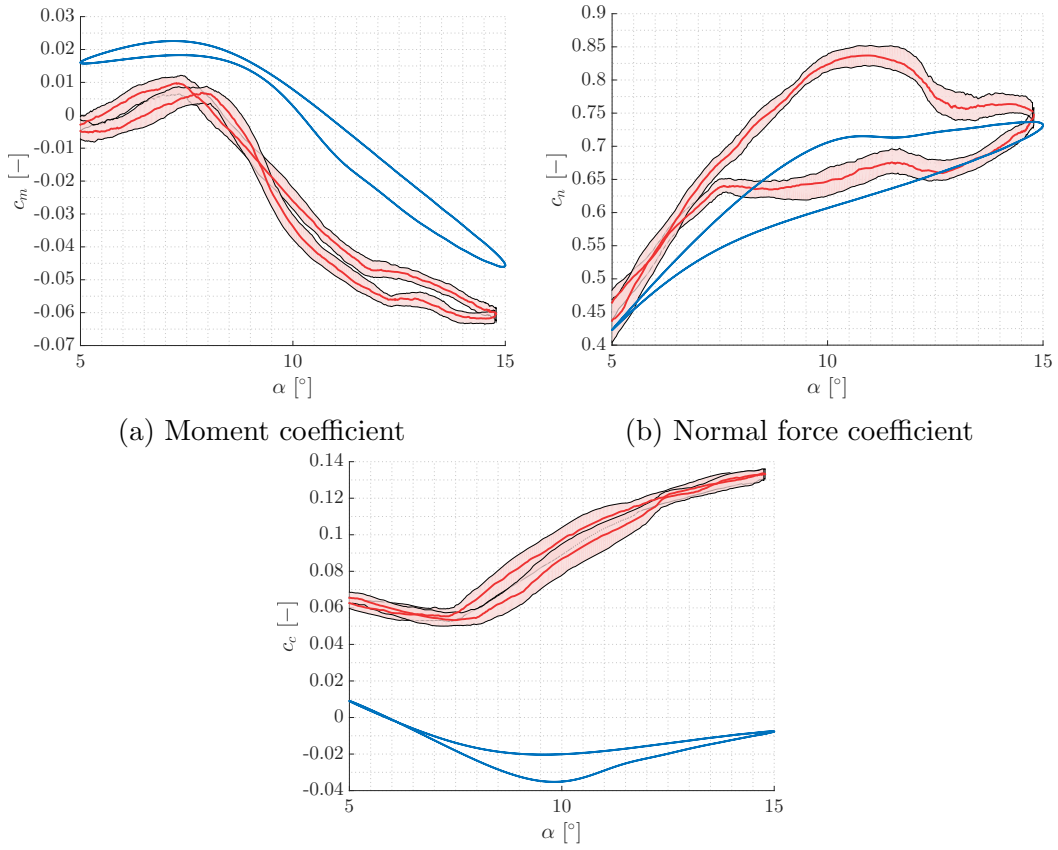

(a) Moment coefficient

(b) Normal force coefficient

(c) Chordwise force coefficient

Figure 5.8: Coefficient angle of attack evolution for the low frequency case, compared with the experimental results

2. Delayed stall ($t \in]0.25, 0.256[$ s): the c_m starts to decrease sharply, due to the influence of the strengthening of the vortex. At $t = 0.256$ s, $c_m = 0$.

3. Moment stall ($t \in]0.28, 0.276[$ s): while the vortex core pressure decreases, the moment collapses and the maximum c_n appears at $t = 0.276$ s. Unlike the reference case, the curvature is negative all the time before the collapse starts.

4. Lift stall ($t \in]0.276, 0.50[$ s): unlike the reference case, the vortex strengthening is the only driving force behind the moment collapse and the lift recovery. Due to a weaker suction peak, the normal force decreases, although it is quickly overtaken by the vortex. The maximum c_n, as well as the minimum c_m, occur at $t = 0.50$ s, the maximum angle of attack.

5. Downstroke ($t \in]0.50, 1.00[$ s): in this phase, the vortex remains in the same position, close to the trailing edge. Finally, it starts to dissipate, without shedding.

5.3 Very high frequency case

For this case, as shown in Table 3.1, the parameters are $\alpha_0 = 10°$, $\Delta\alpha = 15°$, $f = 10$ Hz. The flow characteristics are not too different from other cases, in general, though there

are some points that are worth mentioning.

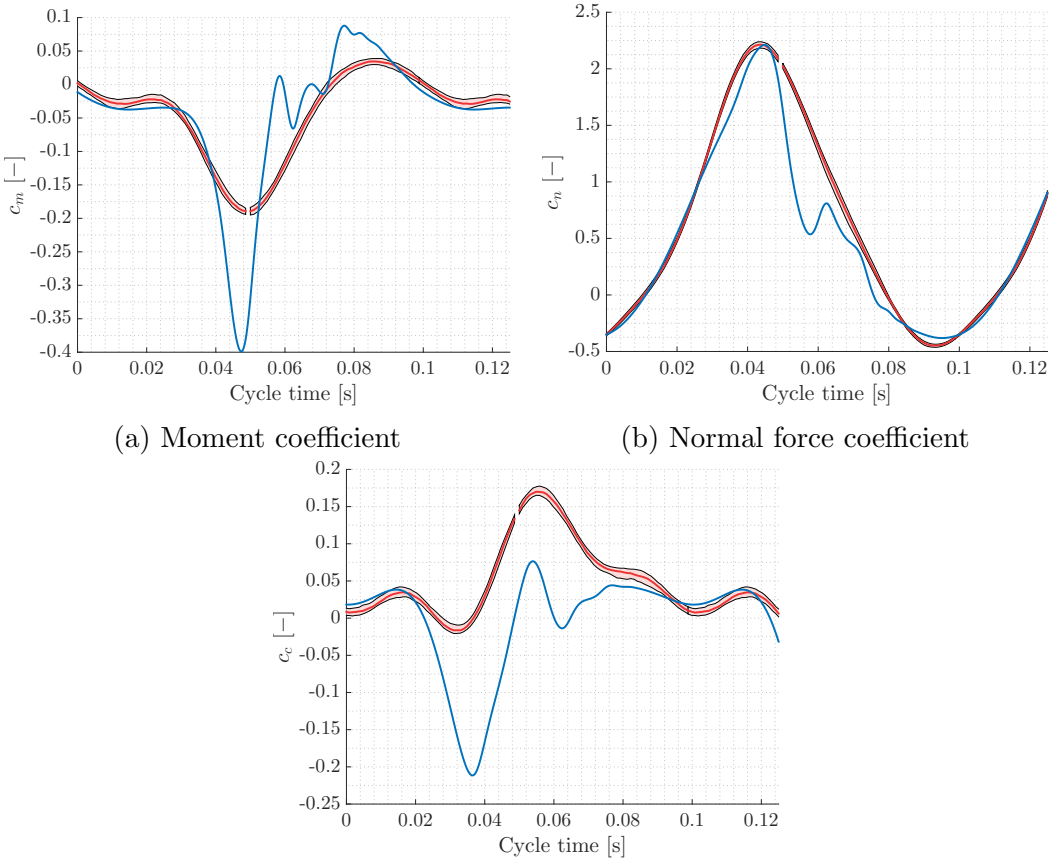

(a) Moment coefficient

(b) Normal force coefficient

(c) Chordwise force coefficient

Figure 5.9: Coefficient time evolution for the very high frequency case, compared with the experimental results

5.3.1 Vortex behaviour at higher frequencies

The most important difference at this frequency is related to the vortex behaviour. At lower frequencies, there is a counter-clockwise vortex shedding from the pressure side trailing edge, which blocks the shedding of the clockwise one. However, this is not the case at higher frequencies. An example is shown in Figure 5.11, which overlays the velocity vectors over the pressure coefficient contours, at a specific time instance.

It is possible to distinguish three main structures, all of them rotating clockwise and over the suction side. They are labeled A, B and C. The first one, vortex A, appears over the half-chord, approximately. It will merge into vortex B, which appears over the trailing edge. Both of them have low pressure regions associated, though they appear very faint. Finally, an already shed vortex, vortex C, can be seen close to the right edge of the graph.

There are two other vortices, rotating counter-clockwise. They are labeled a and b. Vortex b is already shed. It appears as an enormous change in the flow direction close

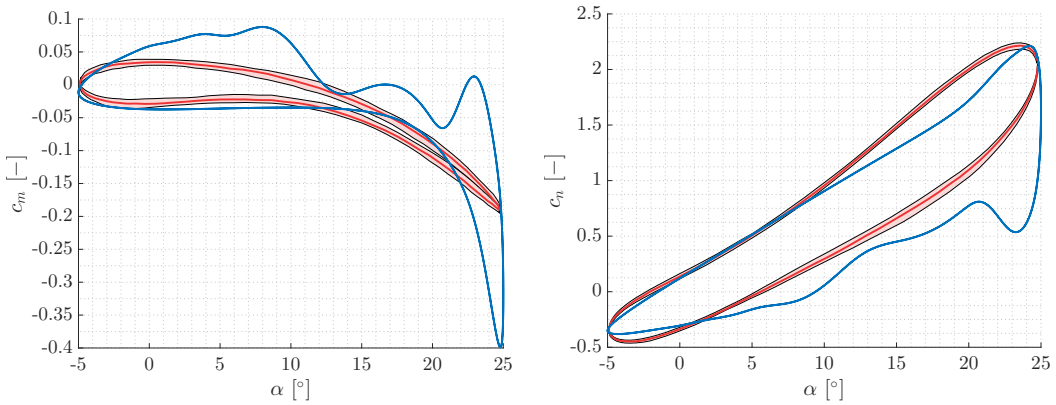

(a) Moment coefficient

(b) Normal force coefficient

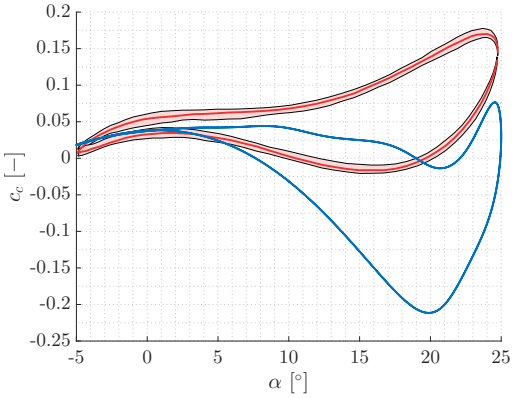

(c) Chordwise force coefficient

Figure 5.10: Coefficient angle of attack evolution for the high frequency case, compared with the experimental results

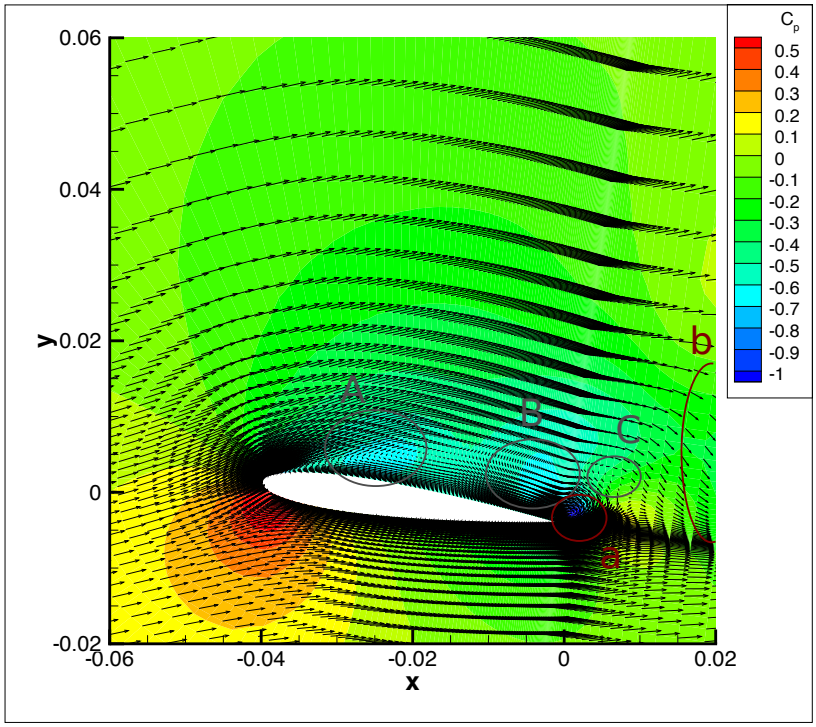

Figure 5.11: C_p in the near-field, with velocity vectors overlaid, $\alpha = 8°$, downstroke, showing the location of the vortices

to the right edge of the figure. The second one, vortex a, is a very low pressure region at the trailing edge, with flow turning from the pressure side to the suction side.

5.4 Separation and reattachment features

Separation and reattachment are two of the main flow features that help explain the behaviour of the flow coefficients. Therefore, it is worth looking further at their evolution and to compare it with the static model implemented by Leishman and Beddoes. This can refer to two different phenomena. The one discussed on the present section is reattachment on time, which refers to a change in the flow attachment state with time. Therefore, if at some point and time instance the flow is detached, but later in the cycle it is attached, it can be considered reattachment over time.

The other kind of reattachment, on the other hand, usually occurs as a consequence of a shift from a detached laminar boundary layer to a turbulent one. This phenomenon has been explained in more detail in Section 2.1.

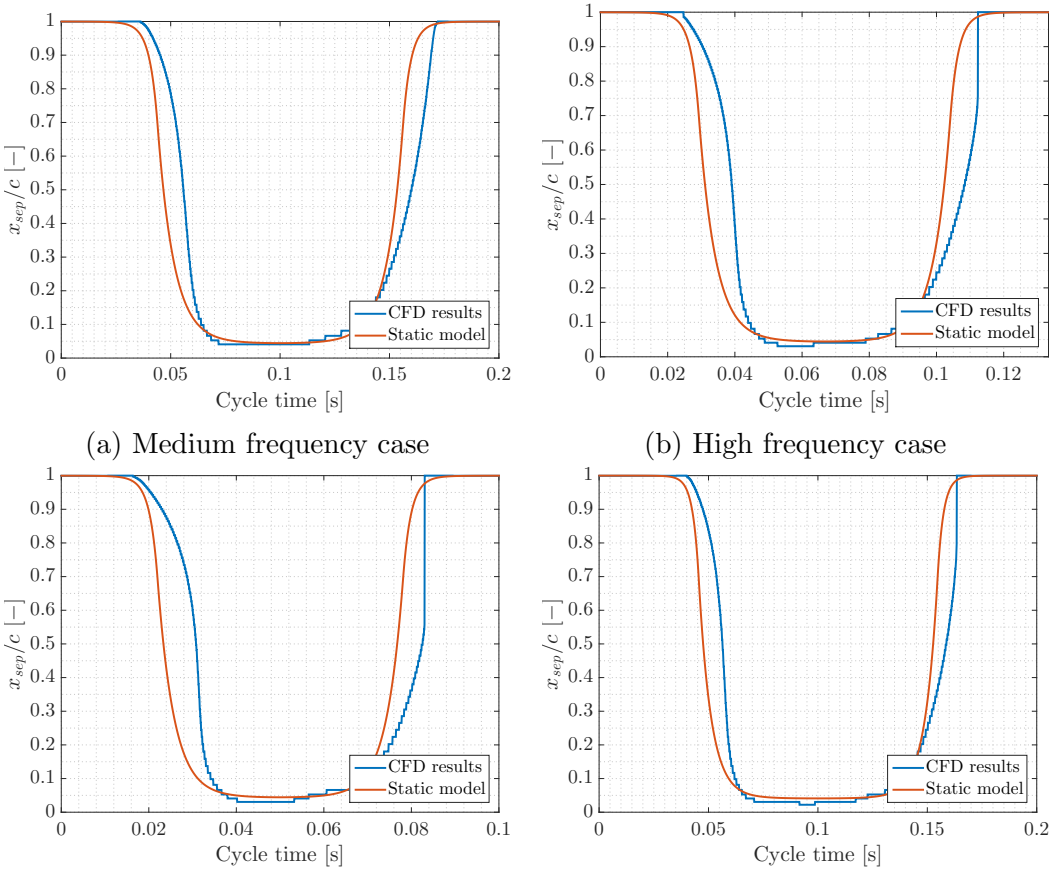

(a) Medium frequency case

(b) High frequency case

(c) Very high frequency case

(d) High amplitude case

Figure 5.12: Leishman static model and CFD results for separation for different cases

Figure 5.12 shows a comparison between the Leishman model described in Table 4.1 and the CFD separation point. This comparison is done for several different cases, at higher frequency and different amplitude from the reference one.

One interesting point is that the model alone does not tell everything about the simulation. For example, in all three cases there is a sharp, sudden increase in $f = \frac{x_{sep}}{c}$ in the downstroke phase, which would not be predicted by the model alone, even taking into account the time offset.

This phenomenon occurs because there appears to be space flow reattachment in that area. The flow detaches and downstream it reattaches, with the detached bubble reducing its size and magnitude as the angle of attack decreases, until finally disappearing. Therefore, two zeroes of the $C_f(x)$ function appear. One such case is shown in Figure 5.13, with the recirculation region contained by these two zeroes.

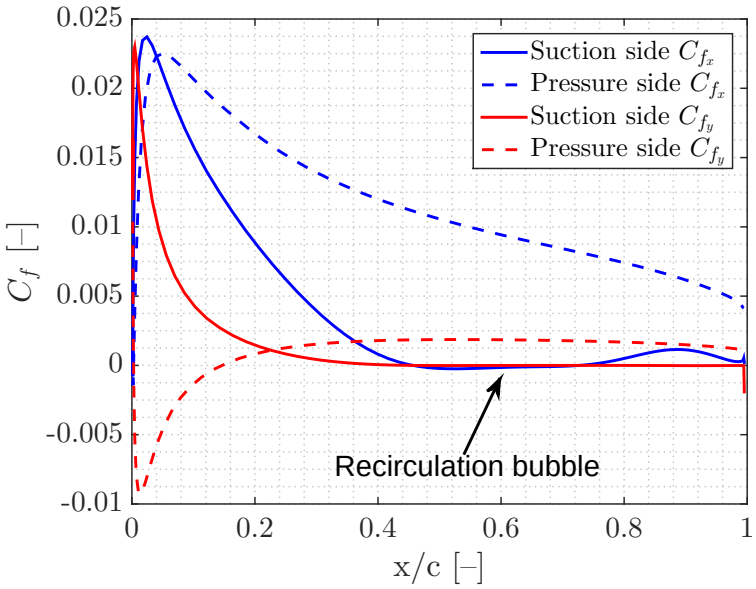

Figure 5.13: Surface friction coefficients for the very high frequency case, $\alpha = 3.7°$, downstroke

5.5 Vortex behaviour

The present section deals with the behaviour of the vortex, expanding on the results shown for the specific cases in Sections 5.1 and 5.3. First, the onset of this flow structure is described, comparing the behaviour at various conditions.

5.5.1 Vortex onset

Vortex onset is usually considered to be a consequence of the interaction between the growth of the separation region and the laminar separation bubble. This flow structure is not modelled, however, by the fully turbulent closure equations employed in the present work, nor by the transition model discussed in Section 4.3. Therefore, the vortex shows a different formation mechanism, which this section attempts to explain.

One way of achieving this is by showing the pressure coefficient 2D distribution, with the velocity vectors superimposed. A vortex appears when there is an association of a low pressure region and a turning flow.

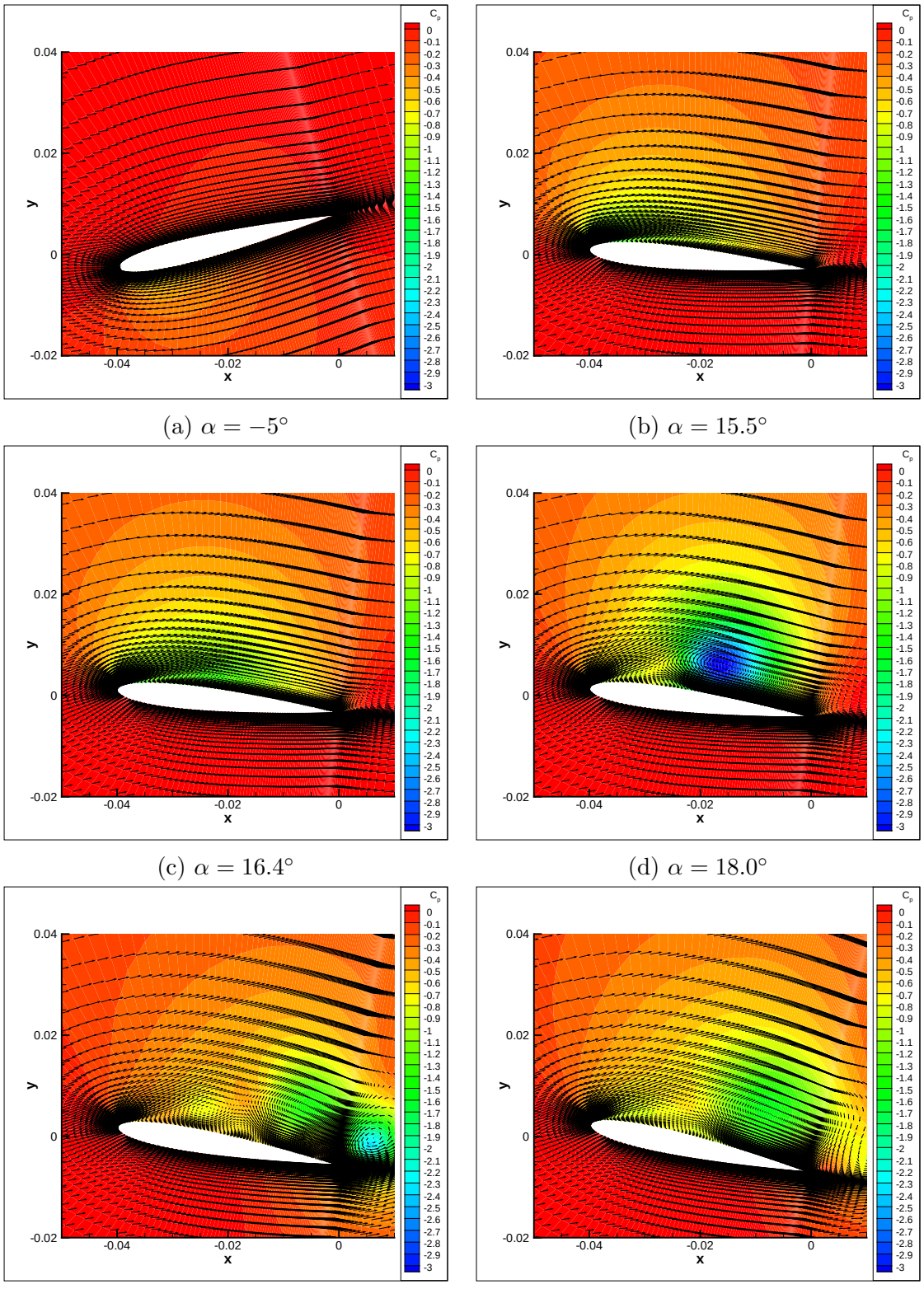

(a) $\alpha = -5°$

(b) $\alpha = 15.5°$

(c) $\alpha = 16.4°$

(d) $\alpha = 18.0°$

(e) $\alpha = 20.6°$

(f) $\alpha = 23.4°$

Figure 5.14: Vortex onset and early evolution for the reference case

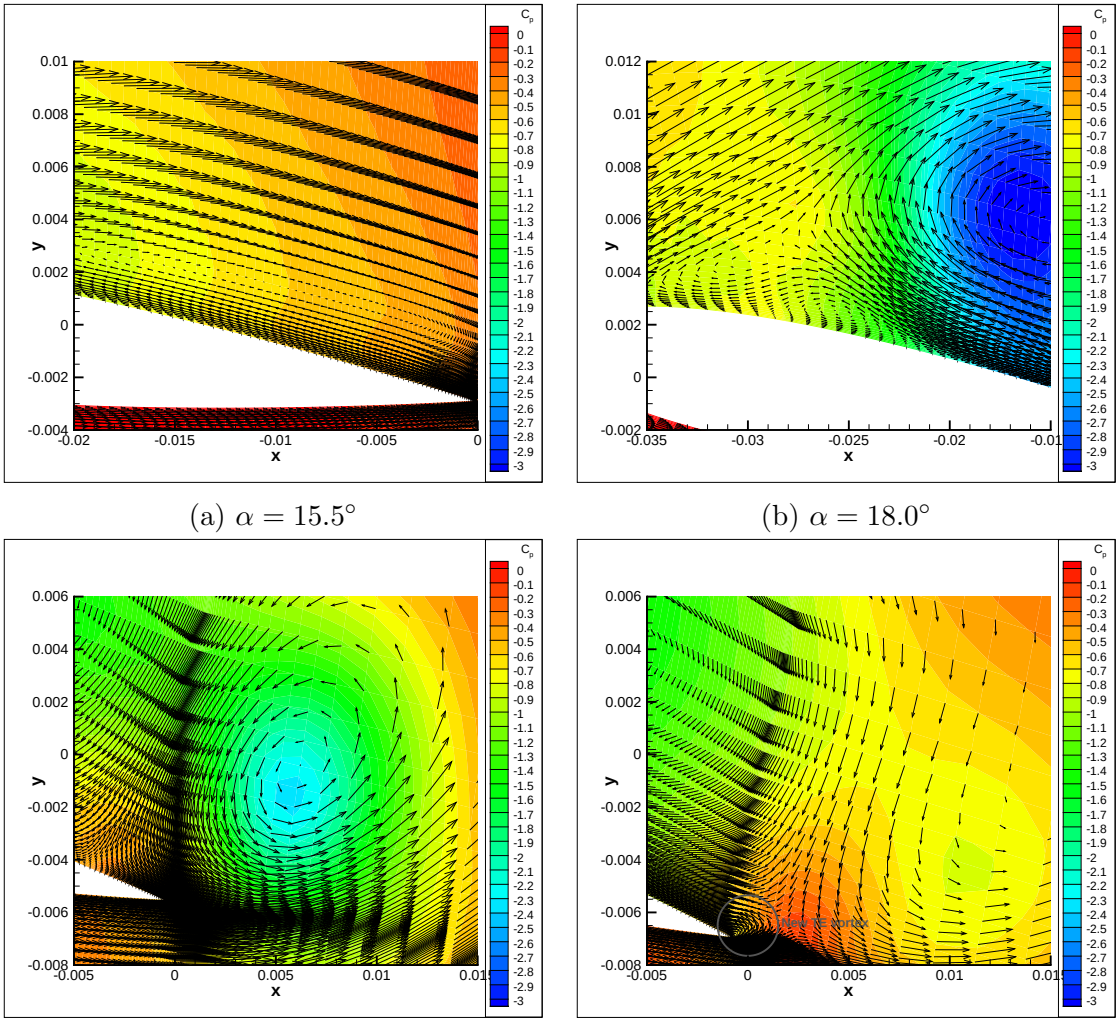

(a) $\alpha = 15.5°$ (b) $\alpha = 18.0°$

(c) $\alpha = 20.6°$ (d) $\alpha = 23.4°$

Figure 5.15: Zoom-in vortex onset and early evolution for the reference case

Figure 5.14 includes the pressure coefficient distribution in the near field, with the velocity vectors superimposed. The first plot, Figure 5.14a, shows the flow contours at the minimum angle of attack, with fully attached flow.

The second plot, chosen to be at an angle before vortex onset, but still showing substantial separation, appears in Figure 5.14b. A zoom-in of the recirculation bubble is presented in Figure 5.15a. These flow conditions are typical before vortex onset: a recirculation bubble is growing, moving upstream and stalling a larger part of the airfoil. At some point it reaches the suction peak, located in the leading edge. Then, the bubble closes and a low pressure region appears, leading to vortex onset. This is shown in Figure 5.14c. It should be noted, though, that the vortex becomes visible around mid-chord for this specific case, which contrasts with the usually established mechanism of leading edge vortex formation.

The following plot, at $\alpha = 18.0°$, in Figure 5.14d, shows the fully developed vortex, which has started to move downstream. Two more flow features, which have already been discussed, start to appear. The first one is a counter-recirculation bubble, close

to the half-chord, somewhat upstream. It appears close to the airfoil surface in Figure 5.15b. Furthermore, a third vortex is generated close to the leading edge. Since vortex onset happens at mid-chord, part of the recirculation bubble shown in Figure 5.15a is upstream the main vortex (equivalent to B in Figure 5.11) and it turns into another vortex (equivalent to A). This one ends up also moving downstream.

A counter-clockwise vortex is generated at the trailing edge, similar to the starting vortex.This vortex will continue to strengthen as the angle of attack increases and at some point it will be shed. Compare Figures 5.14e and 5.14f at that effect. A zoom-in for the first one, in Figure 5.15c, shows that the trailing edge vortex started shedding.

At the first time instance, the first vortex, B, has stabilised its position just over the trailing edge and the second one starts moving downstream, to merge with it. This leads to a slight upstream movement of the flow feature. At the end, it just dissipates as the flow starts to reattach in the downstroke phase. However, both vortex generation mechanisms continue producing vortices, since there is enough time. One example is shown in Figure 5.15d, which shows a shed trailing edge vortex and a newly appearing one.

The very high frequency case shows a similar behaviour, though with some caveats. The equivalent map, with the same scale and legend, is shown in Figure 5.16. The times are much shorter, due to the higher frequency. As in the previous case, Figure 5.16a shows fully attached flow, while Figure 5.16b shows a large recirculation region, with reversed flow, in the downstream half of the airfoil. It is shown more clearly in Figure 5.17a.

The first indication of a vortex appearing is shown in Figure 5.16c. Unlike the previous case, the bubble closes near the leading edge, creating a low pressure region. The rest of the airfoil shows little difference from the recirculation-without-vortex situation. Figure 5.16d shows a much strengthened vortex and the first evidence of two other important flow structures. Another leading-edge vortex is starting to appear around the same position as the first one. Furthermore, the aforementioned re-recirculation bubble is shown in the first quarter-chord. There is still no trailing-edge vortex.

Figure 5.16e shows the evolution of these structures. Specifically, the first vortex has moved downstream, while the second one remains close to the leading edge and the counter-rotating vortex is starting to form, termed as b in Figure 5.16f. Finally, Figure 5.16f shows the fully-formed extra vortices, termed A and b, and an incipient trailing edge one, named a. Figure 5.17b shows the zoomed-in trailing edge, with the main vortex, B, and the trailing edge one, a.

The low frequency, low amplitude calculation gives different results. An equivalent map is shown in Figure 5.18, starting from the minimum angle of attack reached ($\alpha = 5°$). Note that the C_p legend is different, since the structures are weaker. At that

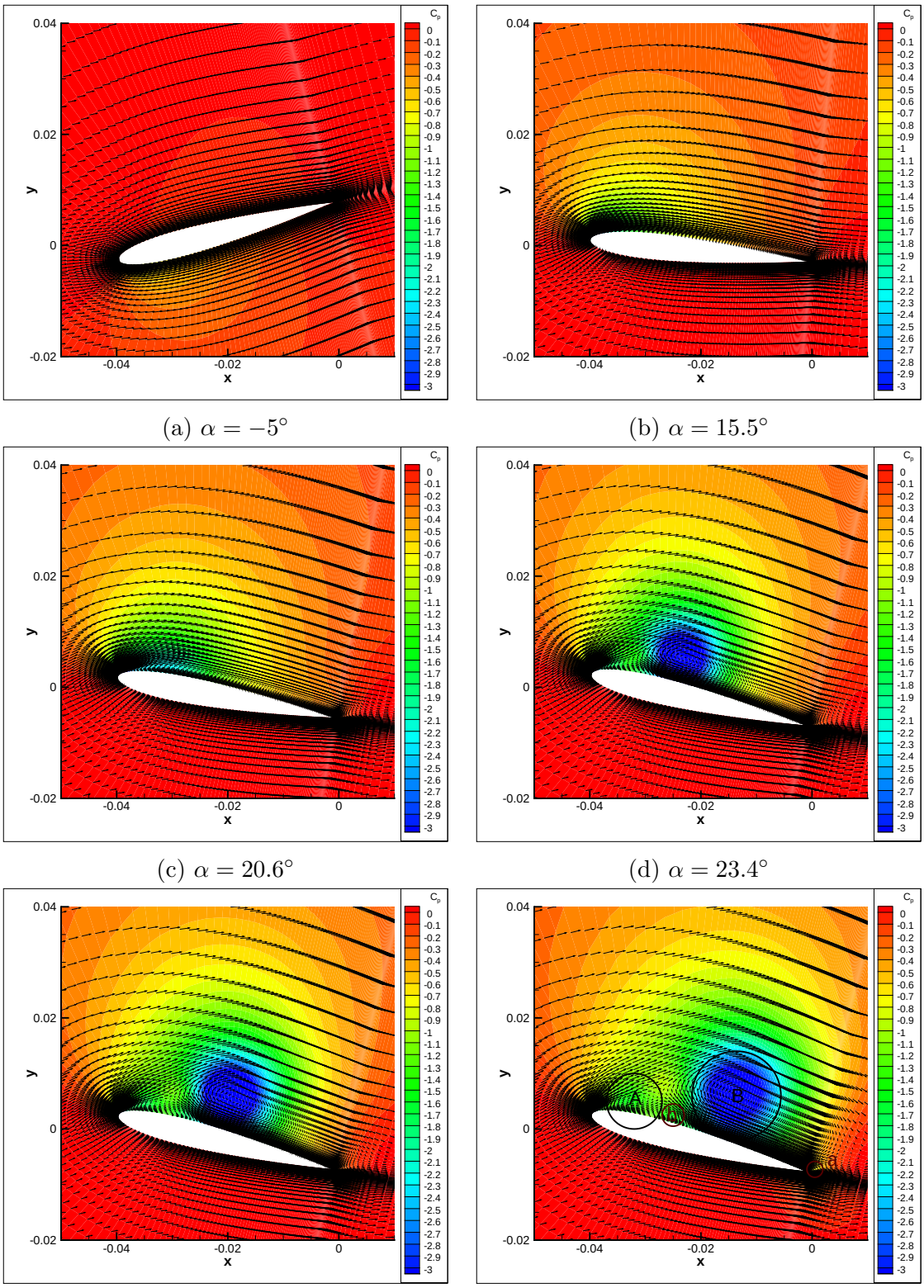

(a) $\alpha = -5°$

(b) $\alpha = 15.5°$

(c) $\alpha = 20.6°$

(d) $\alpha = 23.4°$

(e) $\alpha = 24.1°$

(f) $\alpha = 24.8°$

Figure 5.16: Vortex onset for the very high frequency case

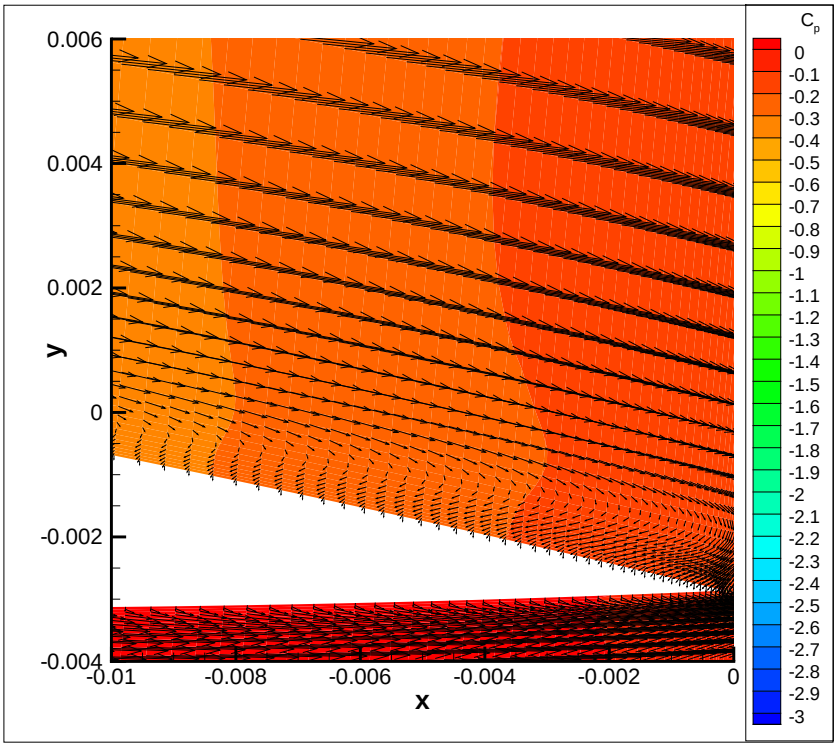

(a) $\alpha = 15.5°$

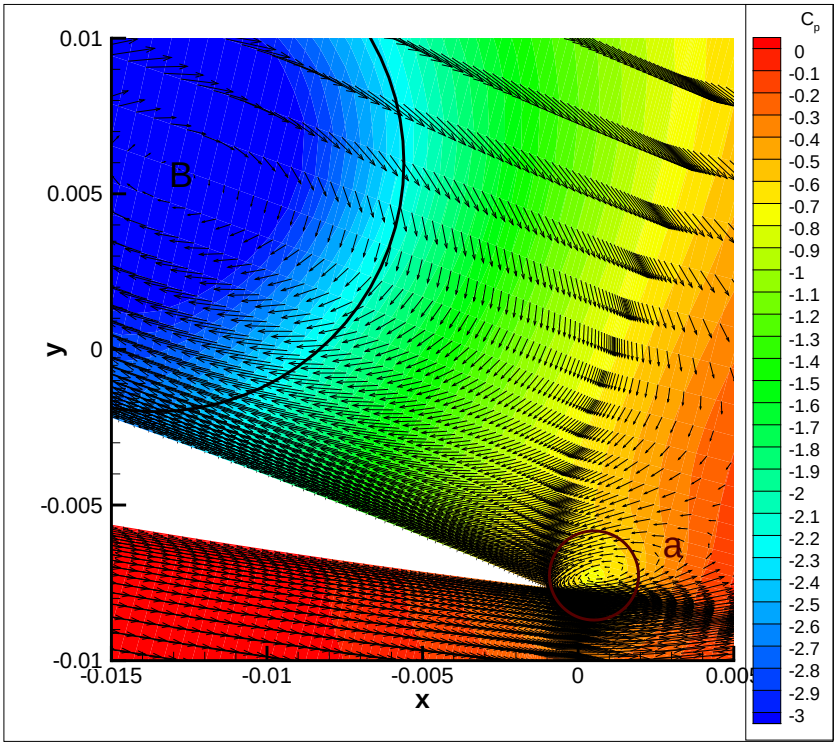

(b) $\alpha = 24.8°$

Figure 5.17: Zoom-in in two time instances for the very high frequency case

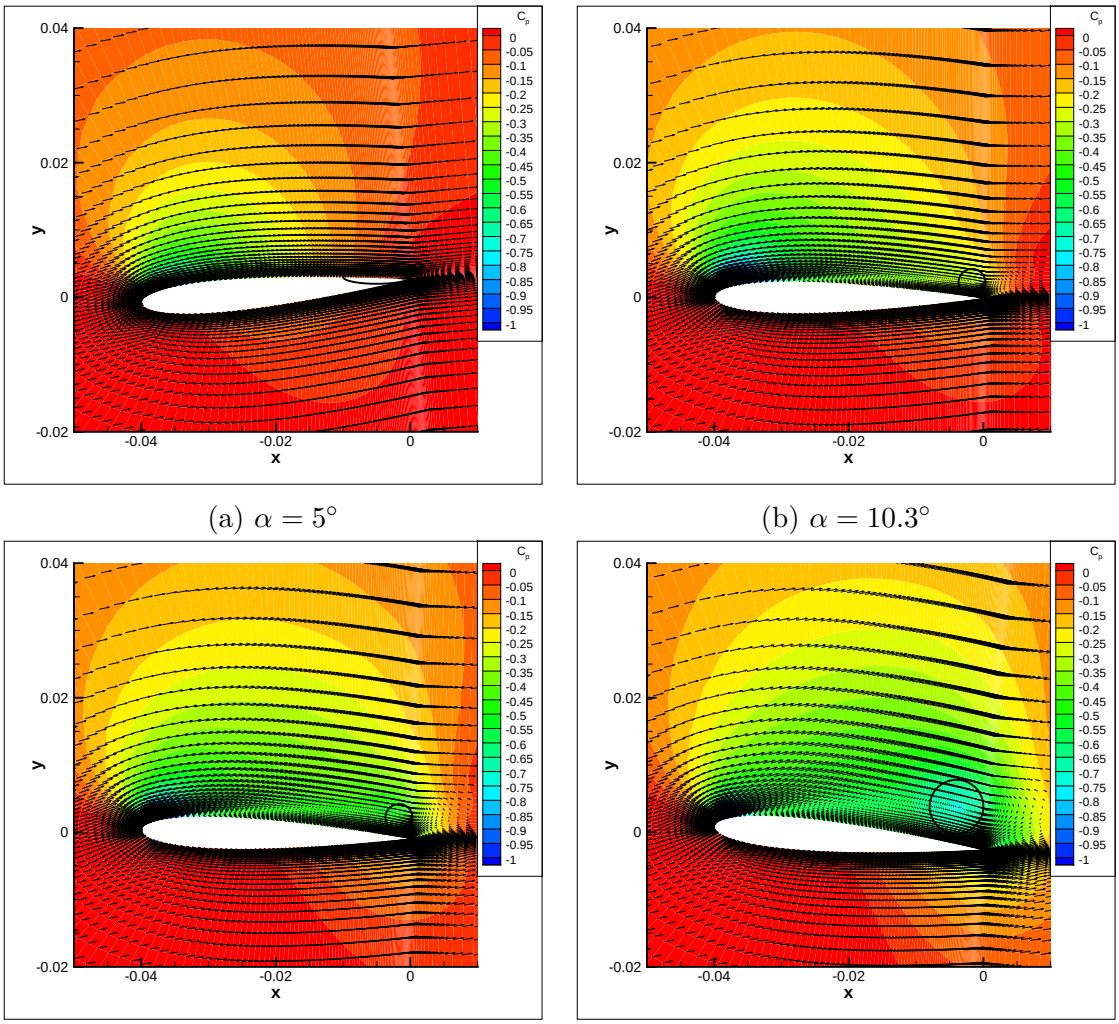

(a) $\alpha = 5°$ (b) $\alpha = 10.3°$

(c) $\alpha = 11.8°$ (d) $\alpha = 15.0°$

Figure 5.18: Vortex onset for the low frequency case

time instance, shown in Figure 5.18a, the flow is mostly attached, though a recirculation bubble appears close to the trailing edge, circled.

Figure 5.18b shows the onset of two different flow structures. First of all, the pressure remains approximately constant along the chord, slightly decreasing at the very end of the airfoil, leading to the appearance of a vortex. Secondly, at the very trailing edge, the counter-clockwise rotating vortex is forming, associated to another low pressure region. Both features are strengthened as the angle of attack increases, but they barely move, as can be seen in Figure 5.18c. This figure also shows a differentiated vortex, with an obvious local minimum.

Finally, at the maximum angle of attack, the vortex has increased its strength, in Figure 5.18d. This is related to the post-stall increase in normal force previously explained and displayed in Figure 5.8b.

Vortex onset times can be estimated by finding the first time instance for which a second peak appears in the surface C_p plot, downstream of the leading edge suction

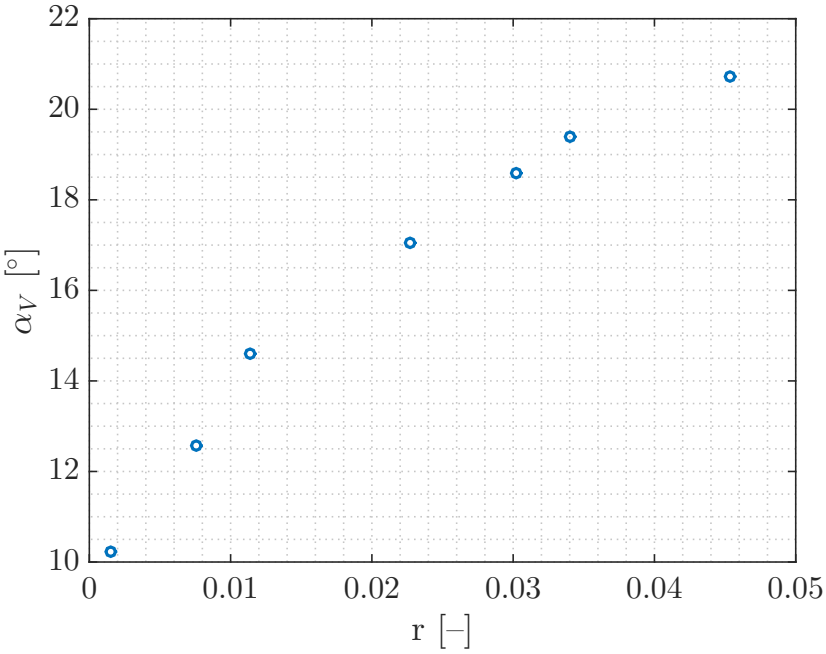

Figure 5.19: Vortex onset angle as a function of the reduced pitch rate

one. This analysis is performed as explained in Section 3.2.1, using the surface pressure coefficient distribution. That method allows for an earlier detection of the vortex, being more closely related to its onset. In this case, two variables are studied: the angle of attack at which the vortex can be said to start forming and the chordwise location of the vortex at this angle. Figure 5.19 shows this angle, which generally increases with reduced pitch rate.

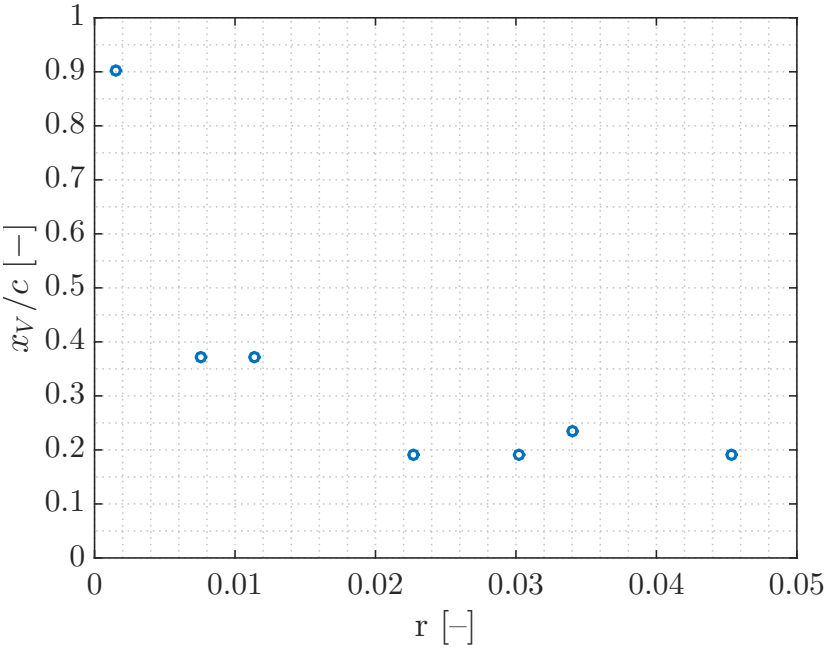

Figure 5.20: Vortex onset chordwise position as a function of the reduced pitching rate

Figure 5.20 includes the non-dimensional vortex onset location, with 0 being the leading edge and 1 being the trailing edge. It can be seen that they tend to appear

closer to the leading edge as the reduced amplitude increases, even though the onset angle is larger.

5.5.2 Vortex shedding

Vortex shedding occurs as a consequence of the periodic movement of the airfoil. The present section describes this behaviour as observed in the CFD simulations.

As commented earlier, there are three main vortices, depending on their generation point. The most useful for dynamic stall is the equivalent of the leading edge vortex, which appears on the suction side at high angles of attack. Its rotation direction is nose-up, clockwise. The second one, trailing edge vortex, appears at that point, rotating nose-down, counter-clockwise. Its topology is similar to the starting vortex. Finally, a third vortex may appear between two leading edge vortices, rotating counter-clockwise.

The trailing edge vortex is seen to detach in every case, after which another one appears. The shedding frequency is considerably higher than the oscillation frequency, conflicting with some assumptions usually applied in potential flow simulations.

The suction side vortices show a different evolution. Once the first one reaches the trailing edge, its velocity collapses. Other vortices merge into it, moving its position and increasing temporarily its strength, until the vortex dissipates.

5.6 Dynamic parameter estimation

The parameters required for running the Leishman-Beddoes model can be obtained by post-processing the simulation results. Some of them are obtained from static experiments and so have been commented previously.

5.6.1 Non-dimensional time parameters

One such set is related to the non-dimensional time it takes for various flow features to appear and to affect the coefficients. Therefore, they characterise the time evolution of the oscillating airfoil. A short description is included in Section 2.2.4.3.

5.6.1.1 Separation delay time

The separation delay time is a parameter that, as it name implies, delays the dynamic separation compared to the static one. It can be measured directly in a plot, such as Figure 5.6 or Figure 5.12 . It is obtained by measuring the difference between the times at which the model crosses the $f = 0.7$ value and the time at which the same thing happens in CFD. This procedure is summarised in Figure 5.21, showing both the static model results and the CFD data for the separation point. It is checked both in the upstroke and the downstroke phases, in order to provide an estimate of the spread.

Case	r [–]	α_{sep} [°]	α_{re} [°]
Low amplitude	0.0076	8.04	5.78
Reference	0.0113	9.48	4.70
Medium frequency	0.0227	11.13	3.11
High amplitude	0.0303	12.32	2.35
High frequency	0.0340	12.33	2.05
Very high frequency	0.0454	13.55	2.76

Table 5.1: Value of the separation and reattachment angles for the studied cases

Then, after obtaining the non-dimensional time $T_a = t_a \cdot \frac{U_\infty}{b}$, the results are shown in Table 5.2. The table shows also the differences between the up and downstroke results, which are relatively small, ±15% at most, which is lower than the usual experimental uncertainties. However, the value of the parameter for downstroke is consistently lower than for upstroke cases. The downstroke time is related to the T_r parameter introduced by Sheng [2].

Case	r [–]	t_a [ms]	T_a [–]
Low amplitude	0.0076	9.6 ± 2.7	3.5 ± 1.0
Reference	0.0113	10.4 ± 0.2	3.77 ± 0.08
Medium frequency	0.0227	8.8 ± 0.2	3.19 ± 0.08
High amplitude	0.0303	8.1 ± 0.2	2.94 ± 0.08
High frequency	0.0340	7.2 ± 0.2	2.62 ± 0.07
Very high frequency	0.0454	5.9 ± 1.0	2.14 ± 0.36

Table 5.2: Value of the T_a parameter for the studied cases

These results are close to the ones reported by Boutet et al. They report that for low reduced pitch ratio values $T_a \simeq 5.2$, while for high values $T_a = 2.43$, compared to 2.14 in the CFD simulations for the very high frequency case or to 3.19 in the medium frequency one [6].

5.6.1.2 Vortex shedding time

This parameter refers to the time it takes for a vortex to clear the trailing edge, after being formed, by travelling downstream to the trailing edge. It is calculated as the ratio between the chord and the initial velocity of the vortex core after its first detection. It is averaged in order to reduce the noise. The results are shown in Table 5.3, comparing the vortex core speed in the x direction, the calculated vortex shedding time and the non-dimensional T_{v_l}.

It is worth noting that the times show a strong dependence on the value of r. In fact, T_{v_l} is approximately inversely proportional to r. This is in line with the values reported by the experiments [7], though CFD appears to overestimate them. A comparison of this parameter is shown in Figure 5.22, which presents the experimental results and

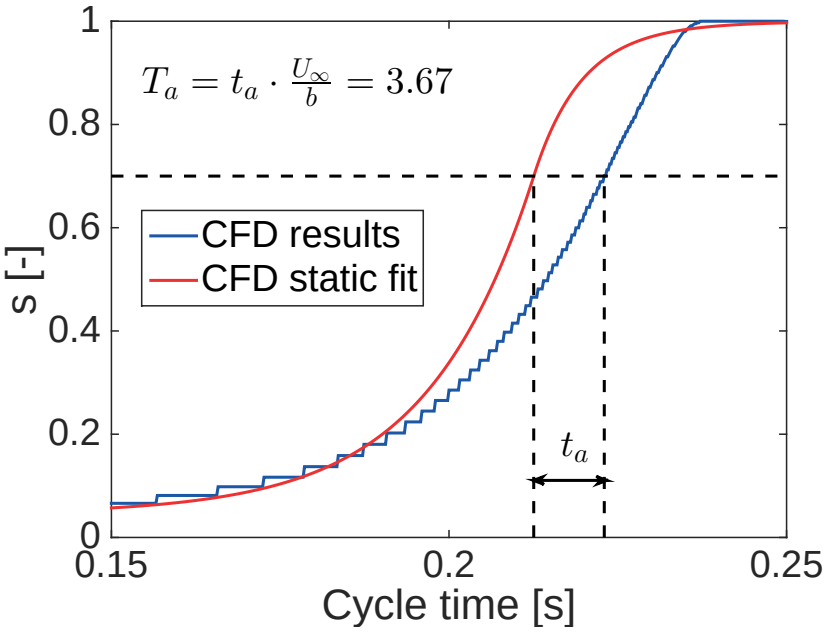

Figure 5.21: Reference case T_a calculation

Case	r [–]	$\bar{U_v}$ [$\frac{\text{m}}{\text{s}}$]	t_{v_l} [ms]	T_{v_l} [–]	Experimental T_{v_l} [–]
Low amplitude	0.0076	0.60	66.7	24.17	9.23
Reference	0.0113	0.59	68.1	24.68	8.20
Medium frequency	0.0227	1.35	29.6	10.74	5.13
High amplitude	0.0303	1.48	27.1	9.83	4.79
High frequency	0.0340	1.75	22.9	8.29	5.13
Very high frequency	0.0454	1.95	20.5	7.44	3.76

Table 5.3: Value of the T_{v_l} parameter for the studied cases

tendencies compared to the CFD value. The overestimation in the simulations is quite clear.

5.7 Stall onset criteria

As explained in Section 2.2.5, there are several different dynamic stall criteria that can be applied to the current case. The present section compares the times and angles in which they occur in the CFD results, with the experimental data and comments the overall trends. Most of these criteria have been described by Sheng et al. [1].

5.7.1 Δc_m criterion

This criterion has been described in Section 2.2.5.1. In the present study, low amplitude simulations resulted in a much lower collapse in moment than higher amplitude ones. Therefore, for every case it was taken to be $\Delta c_m = -0.01 \cdot \frac{\Delta\alpha}{5^\circ}$. The maximum value achieved, therefore, would be $\Delta c_m = -0.04$ for the high amplitude case and

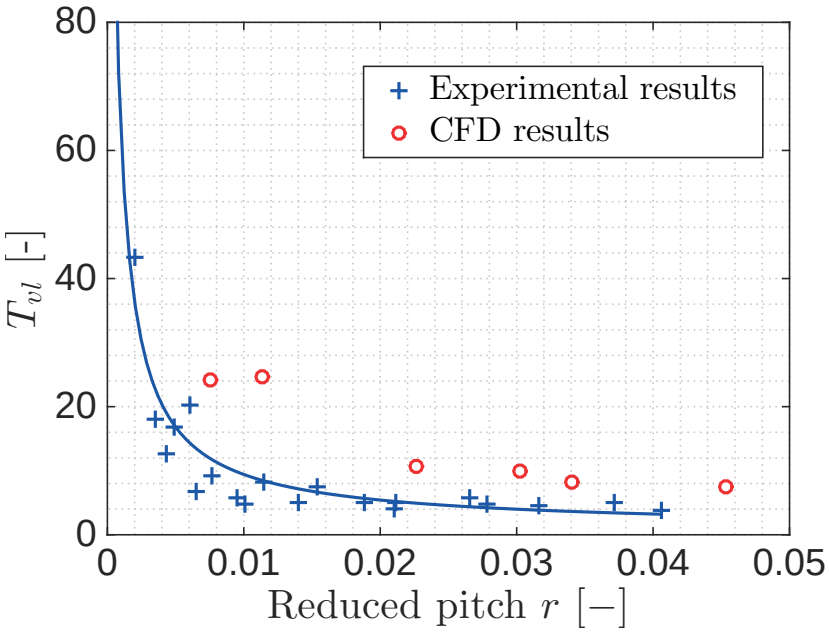

Figure 5.22: Comparison between experimental and CFD T_{v_l}, with the experimental fit overlaid [7]

the minimum is $\Delta c_m = -0.01$ for the low amplitude one. The results are shown in Table 5.4.

Case	r [–]	α_{DS} [°]	α_{DS}^{Exp} [°]	t_{DS} [ms]
Static	0	15.7	6.6	–
Low frequency	0.0015	10.09	10.61	253.0
Low amplitude	0.0076	12.38	9.25	65.8
Reference	0.0113	14.59	12.87	119.8
Medium frequency	0.0227	17.43	14.56	66.5
High amplitude	0.0303	19.58	16.63	65.9
High frequency	0.0340	19.37	16.32	47.65
Very high frequency	0.0454	21.06	15.87	38.20

Table 5.4: Value of the Δc_m criterion for the studied cases

Table 5.4 also compares the experimental values, termed α_{DS}^{Exp} [6]. It can be seen that simulations consistently overestimate this angle and they do so more importantly at higher reduced pitch ratio cases. The static case is meaningless for this criterion.

5.7.2 $\frac{\partial}{\partial\alpha}c_c$ criterion

As explained in Section 2.2.5.2, there are several minima in every case. The first one is related to the stall onset and the results are shown in Table 5.5.

The CFD values (α_{DS}) are compared to the experimental ones (α_{DS}^{Exp}). This criterion is overestimated by the CFD, due to the discrepancies between both criteria discussed previously. This is true at every point, including the static.

Case	r [–]	α_{DS} [°]	α_{DS}^{Exp} [°]	t_{DS} [ms]
Static	0	9	7	–
Low frequency	0.0015	9.58	7.47	763.5
Low amplitude	0.0076	12.06	9.13	63.5
Reference	0.0113	13.82	10.33	116.4
Medium frequency	0.0227	16.60	13.21	64.5
High amplitude	0.0303	18.35	14.86	63.7
High frequency	0.0340	18.37	12.48	45.90
Very high frequency	0.0454	19.88	15.01	36.45

Table 5.5: Value of the $\frac{\partial}{\partial\alpha}c_c$ criterion for the studied cases

The second minimum, shown in Table 5.6, is related to the second increase in normal force and the moment collapse, described earlier. Therefore, this minimum marks the point in which the vortex strengthens again.

Case	r [–]	α_V [°]	t_V [ms]
Low amplitude	0.0076	14.81	108.8
Reference	0.0113	20.23	147.8
Medium frequency	0.0227	24.44	91.3
High frequency	0.0340	24.48	72.25
High amplitude	0.0303	29.13	90.6
Very high frequency	0.0454	20.71	62.35

Table 5.6: Value of the $\frac{\partial}{\partial\alpha}c_c$ criterion for the studied cases (Second peak)

A third minimum appears before flow reattachment occurs. Therefore, this criterion can be useful for separating the flow phases.

5.7.3 $\frac{\partial^2}{\partial\alpha^2}c_n$ criterion

Section 2.2.5.3 establishes the procedure of detection. The increase in the curvature of the coefficient appears in the cases studied here as a modification in the slope due to the presence of the vortex, increasing faster just before the collapse occurs. It is accompanied by a sharp decrease in the moment coefficient, so it is correlated with the aforementioned c_m drop criterion, explained in Section 2.2.5.1.

Since this criterion depends on vortex onset, the low frequency, low amplitude case should not be taken into account. As explained in Section 5.5 this case is atypical with respect to its onset. Furthermore, as shown in Figure 5.8b the $c_n(\alpha)$ curvature in the upstroke phase is negative until stall onset has already occured.

5.7.4 $C_p|_{LE}$ and $C_p|_{c/4}$ criteria

Section 2.2.5.4 describes these two criteria, as well as the drawbacks of using them in experimental setups. Therefore, the main data analysis is performed on the leading

Case	r [–]	α_{DS} [°]	t_{DS} [ms]
Static	0	–	–
Low frequency	0.0015	11.21	289.0
Low amplitude	0.0076	10.91	55.8
Reference	0.0113	11.04	104.4
Medium frequency	0.0227	11.88	54.0
High amplitude	0.0303	12.82	54.5
High frequency	0.0340	12.81	37.33
Very high frequency	0.0454	14.50	29.85

Table 5.7: Value of the $\frac{\partial^2}{\partial \alpha^2} c_n$ criterion for the studied cases

edge pressure coefficient, which is less affected by experimental and numerical errors.

However, there are significant differences between both criteria, as shown in Figure 5.23, which plots the C_p in those two points as a function of cycle time. The described collapse does not occur, at least as strongly as it does in the other, higher Reynolds cases, as reported by Sheng et al. [1]. The decrease from the maximum is smooth, not sharp. The curvature change around the same time is also clear in the quarter-chord point.

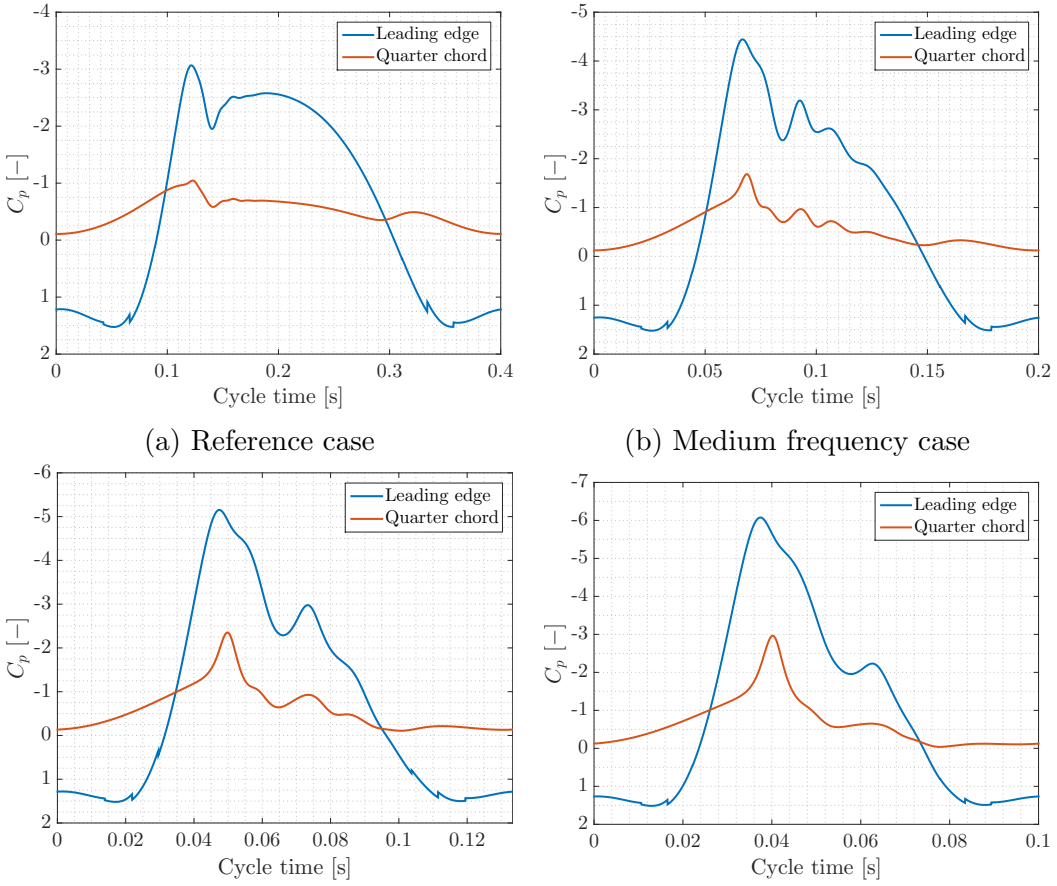

(a) Reference case

(b) Medium frequency case

(c) High frequency case

(d) Very high frequency case

Figure 5.23: Pressure coefficient time variation at leading edge and quarter chord

It was decided to assume that dynamic stall occurs when the leading edge pressure coefficient takes its minimum value. The results are shown in Table 5.8. There is a second peak, also, related to the second vortex described earlier.

Case	r [–]	α_{DS} [°]	t_{DS} [ms]
Static	0	12	–
Low amplitude	0.0076	13.03	70.7
Reference	0.0113	14.99	121.6
Medium frequency	0.0227	17.55	66.8
High amplitude	0.0303	19.30	65.4
High frequency	0.0340	19.26	47.45
Very high frequency	0.0454	20.54	37.40

Table 5.8: Value of the $C_p|_{LE}$ criterion for the studied cases

The results for the curvature of $C_p|_{c/4}$ criterion are shown in Table 5.9. There is no clear tendency from the data, which leads to not recommending applying this criterion to the experiments.

Case	r [–]	α_{DS} [°]	t_{DS} [ms]
Static	0	12	–
Low amplitude	0.0076	11.07	1.7
Reference	0.0113	13.04	13.0
Medium frequency	0.0227	12.81	6.0
High amplitude	0.0303	14.50	35.6
High frequency	0.0340	11.80	2.55
Very high frequency	0.0454	11.27	1.35

Table 5.9: Value of the $C_p|_{c/4}$ criterion for the studied cases

5.7.5 Summary

In Figure 5.24, a comparison between the previously described criteria and the 70% attached flow difference is shown. The error bars show the difference between the upstroke and downstroke phases, as stated in Table 5.2. The criterion most closely agreeing with the 70% attached flow one is the curvature change in the normal force coefficient.

The drop in c_m and the local c_c minimum are also strongly correlated to each other and could be used to estimate the parameters from experiments. The minimum C_p at the leading edge shows the same behaviour as those. There is one exception: the light stall case does not show a good point for both the c_n and the leading edge C_p criteria. The first one indicates vortex onset, instead of stall onset, which does not occur in that case. The second one also overestimates the stall onset angle. Therefore, it does not work in light stall conditions.

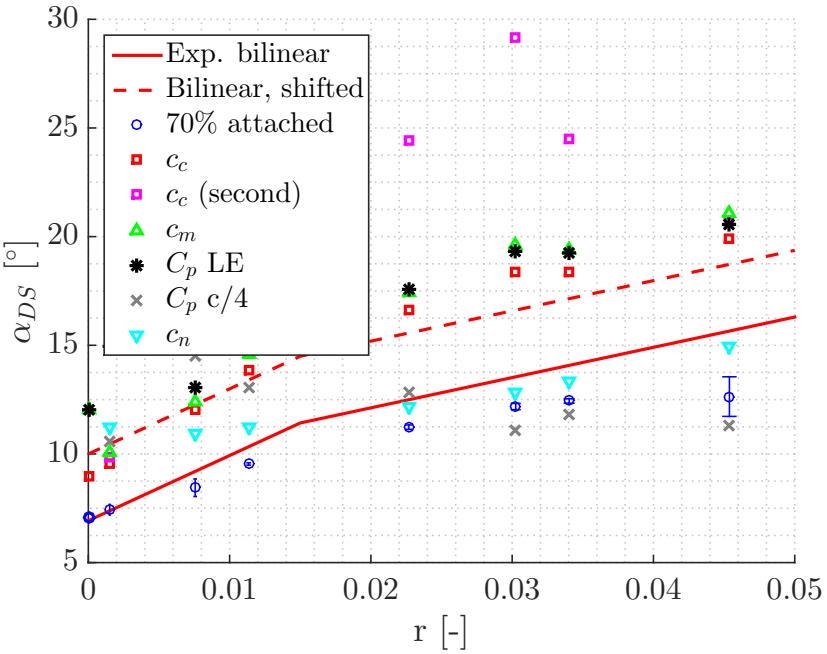

Figure 5.24: Comparison of stall onset criteria

On the other hand, the Δt between the two first minima of the chordwise force is more or less constant, unaffected by the pitching frequency. This is clearly seen on the highest frequency point, in which it goes over the maximum angle of attack. This parameter could be used as a substitute of T_{v_l}.

Figure 5.24 also shows the bilinear correlations obtained from the experiments [6]. The solid red line is the experimental one obtained from the C_M criterion. However, there is a second, shifted line to represent the offset incurred in the simulations. It is important to compare both the onset values and the slope of the curves, since this slope is employed by the model. The slopes look similar, though they are not identical. This parameter is not crucial, though.

Chapter 6

Conclusions and future work

6.1 Conclusions

The present thesis has shown the results of several 2D Unsteady RANS simulations on low-Reynolds dynamic stall, for a NACA0012 airfoil. A short description of the numerical setup is included. Convergence has been achieved in the dynamic cases, for both cycle-to-cycle and time-steps per cycle. A comparison between two vortex core detection criteria has been presented, their strengths and weaknesses have been shown.

First of all, several static cases were simulated, and compared to the experimental results. Even though the boundary layer transition mechanisms are not modelled, the normal force and pitch moment obtained are close to those measured experimentally, including at high angles of attack. Menter's SST turbulence model provides better agreement than Spalart-Allmaras, as was expected. However, the simulations predicted trailing edge stall, while the actual mechanism in the experiments was, most likely, leading edge stall.

The core of the work are the dynamic cases, which provide insights in the likely development of dynamic stall. However, since there is no modelling of boundary layer transition, the usual mechanism for dynamic stall onset cannot be simulated. Despite this, the time evolution of loads appears to be consistent between experiments and simulations.

There is a major difference in the chordwise force, though. This might be due to the uncertainties in the corrections applied in this measurement. The maxima and minima appear around the same area, which is important for the corresponding stall onset criterion.

Another important difference between experiments and CFD is the higher collapse in both the moment and normal force after stall onset in the simulations. This collapse is followed by stronger oscillations, mostly absent in experimental results.

It is possible to study the behaviour of the different vortices present in the simu-

lations. They imply that clockwise vortices are generated over the suction side after the first one appears. Furthermore, the shedding frequency of trailing edge vortices is higher than the movement frequency.

Vortex onset occurs at higher angles for an increased reduced pitch rate and vortices are generated closer to the leading edge, too. At the shallow stall extreme, the vortex appears at the trailing edge, and does not move significantly.

Some parameters for the semi-empirical models have been derived, including two non-dimensional times. The first one, the separation delay time, has been shown to decrease with r, as reported in the experiments. Another one, vortex shedding time, also decreases. This relation is approximately inversely proportional for this case.

Stall onset correlates quite well with the experimental criteria, though there are several limitations to be noted. First of all, some of them do not work in shallow stall, low reduced pitch rate cases. One example is the leading edge pressure coefficient, which overestimates the angle for stall onset in those conditions. Another important criterion, dealing with the curvature of the normal force coefficient curve, is closely related to vortex onset, instead of stall onset.

Finally, it should be noted that these results are not a perfect representation of the flow. Therefore, they should be taken as indicative of the actual flow physics.

6.2 Future work

One of the main directions for the future is a comparison including further simulations, both for other, thicker, airfoils and other cases for the present one. Within past work, there are data for a NACA0018 airfoil at the same conditions. Therefore, this airfoil would be an obvious continuation.

Another possible direction is improving the fidelity of the simulations. For example, a transition model could be implemented within SU2 in order to check whether it has a large impact on the flow, besides changing the mechanism of vortex onset. Other improvement would be simulating the full 3D field, which could help in determining the appropriate strength of the vortex, though it would be more computationally expensive. Another modification in this line could be using mixed URANS-LES frameworks. This is also more expensive.

Finally, Particle Image Velocimetry or other flow visualisation techniques would be very informative with respect to the flow physics, and also stall and vortex onset. With this information, the CFD models could be validated and the error incurred measured, without relying on empirical criteria.

Bibliography

[1] W. Sheng, R. A. M. Galbraith, and F. N. Coton. "A New Stall-Onset Criterion for Low Speed Dynamic-Stall". In: *Journal of Solar Energy Engineering* 128.4 (2006), p. 461. DOI: 10.1115/1.2346703 (cit. on pp. 1, 12, 14–16, 63, 66).

[2] W. Sheng, R. A. M. Galbraith, and F. N. Coton. "A Modified Dynamic Stall Model for Low Mach Numbers". In: *Journal of Solar Energy Engineering* 130.3 (2008), p. 031013. DOI: 10.1115/1.2931509 (cit. on pp. 1, 12, 13, 62).

[3] W. Sheng, R. A. M. Galbraith, and F. N. Coton. "Prediction of Dynamic Stall Onset for Oscillatory Low-Speed Airfoils". In: *Journal of Fluids Engineering* 130.10 (2008), p. 101204. DOI: 10.1115/1.2969450 (cit. on p. 1).

[4] K. McLaren, S. Tullis, and S. Ziada. "Computational fluid dynamics simulation of the aerodynamics of a high solidity, small-scale vertical axis wind turbine". In: *Wind Energy* 15.3 (2011), pp. 349–361. DOI: 10.1002/we.472 (cit. on p. 2).

[5] K. McLaren, S. Tullis, and S. Ziada. "Measurement of high solidity vertical axis wind turbine aerodynamic loads under high vibration response conditions". In: *Journal of Fluids and Structures* 32 (2012). The 7th International Symposium on Fluid-Structure Interactions, Flow-Sound Interactions, and Flow-Induced Vibrations & Noise, pp. 12–26. ISSN: 0889-9746. DOI: 10.1016/j.jfluidstructs.2012.01.001 (cit. on p. 2).

[6] J. Boutet, G. Dimitriadis, and X. Amandolese. "Dynamic stall onset variation with reduced frequency for three stall mechanisms". In: *Proceedings of the IFASD 2017 Conference*. 2017 (cit. on pp. 2, 14, 21, 62, 64, 68).

[7] J. Boutet, G. Dimitriadis, and X. Amandolese. "Evaluation of a Modified Leishman-Beddoes Model for Three Airfoil Sections Experiencing Dynamic Stall at Low Reynolds Number". Under preparation. 2018 (cit. on pp. 3, 62, 64).

[8] T. D. Economon, F. Palacios, S. R. Copeland, T. W. Lukaczyk, and J. J. Alonso. "SU2: An Open-Source Suite for Multiphysics Simulation and Design". In: *AIAA Journal* 54.3 (2016), pp. 828–846. DOI: 10.2514/1.j053813 (cit. on pp. 4, 21).

[9] T. D. Economon et al. "Performance optimizations for scalable implicit RANS calculations with SU2". In: *Computers & Fluids* 129 (2016), pp. 146–158. DOI: 10.1016/j.compfluid.2016.02.003 (cit. on pp. 4, 21).

[10] C. Geuzaine and J.-F. Remacle. "Gmsh: A 3-D finite element mesh generator with built-in pre- and post-processing facilities". In: *International Journal for Numerical Methods in Engineering* 79.11 (2009), pp. 1309–1331. DOI: 10.1002/nme.2579 (cit. on pp. 4, 22).

[11] G. B. McCullough and D. E. Gault. *Examples of three representative types of airfoil-section stall at low speed*. Tech. rep. NACA-TN-2502. National Advisory Committee for Aeronautics. Ames Aeronautical Lab.; Moffett Field, CA, United States, 1951 (cit. on pp. 5, 6).

[12] J. D. Anderson. *Fundamentals of aerodynamics*. Ed. by L. Bearnesderfer and E. Castellano. 2nd Edition. Aeronautical and aerospace engineering series. McGraw-Hill, 1991. ISBN: 0-07-001679-8 (cit. on pp. 5, 6).

[13] K. W. McAlister, S. L. Pucci, W. J. McCroskey, and L. W. Carr. *An Experimental Study of Dynamic Stall on Advanced Airfoil Sections. Volume 2: Pressure and Force data*. Technical Memorandum 84245. National Aeronautics and Space Administration, 1982 (cit. on pp. 6, 17).

[14] W. J. McCroskey. "Unsteady Airfoils". In: *Annual Review of Fluid Mechanics* 14.1 (1982), pp. 285–311. DOI: 10.1146/annurev.fl.14.010182.001441 (cit. on p. 8).

[15] D. Petot. "Modélisation du décrochage dynamique par équations différentielles". In: *La Recherche Aérospatiale* 5 (1989), pp. 59–72 (cit. on pp. 8, 13, 14).

[16] M. S. Chandrasekhara, M. C. Wilder, and L. W. Carr. "Competing Mechanisms of Compressible Dynamic Stall". In: *AIAA Journal* 36.3 (1998), pp. 387–393. DOI: 10.2514/2.375 (cit. on pp. 9, 45).

[17] J. G. Leishman and T. S. Beddoes. "A generalised model for airfoil unsteady aerodynamic behaviour and dynamic stall using the indicial method". In: *Proceedings of the 42nd Annual forum of the American Helicopter Society* (1986), pp. 243–265 (cit. on pp. 9, 11, 12).

[18] J. G. Leishman and T. S. Beddoes. "A Semi-Empirical Model for Dynamic Stall". In: *Journal of the American Helicopter Society* 34.3 (1989), pp. 3–17. DOI: 10.4050/jahs.34.3 (cit. on pp. 9–11).

[19] J. G. Leishman and G. L. Crouse. "State-space model for unsteady airfoil behavior and dynamic stall". In: *30th Structures, Structural Dynamics and Materials Conference*. American Institute of Aeronautics and Astronautics, 1989. DOI: 10.2514/6.1989-1319 (cit. on pp. 9, 10, 12).

[20] T. S. Beddoes. "Representation of airfoil behaviour". In: *Vertica* 7.2 (1983), pp. 183–197 (cit. on pp. 10, 11).

[21] D. G. F. Herring, A. J. Niven, and R. A. Galbraith. "Analysis of reattachment during ramp down tests". In: *Proceedings of the 14th European Rotorcraft Forum*. 11. 1988. URL: http://hdl.handle.net/20.500.11881/2782 (cit. on p. 12).

[22] C. T. Tran and D. Falchero. "Application of the ONERA dynamic stall model to a helicopter blade in forward flight". In: *Vertica* 6.3 (1982), pp. 219–239 (cit. on p. 14).

[23] R. Dat, C. T. Tran, and D. Petot. "Modèle phénoménologique de décrochage dynamique sur profil de pale d'hélicoptère". In: *16è Colloque d'aérodynamique apliquée*. 1979 (cit. on p. 14).

[24] P. R. Spalart. "Comments on the Feasibility of LES for Wings, and on Hybrid RANS/LES Approach". In: *Proceedings of First AFOSR International Conference on DNS/LES, 1997*. 1997 (cit. on p. 17).

[25] P. R. Spalart et al. "A New Version of Detached-eddy Simulation, Resistant to Ambiguous Grid Densities". In: *Theoretical and Computational Fluid Dynamics* 20.3 (2006), pp. 181–195. DOI: 10.1007/s00162-006-0015-0 (cit. on p. 17).

[26] G. Martinat, M. Braza, Y. Hoarau, and G. Harran. "Turbulence modelling of the flow past a pitching NACA0012 airfoil at 10^5 and 10^6 Reynolds numbers". In: *Journal of Fluids and Structures* 24.8 (2008), pp. 1294–1303. DOI: 10.1016/j.jfluidstructs.2008.08.002 (cit. on p. 17).

[27] S. Wang, D. B. Ingham, L. Ma, M. Pourkashanian, and Z. Tao. "Turbulence modeling of deep dynamic stall at relatively low Reynolds number". In: *Journal of Fluids and Structures* 33 (2012), pp. 191–209. DOI: 10.1016/j.jfluidstructs.2012.04.011 (cit. on p. 17).

[28] A. Zanotti, R. Nilifard, G. Gibertini, A. Guardone, and G. Quaranta. "Assessment of 2D/3D numerical modeling for deep dynamic stall experiments". In: *Journal of Fluids and Structures* 51 (2014), pp. 97–115. DOI: 10.1016/j.jfluidstructs.2014.08.004 (cit. on p. 17).

[29] S. Wang, D. B. Ingham, L. Ma, M. Pourkashanian, and Z. Tao. "Numerical investigations on dynamic stall of low Reynolds number flow around oscillating airfoils". In: *Computers & Fluids* 39.9 (2010), pp. 1529–1541. DOI: 10.1016/j.compfluid.2010.05.004 (cit. on p. 17).

[30] F. R. Menter. *Improved two-equation k-omega turbulence models for aerodynamic flows*. Tech. rep. NASA Ames Research Center, Moffett Field, CA, United States, 1992 (cit. on p. 17).

[31] F. R. Menter. "Two-equation eddy-viscosity turbulence models for engineering applications". In: *AIAA Journal* 32.8 (1994), pp. 1598–1605. DOI: 10.2514/3.12149 (cit. on p. 17).

[32] P. Spalart and S. Allmaras. "A one-equation turbulence model for aerodynamic flows". In: *30th Aerospace Sciences Meeting and Exhibit*. American Institute of Aeronautics and Astronautics, 1992. DOI: 10.2514/6.1992-439 (cit. on p. 17).

[33] S. C. Cakmakcioglu, O. Bas, and U. Kaynak. "A correlation-based algebraic transition model". In: *Proceedings of the Institution of Mechanical Engineers, Part C: Journal of Mechanical Engineering Science* (2017), p. 095440621774353. DOI: 10.1177/0954406217743537 (cit. on p. 17).

[34] F. R. Menter, R. Langtry, and S. Völker. "Transition Modelling for General Purpose CFD Codes". In: *Flow, Turbulence and Combustion* 77.1-4 (2006), pp. 277–303. DOI: 10.1007/s10494-006-9047-1 (cit. on p. 17).

[35] R. B. Langtry and F. R. Menter. "Correlation-Based Transition Modeling for Unstructured Parallelized Computational Fluid Dynamics Codes". In: *AIAA Journal* 47.12 (2009), pp. 2894–2906. DOI: 10.2514/1.42362 (cit. on p. 17).

[36] L. W. Carr and M. S. Chandrasekhara. "Compressibility effects on dynamic stall". In: *Progress in Aerospace Sciences* 32.6 (1996), pp. 523–573. DOI: 10.1016/0376-0421(95)00009-7 (cit. on p. 17).

[37] T. Albring. *Bug about the wrong pitching_omega of incompressible flow*. Online. 2015. URL: https://github.com/su2code/SU2/issues/193 (cit. on p. 18).

[38] L. Graftieaux, M. Michard, and N. Grosjean. "Combining PIV, POD and vortex identification algorithms for the study of unsteady turbulent swirling flows". In: *Measurement Science and Technology* 12.9 (2001), pp. 1422–1429. DOI: 10.1088/0957-0233/12/9/307 (cit. on pp. 18, 19).

[39] M. Michard and T. Favelier. "Développement d'un critère d'identification de structures tourbillonnaires adapté aux mesures de vitesse par PIV". In: *9e Congrès Francophone de Vélocimétrie Laser*. 2004 (cit. on pp. 18, 19).

[40] J. Sahner, T. Weinkauf, and H.-C. Hege. "Galilean Invariant Extraction and Iconic Representation of Vortex Core Lines". eng. In: *EUROVIS 2005: Eurographics / IEEE VGTC Symposium on Visualization*. The Eurographics Association, 2005. DOI: 10.2312/vissym/eurovis05/151-160 (cit. on pp. 18, 19).

[41] V. Kolář. "Vortex identification: New requirements and limitations". In: *International Journal of Heat and Fluid Flow* 28.4 (2007), pp. 638–652. DOI: 10.1016/j.ijheatfluidflow.2007.03.004 (cit. on pp. 18, 19).

[42] J. C. R. Hunt, A. A. Wray, and P. Moin. "Eddies, Streams, and Convergence Zones in Turbulent Flows". In: *Proceedings of the Summer Program 1988*. Ed. by C. for Turbulence Research. 1988, pp. 193–208 (cit. on p. 18).

[43] J. Jeong and F. Hussain. "On the identification of a vortex". In: *Journal of Fluid Mechanics* 285.-1 (1995), p. 69. DOI: 10.1017/s0022112095000462 (cit. on pp. 18, 19).

[44] M. S. Chong, A. E. Perry, and B. J. Cantwell. "A general classification of three-dimensional flow fields". In: *Physics of Fluids A: Fluid Dynamics* 2.5 (1990), pp. 765–777. DOI: 10.1063/1.857730 (cit. on p. 19).

[45] H. Güner. "Delayed detached-eddy simulations for separated flows". MA thesis. Faculté des Sciences appliquées, Université de Liège, 2015 (cit. on p. 23).

[46] R. Gómez Gómez. "Fluid-structure interaction simulations of separated flows through Detached Eddy Simulations". MA thesis. Faculté des Sciences appliquées, Université de Liège, 2017 (cit. on p. 23).

[47] A. Zanotti, F. Auteri, G. Campanardi, and G. Gibertini. "An Experimental Set Up for the Study of the Retreating Blade Dynamic Stall". In: *Proceedings of the 37th European Rotorcraft Forum*. 145. 2011 (cit. on p. 26).

Appendix A

Load coefficients for studied cases

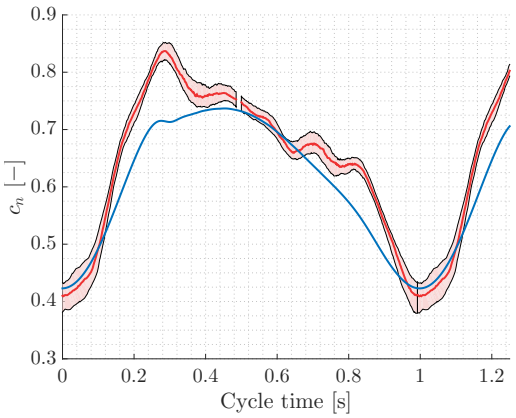

(a) Low frequency

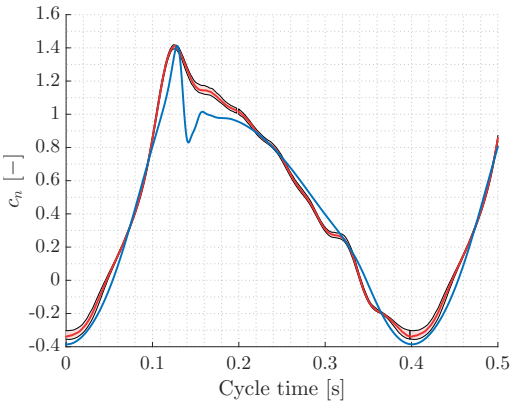

(b) Reference

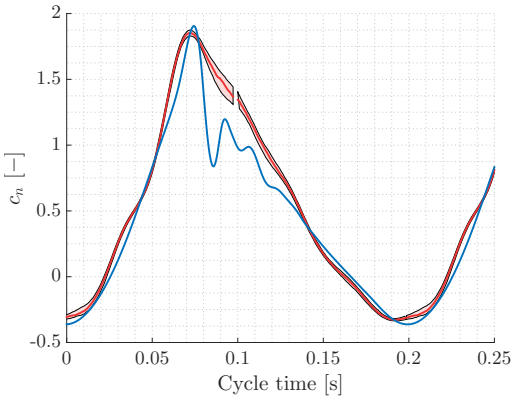

(c) Medium frequency

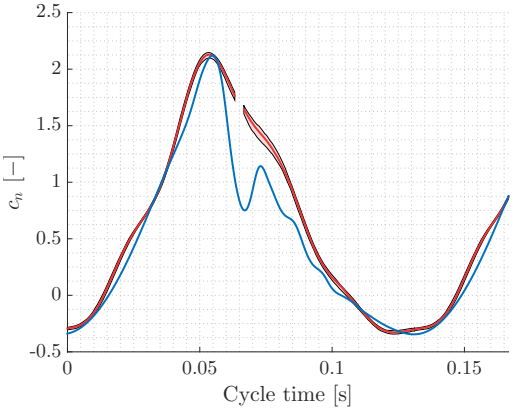

(d) High frequency

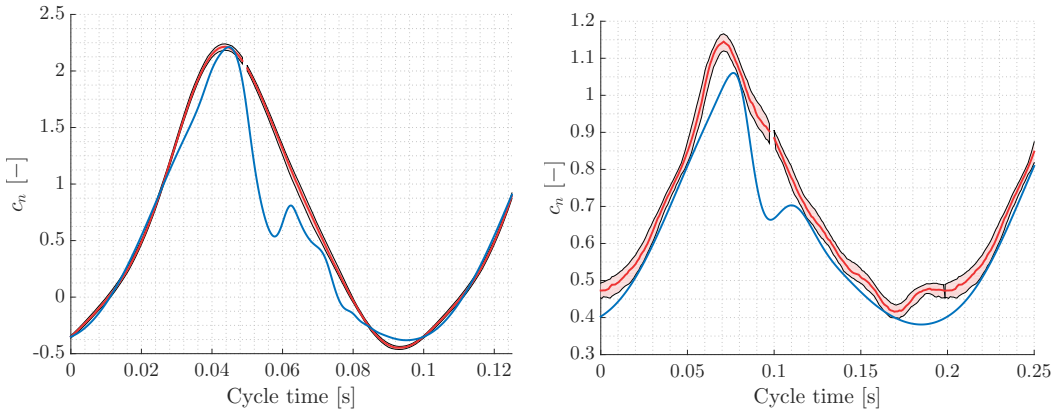

(e) Very high frequency

(f) Low amplitude

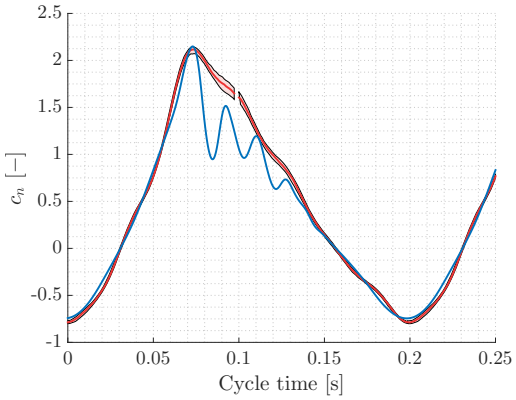

(g) High amplitude

Figure A.1: Normal force coefficient time evolution for studied cases

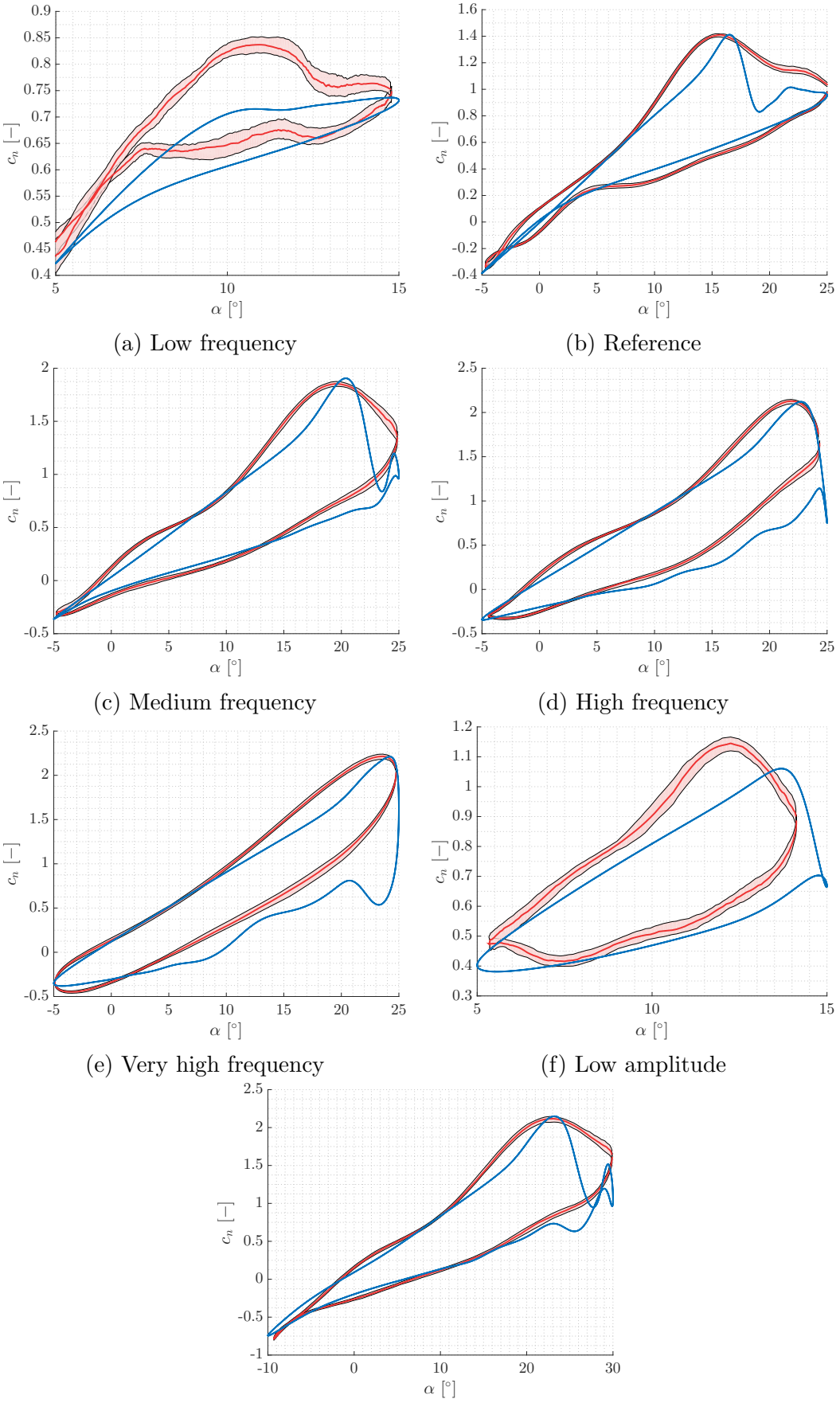

(a) Low frequency

(b) Reference

(c) Medium frequency

(d) High frequency

(e) Very high frequency

(f) Low amplitude

(g) High amplitude

Figure A.2: Normal force coefficient angle of attack evolution for studied cases

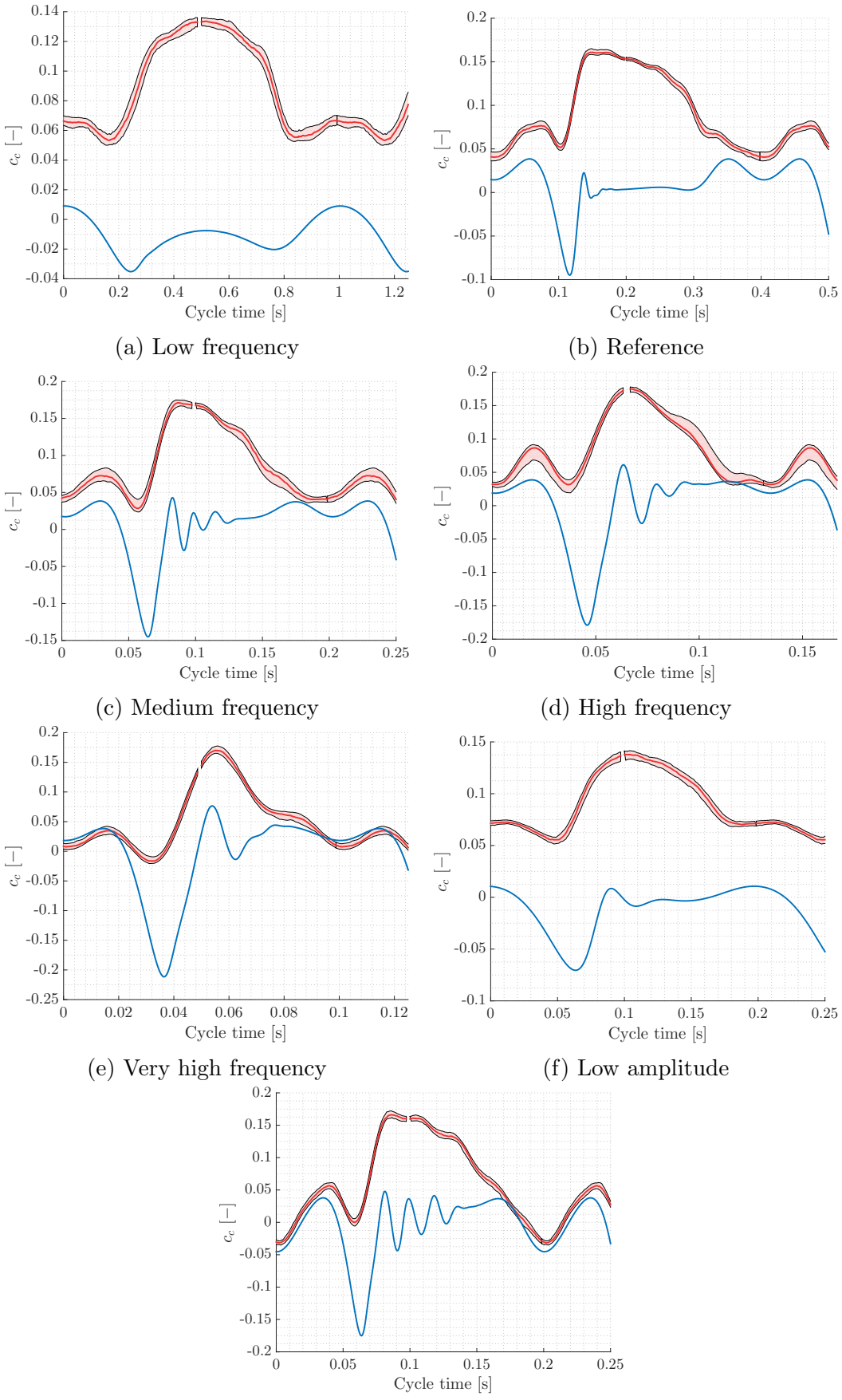

(a) Low frequency

(b) Reference

(c) Medium frequency

(d) High frequency

(e) Very high frequency

(f) Low amplitude

(g) High amplitude

Figure A.3: Chordwise force coefficient time evolution for studied cases

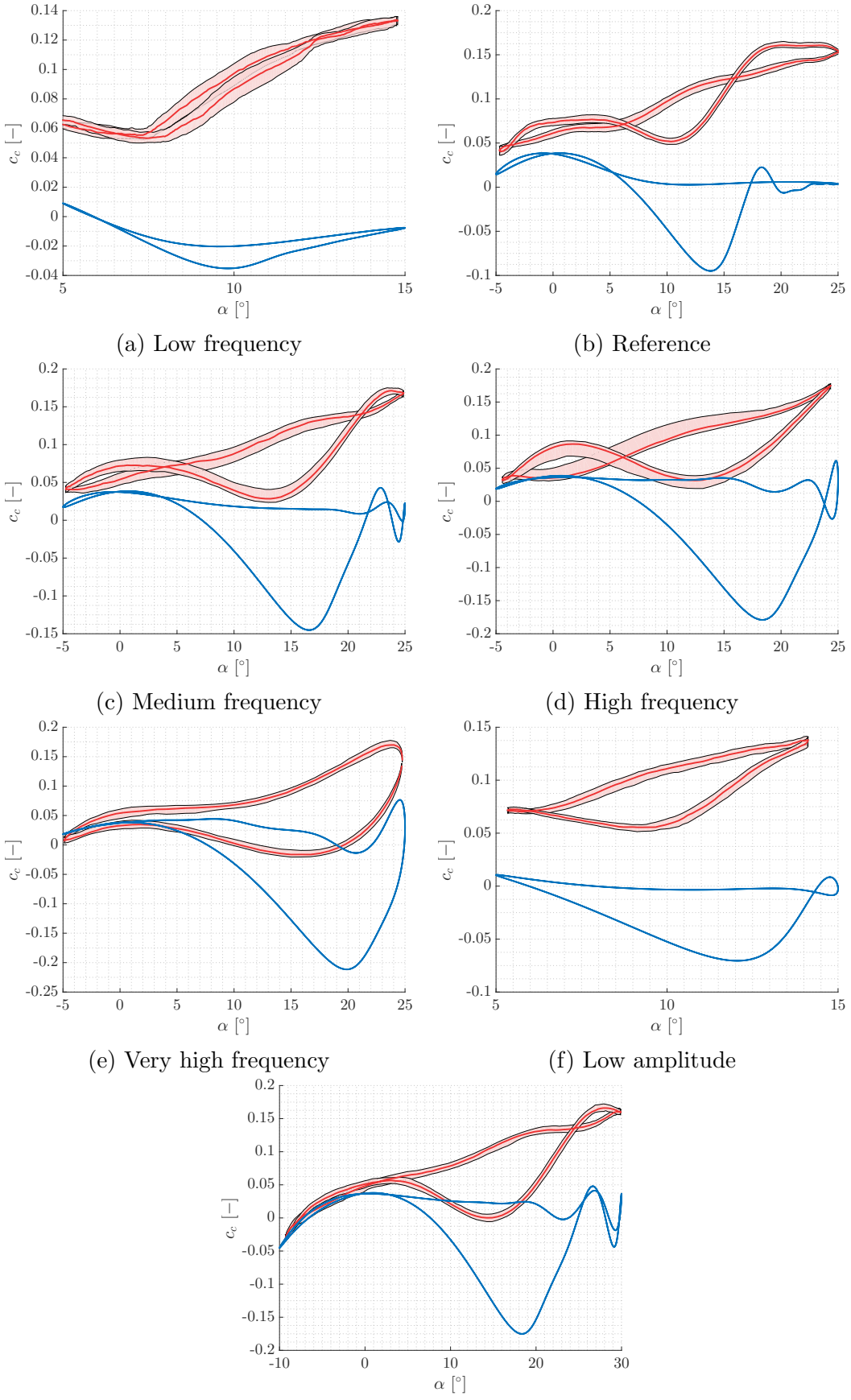

(a) Low frequency

(b) Reference

(c) Medium frequency

(d) High frequency

(e) Very high frequency

(f) Low amplitude

(g) High amplitude

Figure A.4: Chordwise force coefficient angle of attack evolution for studied cases

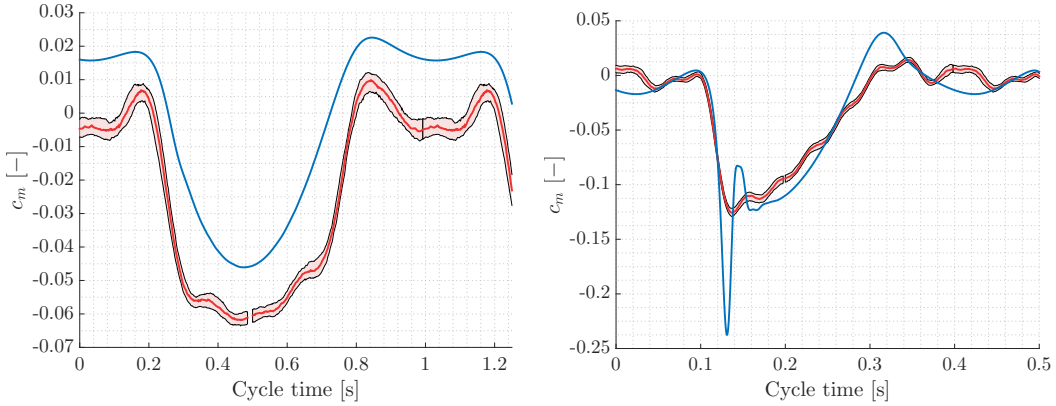

(a) Low frequency

(b) Reference

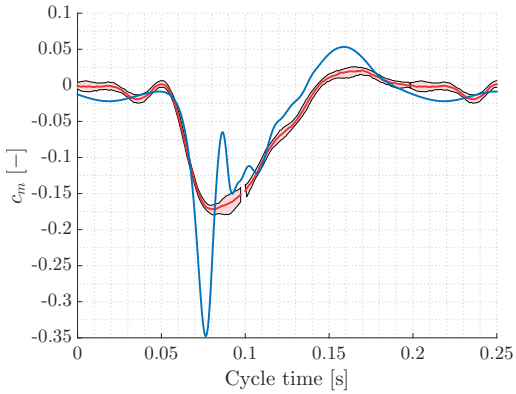

(c) Medium frequency

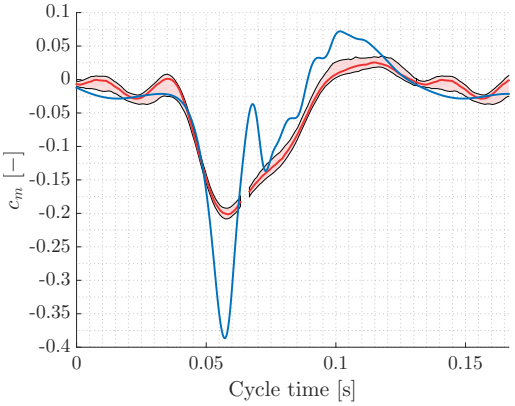

(d) High frequency

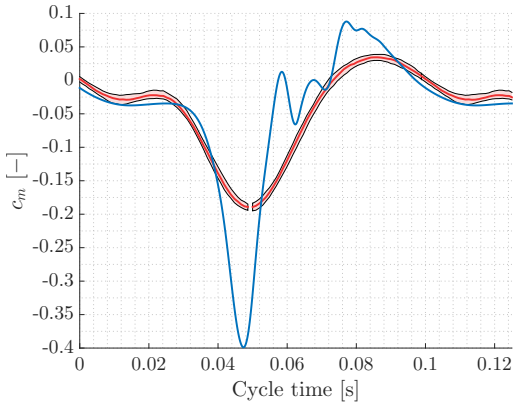

(e) Very high frequency

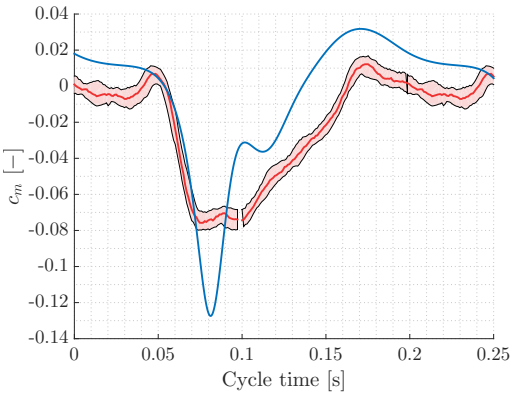

(f) Low amplitude

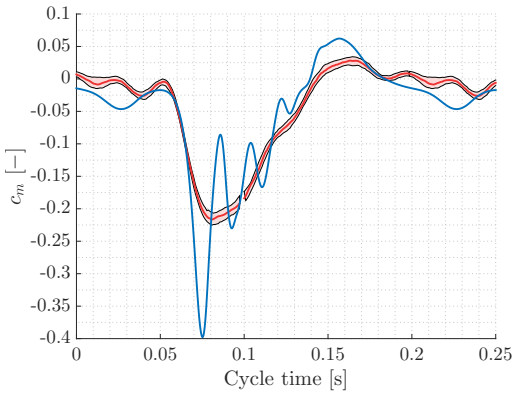

(g) High amplitude

Figure A.5: Pitch moment coefficient time evolution for studied cases

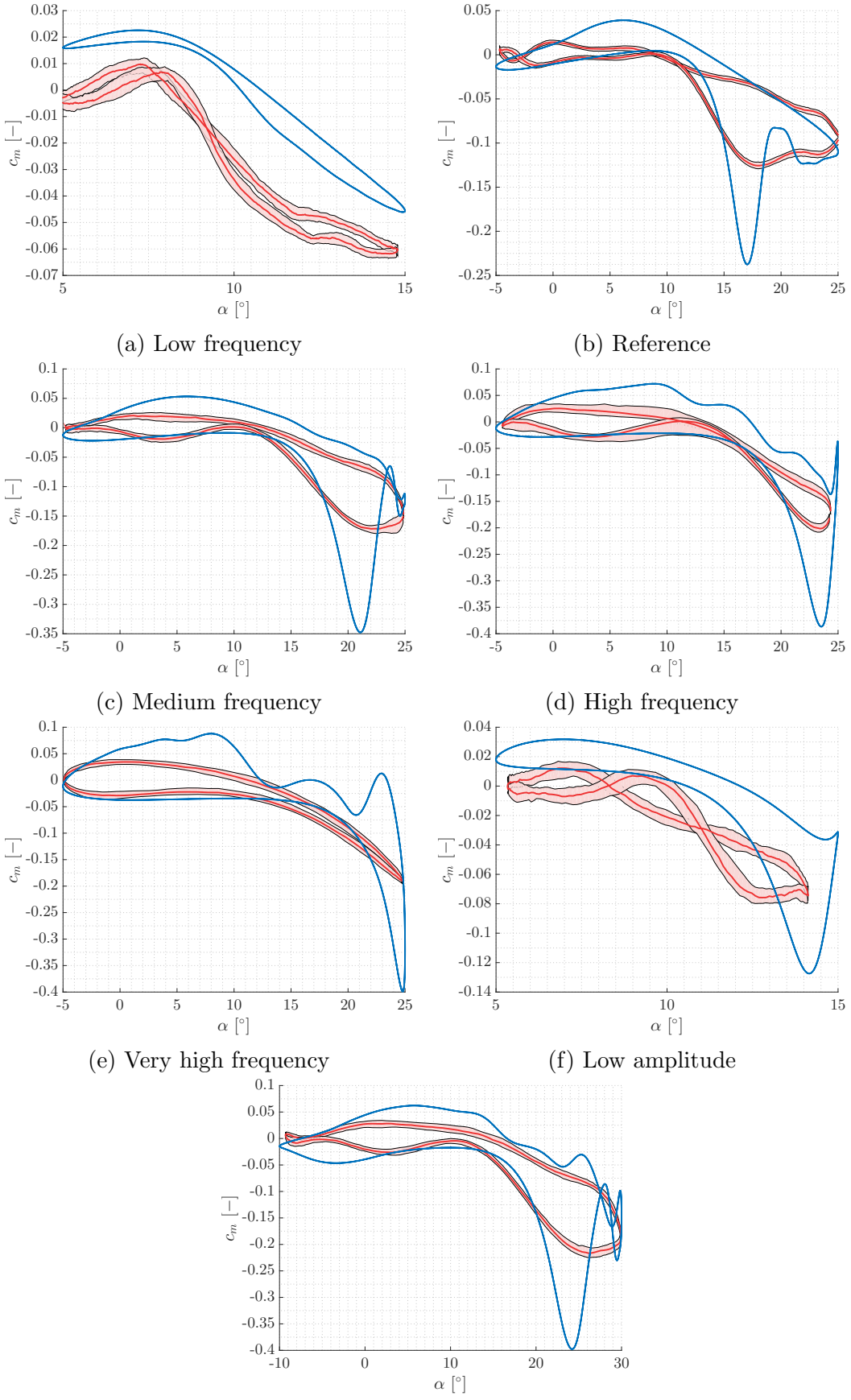

(a) Low frequency

(b) Reference

(c) Medium frequency

(d) High frequency

(e) Very high frequency

(f) Low amplitude

(g) High amplitude

Figure A.6: Pitch moment coefficient angle of attack evolution for studied cases

Appendix B

Separation and vortex behaviour for studied cases

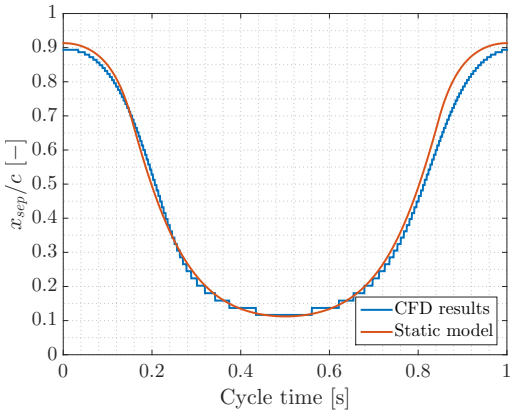

(a) Low frequency

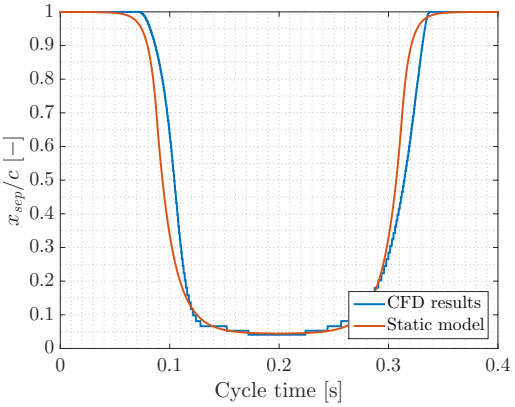

(b) Reference

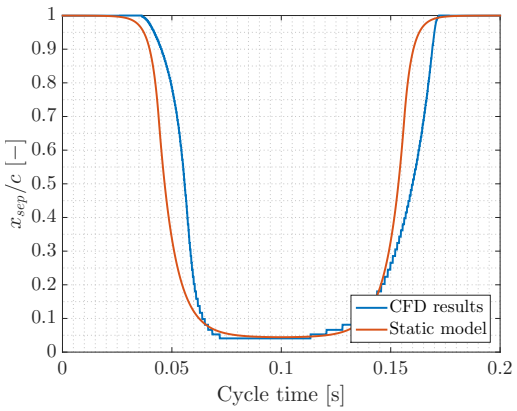

(c) Medium frequency

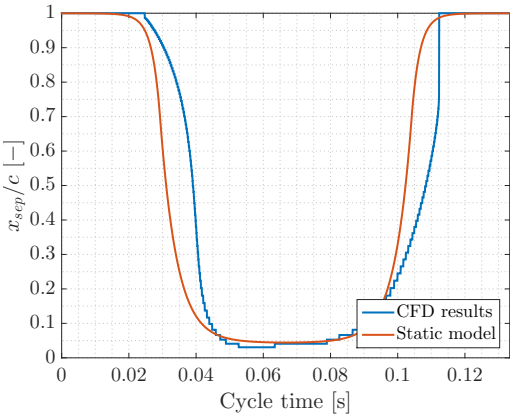

(d) High frequency

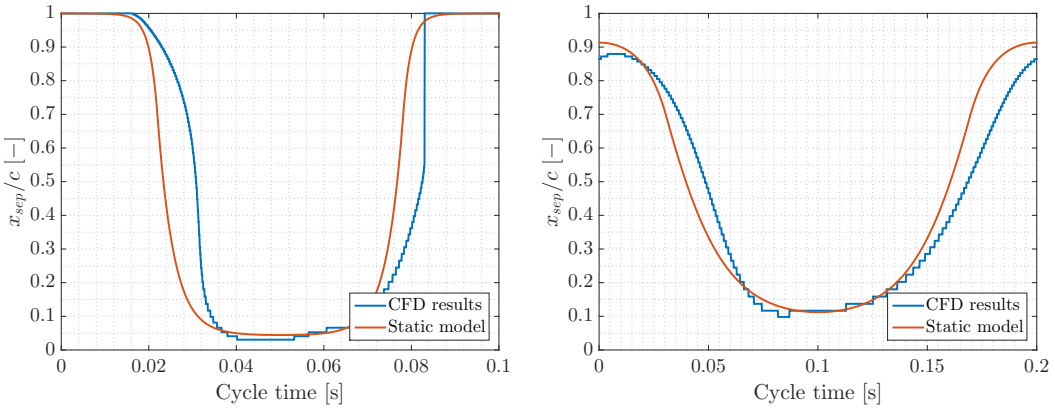

(e) Very high frequency

(f) Low amplitude

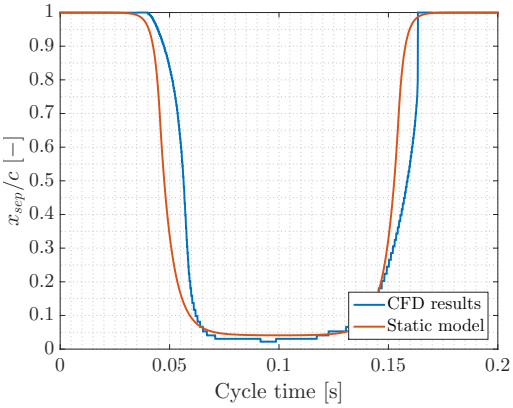

(g) High amplitude

Figure B.1: Separation point time evolution for studied cases

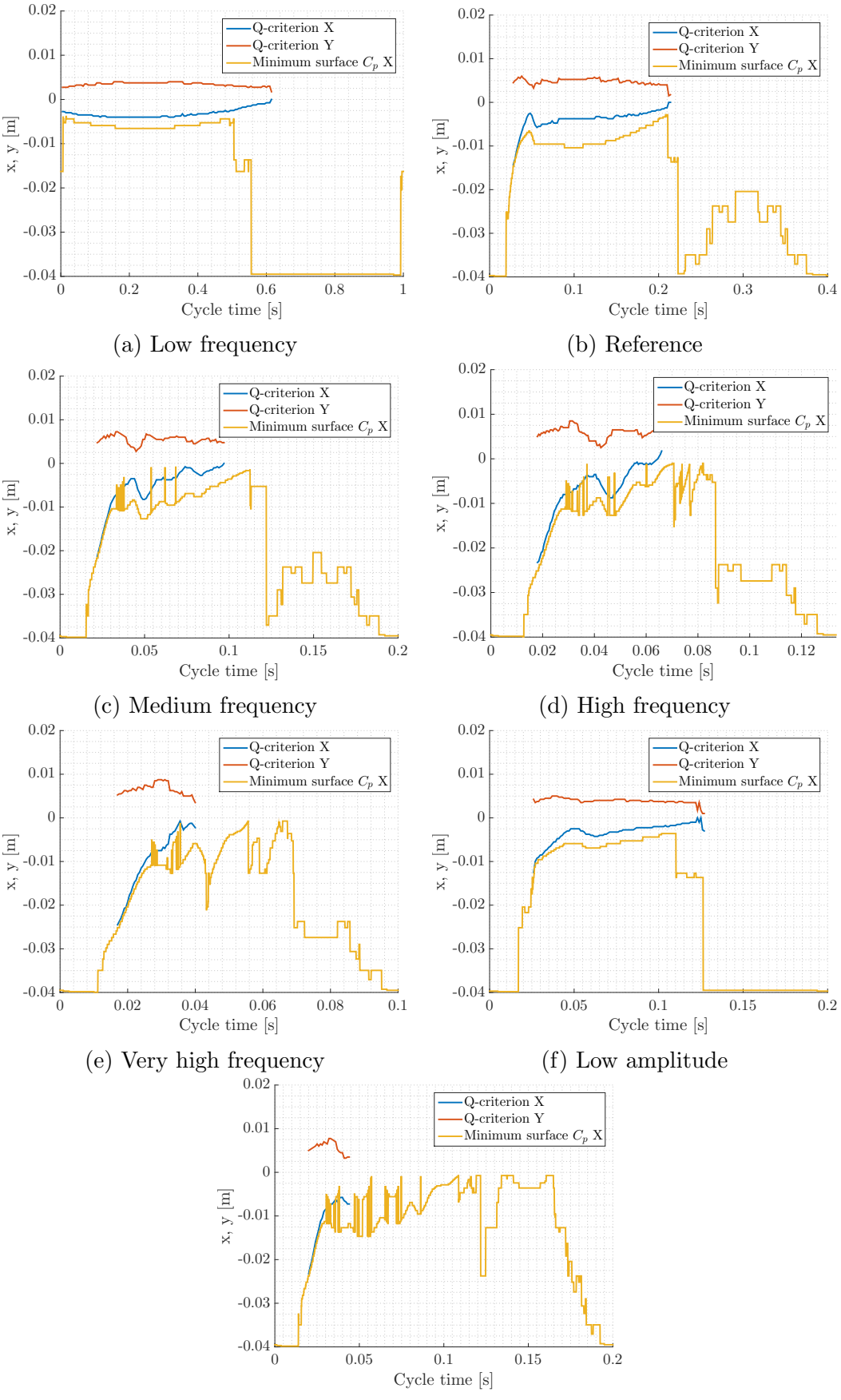

(a) Low frequency

(b) Reference

(c) Medium frequency

(d) High frequency

(e) Very high frequency

(f) Low amplitude

(g) High amplitude

Figure B.2: Comparison between vortex core and surface pressure criteria, time evolution of vortices

Appendix C

$C_p|_{LE}$ and $C_p|_{c/4}$ evolution with cycle time

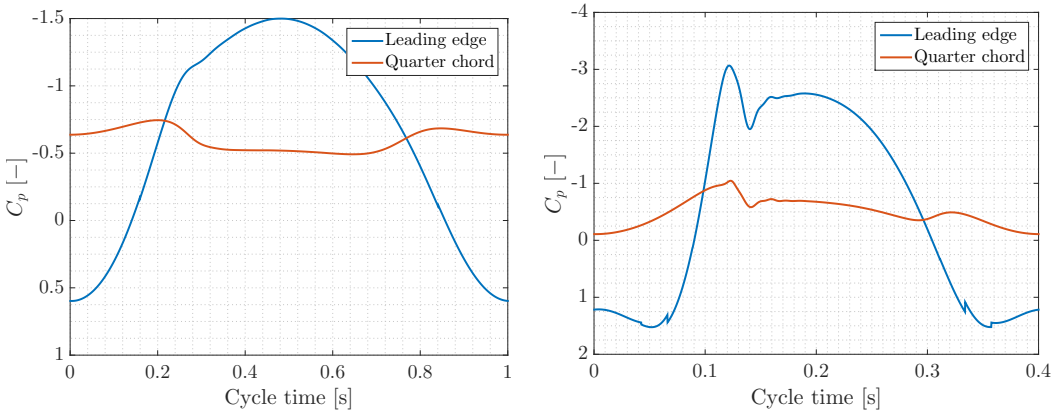

(a) Low frequency

(b) Reference

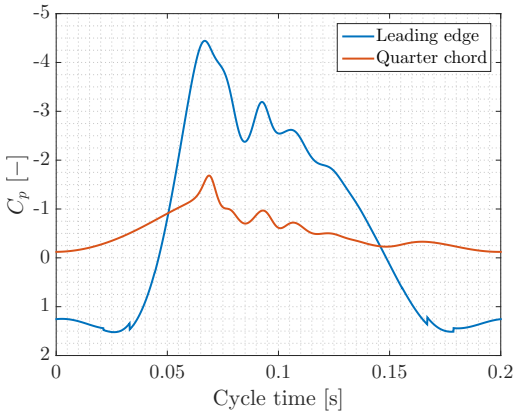

(c) Medium frequency

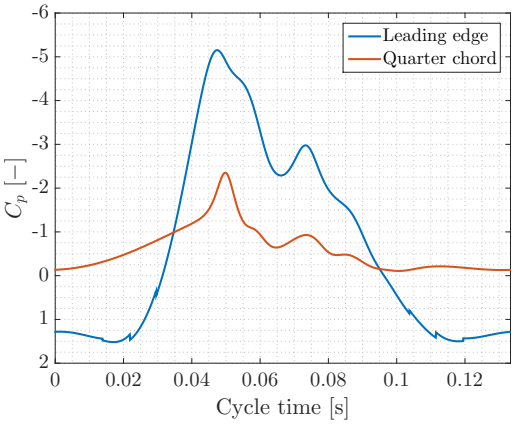

(d) High frequency

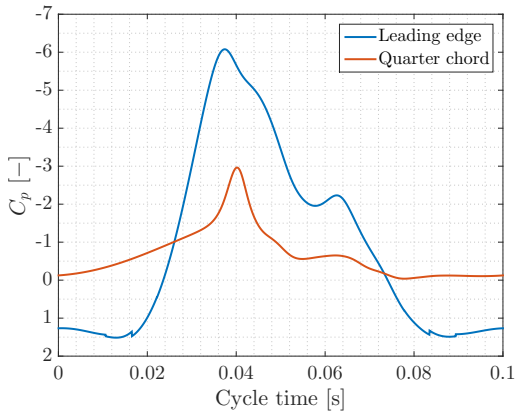

(e) Very high frequency

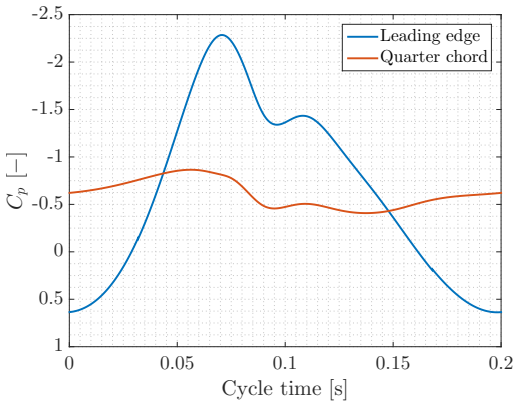

(f) Low amplitude

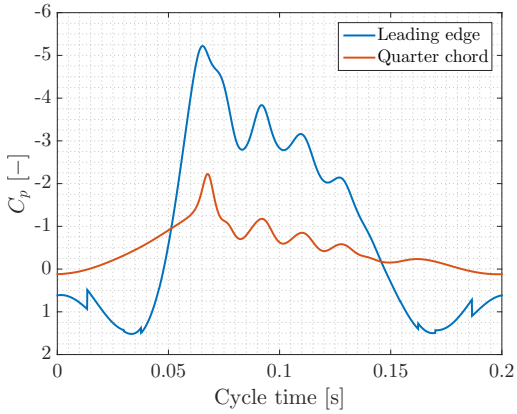

(g) High amplitude

Figure C.1: Pressure coefficient time evolution at leading edge and quarter chord